Mathematical Modelling of Molecular to Tissue Scale Patterning

The University Of Sheffield.

Eman M. Alwani

School of Mathematics and Statistics

University of Sheffield

This dissertation is submitted for the degree of

Doctor of Philosophy

October 2022

I would like to dedicate this thesis to my respectful parents, partner and children who have encouraged and supported me. They have been my greatest source of inspiration.

Declaration

I hereby declare that except where specific reference is made to the work of others, the contents of this thesis are original and have not been submitted in whole or in part for consideration for any other degree or qualification in this, or any other university. This thesis is my own work and contains nothing which is the outcome of work done in collaboration with others, except as specified in the text and the following acknowledgements.

Eman M. Alwani

October 2022

Acknowledgements

I am grateful to my supervisor Alexander Fletcher, whose support and guidance have been invaluable in providing this work towards completion. I would also like to thank our collaborator Andreas Buttenschön from the University of British Columbia, who helped inspired my work in Chapter 2. I am grateful for the discussions we had and for the code he provided, which I adapted to generate Fig. 2.11. I would also acknowledge my advisor Paul Blackwell for looking after my well-being and providing me with valuable advice and comments during my confirmation review. I have been lucky to be supported by friends in our 'DynoCaTs' journal club. Special thanks go to my friend Larra Trinidad for the great discussions that helped me understand the biology behind my work. She has provided me with an image for Fig. 1.1. I would also like to acknowledge my colleague Ian Groves for reading my reports and helping me to organise my work. Finally, my special thanks goes to my family and friends in Saudi Arabia for their emotional support during the stressful times. This work has been funded by the Government of Saudi Arabia and Umm Al-Qura University.

Abstract

The patterning of multicellular tissues is an essential process in embryonic development involving dynamic, iterative interactions between components from the molecular to the tissue scale. Mathematical modelling can help disentangle this complexity by integrating disparate experimental observations in a systematic conceptual framework. To that end, this thesis presents a suite of reaction-diffusion models of molecular to tissue scale patterning, ranging from generic, tractable models amenable to mathematical analysis to more detailed models that account for known biochemical interactions. At the molecular scale, we explore the phenomenon of protein complex clustering by modelling transmembrane homodimer formation. We identify conditions in which this model supports spatial patterns, corresponding to clusters, as a Turing or wave-pinning instability. Moving up a length scale, motivated by the 'core' planar polarity pathway in the fly wing, we model transmembrane heterodimer complex formation in a one-dimensional line of cells. We explore how different forms of molecular feedback interactions amplify initial asymmetries to drive this system to a spatial pattern (corresponding to planar polarisation). We then extend this model into two spatial dimensions and explore the existence and stability of different forms of patterning, including planar polarisation. Finally, we consider a two-dimensional model of the Fat-Dachsous planar polarity pathway, exploring the relative contributions of local feedback interactions and tissue-scale signalling cues in generating observed levels of planar polarisation in this system. Together, the contributions in this thesis advance the use of mathematical modelling to help understand patterning processes in developmental biology.

Table of contents

Chapter 1

Introduction

Embryonic development emerges from the complex interplay of cellular processes such as proliferation, movement and fate specification. These processes are regulated through a variety of forms of *patterning*, whereby structures that are initially (close to) spatially homogeneous evolve over time to become spatially heterogeneous in a robust and reproducible manner. Over 100 years after D'Arcy Thompson's *On Growth and Form* [1], and 70 years after Turing's *The Chemical Basis of Morphogenesis* [2], mathematical biology plays an increasingly important role in advancing our understanding of patterning in developmental biology. This thesis contributes to that endeavour through the construction and analysis of a suite of mathematical models of patterning from the molecular to the tissue scale.

To provide a foundation for this work, in this chapter we discuss the relevant background biology and approaches. The remainder of this chapter is structured as follows. In Section 1.1 we discuss patterning from the molecular to the tissue scale and highlight key open questions at each scale. In Section 1.2 we discuss how mathematical modelling has been successfully used to study developmental patterning. In Section 1.3 we discuss how *planar polarity* provides an excellent exemplar for studying the principles of molecular to tissue scale patterning. Finally, in Section 1.4 we summarise the key research questions to be tackled in this thesis and present an outline for the remainder of the thesis.

1.1 Molecular to tissue scale patterning

The patterning of multicellular tissues is essential for the formation of the organs that make up our bodies. It relies on *self-organisation*, which emerges from dynamic, iterative interactions between components from molecular to tissue scales [3].

At the molecular scale, there is increasing experimental evidence that proteins involved in cellular signalling and communication do not accumulate uniformly within cells, but instead form spatially localised clusters [4, 5]. An important example is the cell-cell adhesion protein E-cadherin, which forms transmembrane complexes linking adjacent cells, and regulates important cellular processes such as cell polarisation [6]. Super-resolution microscopy has revealed that E-cadherin complexes form high-density nano-scale clusters [4, 7]. The size, distribution, and dynamics of these clusters are likely to have consequences on local adhesive forces and tensile force transmission [4], since they interact with the cortical actin cytoskeleton [8]. Another example is provided by planar polarity proteins (see Section 1.3), which have been shown to cluster into discrete stable membrane subdomains, or *puncta* [5, 9]. Experiments suggest that such clustering is functionally important for the generation of cellular polarity [9]. However, the mechanisms underlying puncta formation, the stability over the timescale of planar polarisation, and the nature of any feedback interactions that amplify cluster sorting, still remain unknown [10, 11].

Local organisation of proteins into clusters does not suffice to explain self-organisation of locally coordinated cell polarisation. Moving up a length scale, cellular symmetry breaking and polarisation [12] emerge from the coordination of molecular interactions through intracellular interactions. For example, during planar polarisation of epithelial tissues, intercellular complex formation and feedback interactions result in the asymmetric distribution of polarity proteins at opposite ends of the cell [13]. Heterogeneity and variability in protein interactions have increasingly been recognised as playing an important role in cell-level patterning and signal interpretation [14]. However, while reaction-diffusion networks [15] and gradients

of post-translational modification [16] have been suggested to underlie cell-scale patterning events, the precise mechanisms largely remain unclear.

Finally, at the tissue scale, intercellular communication and polarised behaviours such as cell division and intercalation locally coordinate cell polarity, while long-range controls have been posited to coordinate patterning across tissues [17]. For example, it has been proposed that the alignment and orientation of planar polarity across a tissue many hundreds or thousands of cells across can arise from a graded 'global directional cue' that could be mechanical and/or chemical in nature [18, 19]. However, the source, timing, and persistence of the mechanisms coordinating tissue-scale pattering remain unclear in many cases.

1.2 Mathematical modelling

Spatial patterns in biology have been inspiring mathematicians for decades, if not centuries. The complexity of particular biological systems has given rise to new specialised research fields, such as mathematical oncology [20]. Nevertheless, simplified mathematical models are still helpful in explaining the – often non-intuitive – general mechanisms underlying biological pattern formation.

Within developmental biology, a particularly successful modelling approach – whose roots lie in the groundbreaking early work of Turing [2] – is to consider the biochemical reaction kinetics and diffusive transport of key proteins or other signalling molecules that form the spatial pattern of interest. Given suitable initial conditions and sufficiently large differences in the diffusion rates of the state variables, *reaction-diffusion systems* share some key mathematical properties including: (i) in the absence of any initial asymmetry, these systems can exhibit stable self-organised patterns (spatially non-uniform steady states) [21]; (ii) different reaction/diffusion parameters are sufficient to produce a variety of distinct patterns [22, 23]; and (iii) patterns formed via reaction-diffusion systems may be sensitive to external perturbations [15, 24].

Reaction-diffusion systems exhibiting pattern formation include the two-component *activator-substrate* mechanism, whereby spatially localised peaks in chemical concentration emerge via a rapidly diffusive substrate and a slowly diffusive activator. Such models have been applied to processes from the molecular to the tissue scale. A relevant cell-scale patterning example is the work of Mori et al. [25], who model the diffusion and the switch between the bound active and inactive forms of the protein Rho-GDP that are found in the cell membrane and cytosol, respectively. The authors find that the rate of protein diffusion, and the total protein concentration within the cell and whether this is conserved over time, play important rules in pattern formation in this system (Rho-GDP polarisation). We explore other relevant models of patterning in more detail in Chapters 2–5.

In this thesis we shall make extensive use of reaction-diffusion based modelling. Nevertheless, it is worth emphasising that not all developmental patterns are based on reaction-diffusion systems or biochemical signalling more generally. Indeed, there is growing evidence for the importance of cell adhesion and other mechanical contributions to many important patterning events, such as follicle patterning [26]. The interactions between mechanics and biochemistry in developmental patterning is a highly active area of current research, which we return to in our concluding discussion in Chapter 6.

1.3 Planar polarity

An important exemplar for developmental patterning, which will motivate much of the work presented in this thesis, is *planar polarity*. During embryogenesis, oriented cell behaviours are required to ensure correct tissue structure, and to generate asymmetries such as the head-tail axis [27]. Planar polarity, whereby cells become polarised within a particular plane, is an important form of oriented cell behaviour [28]. Such behaviour is often observed in epithelial tissues, which line the surfaces of organs and body cavities, and which are composed of sheets of tightly adherent cells that typically adopt a polygonal packing [29].

Planar polarity is involved in a variety of morphogenetic events, such as oriented cell divisions and rearrangements, that help to determine the overall shape, size and structure of developing organs. Hence, elucidating the mechanisms underlying the establishment and maintenance of planar polarity helps us obtain a deeper understanding of how the behaviours of individual cells are interpreted and coordinated to achieve tissue-scale patterning.

Loss of planar polarity is associated with failure of neural tube closure during early embryogenesis [30], spermiation defects [31], cardiac patterning defects [32], and cellular patterning defects in the cochlea that can cause deafness [33]. Understanding the mechanisms underlying planar polarity therefore also offers the possibility of improved therapies for developmental diseases, as well as other medical conditions such as cancer metastasis that involve disruptions to tissue patterning.

A powerful yet cost-effective experimental model for studying planar polarity is the fruit fly *Drosophila*. Planar polarity is demonstrated externally by the alignment of hairs on the wings and the abdomen of the adult fly (Fig. 1.1), with each hair being produced by a single cell (Fig. 1.2 c and d), and polarised with respect to the axis of the body or appendage [27]. For much of this thesis, we will be motivated by experimental studies of planar polarity in the developing fly wing. However, it is worth emphasising that the principles seen in the wing are conserved across many different tissues and species [28].

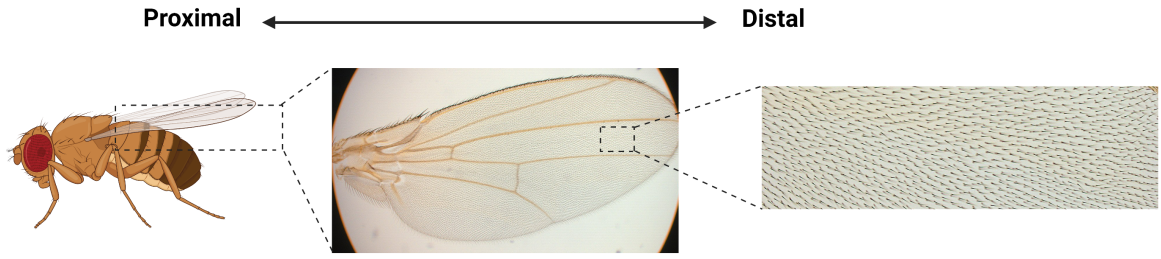

Fig. 1.1 Image of a wild-type *Drosophila* wing, showing uniform distal orientation of trichomes, taken by Larra Trinidad. The fly schematic on the left is created with BioRender.

A key pathway involved in the establishment of planar polarity is the ‘core’ planar polarity pathway [28]. The core pathway shows clear evidence of communication between

neighbouring cells [13] and exhibits asymmetric subcellular localised 'bridges' formed of several proteins within and across neighbouring cells. In the fly wing, planar polarity proteins localise to the proximal (parts closer to the body of the fly) and distal sides of each cell's membrane. These *transmembrane* proteins act as gateways that permit signalling between cells. During early wing development, the transmembrane protein Frizzled (Fz) and the cytosolic proteins Dishevelled (Dsh) and Diego (Dgo) localise to distal cell edges. The transmembrane protein Van Gogh (Vang) and the cytosolic protein Prickle (Pk), however, localise proximally, while the transmembrane cadherin Flamingo (Fmi) localises to both the distal and proximal sides of each cell (Fig. 1.2a) [28].

The molecular logic of the core pathway can be investigated by mutating a small group of cells (*clones*) for a particular core protein and assessing if and how the polarity of juxtaposed wild-type (genetically normal) cells are affected [17]. The removal of any core protein via genetic manipulation disrupts polarisation and leads to 'prehairs' (the stage before a hair emerges) often being formed at the wrong cell edge [34]. In fact, in most strong mutant phenotypes, the trichomes instead form in the cell centre before adopting a wrong polarity as they grow [35]. A *domineering non-autonomous* phenotype is observed [36] when a group of cells lacking Fz activity induces neighbouring wild-type cells to polarise towards mutant cells (Fig. 1.3a). Conversely, a group of cells mutated for Vang (Fig. 1.3b) induce neighbouring wild-type cells to polarise away from the mutant cells [37, 38].

Another key planar polarity pathway is the Ft-Ds pathway. This pathway consists of the two atypical cadherins, Fat (Ft) [39] and Dachsous (Ds) [40], that form heterodimers via their long extracellular domain between adjacent cells (Fig. 1.2b). This pathway also consists of the transmembrane kinase Four-Jointed (Fj) [41], which can modulate Ft and Ds binding affinity [42–44], as well as another atypical myosin effector protein called Dachs [45]. Opposing tissue expression gradients of Ft and Ds along the proximal–distal axis of the

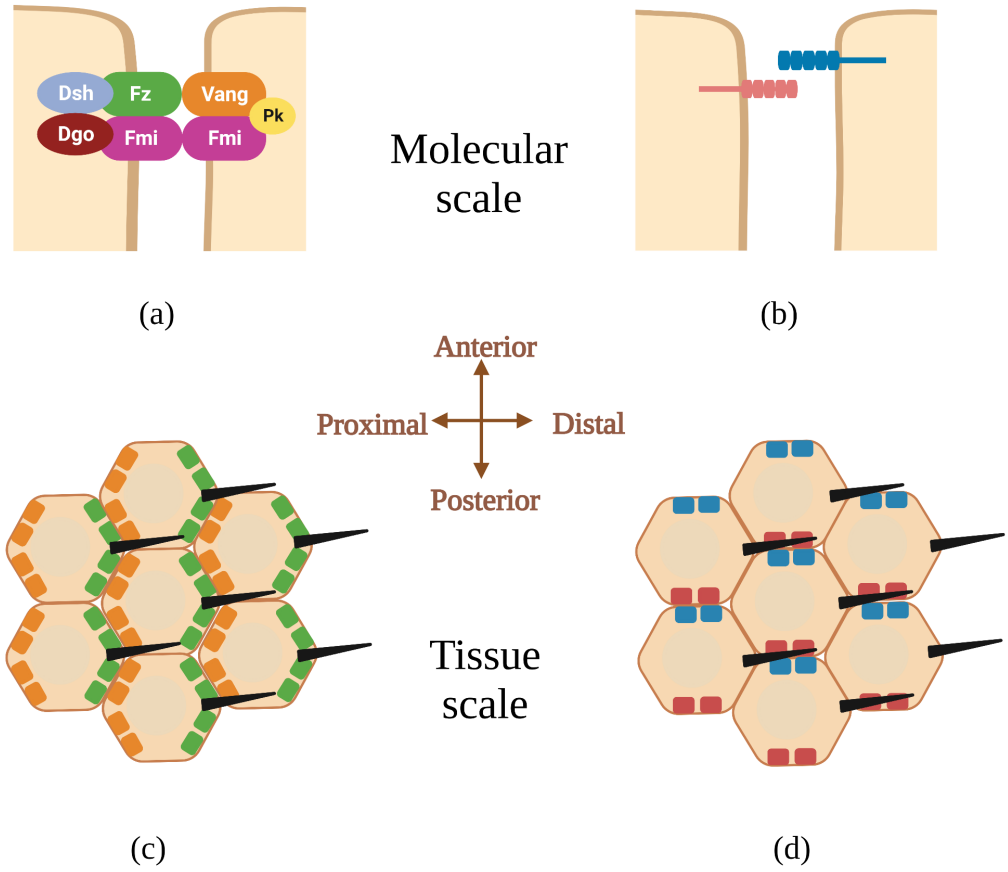

Fig. 1.2 Planar polarity pathways from the molecular to the tissue scale. (a) Core pathway components form asymmetric intercellular complexes at cell junctions. (b) The Ft-Ds pathway proteins Ft (teal) and Ds (pink) form heterodimers between adjacent cells. (c) Schematic of asymmetric localisation of two planar polarity proteins in the fly wing: Fz at distal cell edges (green) and Vang at proximal cell edges (orange). (d) Schematic of asymmetric localisation of Ft and Ds in the fly wing: Ft at anterior cell edges (teal) and Ds at posterior cell edges (pink). Trichomes – microscopic outgrowths of hair (black triangles) – emerge at the distal vertex of each cell as a result of polarity protein localisation (c, d). This Figure is created with BioRender.

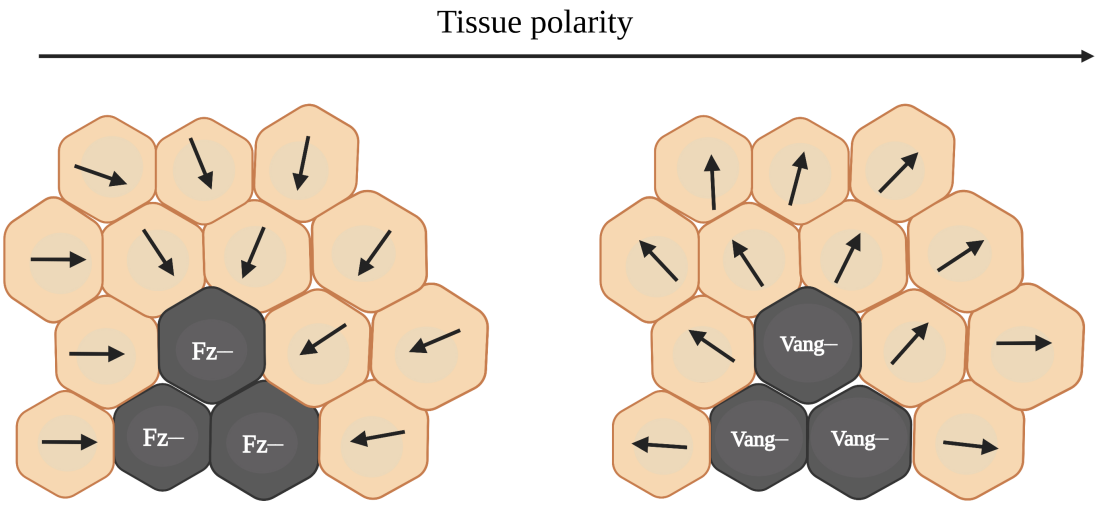

(a) (b)

Fig. 1.3 Schematic of polarity defects in the *Drosophila* wing, illustrating domineering non-autonomy of a central group of cells lacking (a) Fz and (b) Vang activity, visualised through disrupted orientation of neighbouring cells' trichomes (black arrows). Based on experimental observations [36]. This Figure is created with BioRender.

developing fly wing (reviewed in [46]) results in intracellular asymmetric localisation of the Ft-Ds components to the anterior and posterior compartments of each cell (Fig. 1.2d).

1.4 Thesis outline

As summarised above, there are a number of outstanding questions concerning the mechanisms underlying molecular to tissue scale patterning events in development, which mathematical modelling can help shed light on. To address this, in Chapters 2–5 we present and analyse a suite of mathematical models. The remainder of this thesis is structured as follows.

In Chapter 2, we focus on molecular scale patterning. Motivated by the example of E-cadherin clustering, we construct an abstracted reaction-diffusion model of transmembrane homodimer complex formation along a one-dimensional continuous spatial domain, representing a single cell-cell junction within an epithelial tissue. Using a combination

of steady state, linear stability, bifurcation, and asymptotic analysis, as well as numerical simulations, we explore under what circumstances this model supports spatially localised patterns (corresponding to clusters, or puncta) as a Turing and/or wave-pinning instability.

In Chapter 3, we focus on cell-to-tissue scale patterning. Motivated by the example of establishment of core pathway planar polarity across the fly wing, we construct an abstracted reaction-diffusion model of transmembrane heterodimer complex formation in a one-dimensional discrete spatial domain, representing several cells within a tissue. Using a combination of steady state, linear stability, and bifurcation analysis, as well as numerical simulations, we explore how different forms and mechanisms of nonlinear feedback interactions could amplify initial asymmetries to drive the system to a spatial pattern (corresponding to planar polarisation).

In Chapter 4, we extend our abstracted model from Chapter 3 into two spatial dimensions, considering a static hexagonal cell packing representing the fly wing. Using a combination of analytic and numerical approaches, we explore the existence and stability of different forms of patterning, including planar polarisation, in this system.

In Chapter 5, we focus on a more biochemically detailed model of the Ft-Ds planar polarity pathway, previously proposed by Hale et al. [44] for one spatial dimension, and extend this model to two spatial dimensions. Through a range of numerical simulations, we explore the scientific hypothesis that both weak positive feedback as well as a strong global cue is required in order to generate the experimentally observed degree of planar polarisation in this system.

Finally, in Chapter 6, we conclude with a summary of the major results in this thesis and discuss possible avenues for future work.

Chapter 2

Turing and wave-pinning mechanisms of protein complex clustering

2.1 Introduction

As described in Chapter 1, developmental patterning at the tissue scale has its roots in protein interactions at the molecular scale. There is increasing recognition that pattern formation at the level of membrane-bound protein complex clustering and asymmetric localisation underlies important biological processes including cell-cell adhesion and planar polarisation. However, the question of how transmembrane protein complexes locally cluster is still unanswered. The most favoured hypothesis is that this 'self-organising' process may depend on local positive feedback interactions [5, 47], although the mechanism and nature (for example, whether they are self-limiting) of such interactions remain to be elucidated.

Reaction-diffusion models offer a flexible mathematical framework within which to study the possible mechanisms underlying spatial pattern formation. As discussed briefly in Section 1.2, one example of a well-known reaction-diffusion mechanism for pattern formation is the Turing instability [48], which generates spatially periodic peaks and troughs in the concentrations of key chemicals or proteins of interest. A mathematically related

behaviour is the 'wave-pinning' instability [49, 50], which generates spatial subdomains with uniform, separated phases of high and low concentrations connected by a 'wavefront'. Both these mechanisms have been posited in the context of molecular-scale pattern formation [51, 49, 50], though to date there has been little in the way of applications to protein complex clustering in the context of cell-cell adhesion or planar polarity.

2.1.1 Aim of work

In this chapter, we propose a minimal reaction-diffusion model for the formation of protein complex clusters at a cell-cell junction that incorporates some form of nonlinear feedback interactions. Our direct motivation is to understand the formation of E-cadherin homodimer clusters in cell-cell adhesion, though our framework could be naturally extended to explore the clustering of complexes comprising two or more monomer species.

Our aim is to use a combination of analytic, asymptotic, and numerical methods to assess the conditions under which spatially localised patterns are possible in this model. We are also interested in addressing the following questions concerning properties of such patterns: (i) When can 'clusters' (spatially localised non-uniform steady state solutions) form? (ii) Under what circumstances can multiple stable clusters co-exist? (iii) How do cluster shape, size and location depend on the hypothesised form of feedback interactions and parameter values? We first consider a model in which the total mass of our protein of interest (monomers and complexes) along the cell-cell junction is conserved. We then loosen this assumption by introducing monomer trafficking and monomer/complex recycling into the model.

The remainder of this chapter is structured as follows. In Section 2.2 we first describe our modelling assumptions and derive the governing equations for our model. We present a steady state and linear stability analysis, as well as numerical simulations, to support the occurrence of complex clustering in this model. We also use asymptotic analysis to obtain some approximate expressions relating to the formation of a single cluster. In Section 2.3,

we present a modified form of the model that is no longer conservative, and explore how this affects the occurence and properties of complex clustering. We conclude in Section 2.4 by discussing how our theoretical results may relate to E-cadherin compelx clusters in cell-cell adhesion and to Fz/Vang complex puncta in the core planar polarity pathway.

2.2 Mass conserved reaction-diffusion model

In this section, we analyse a simplified model for pattern formation under the restriction of mass conservation. We assume that a protein of interest can form transmembrane homodimer complexes across a cell-cell junction, which for simplicity we model as a one-dimensional line segment.

2.2.1 Governing equations

Let $A(X,T)$ and $A^{\dagger}(X,T)$ denote the concentrations of an unbound protein (or *monomer*) on either side of a cell-cell junction at position $0 < X < L$ and time $T > 0$, respectively (Fig. 2.1). Similarly, let $C(X,T)$ denote the concentration of protein complex (or *dimer*), which we assume forms from two protein molecules on either side of the cell-cell junction binding reversibly according to the reaction

$$A + A^{\dagger} \rightleftharpoons C, \tag{2.1}$$

with a forward rate coefficient k and a reverse rate coefficient v.

We assume that unbound protein on either side of the cell junction can diffuse within the plasma membrane with a diffusion coefficient $D_A > 0$, while complexes diffuse within the plasma membrane with a coefficient D_C, such that complexes diffuse much more slowly than unbound molecules ($D_C \ll D_A$). Relating this model to the motivating example of the adhesion protein E-cadherin, we may expect slower diffusion of the complex, since

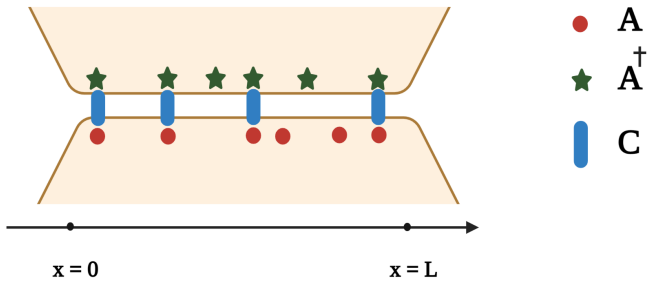

Fig. 2.1 Schematic of a single cell-cell adhesion representing the biochemical reaction (2.1). An unbound protein is spatially distributed on either side of a cell-cell junction (A: red dots in one cell; $A^\dagger$: green stars in the other cell). The complex C is formed via the intercellular binding of one unbound A protein and one unbound $A^\dagger$ protein. This schematic is created with BioRender.

adhesive complexes diffuse more slowly as soon as they attach to a cell cytoskeleton [4]. For simplicity, we assume no-flux boundary conditions at $X = 0$ and $X = L$.

We assume throughout this chapter that D_C, D_A, and v are constants, while k may depend on the local complex concentration. We assume that there is a monotonic increasing function on the forward binding rate. From a biological point of view, considering nonlinear feedback in the binding rate may correspond to binding affinity being affected by the local presence of the complex.

The above assumptions give rise to the reaction-diffusion system

$$\frac{\partial A}{\partial T} = D_A \frac{\partial^2 A}{\partial X^2} - kAA^\dagger + vC, \tag{2.2}$$

$$\frac{\partial A^\dagger}{\partial T} = D_A \frac{\partial^2 A^\dagger}{\partial X^2} - kAA^\dagger + vC, \tag{2.3}$$

$$\frac{\partial C}{\partial T} = D_C \frac{\partial^2 C}{\partial X^2} + kAA^\dagger - vC, \tag{2.4}$$

for $0 < X < L$, $T > 0$, with zero-flux boundary conditions

$$\frac{\partial A}{\partial X} = \frac{\partial A^\dagger}{\partial X} = \frac{\partial C}{\partial X} = 0 \tag{2.5}$$

at $X = 0$ and $X = L$. The initial conditions are chosen to be close to spatially uniform with no complex present such that

$$A(X,0) \approx A_0, \qquad A^\dagger(X,0) \approx A_0, \qquad C(X,0) = 0. \tag{2.6}$$

The system (2.2)–(2.4) has two conserved quantities, corresponding to the total (unbound plus bound) amount of protein in each cell sharing the junction,

$$A_T = \int_0^L (A(X,T) + C(X,T))\,\mathrm{d}X, \tag{2.7}$$

$$A_T^\dagger = \int_0^L (A^\dagger(X,T) + C(X,T))\,\mathrm{d}X, \tag{2.8}$$

where the values of A_T and $A_T^\dagger$ are determined by the initial conditions.

To non-dimensionalise the system (2.2)-(2.4), we write $k = k_0 \mathscr{K}$, where k_0 denotes a baseline value for the forward reaction rate coefficient. We then let $T = T_0 t$, $X = Lx$, $C = k_0 c$, $A = k_0 a$, $A^\dagger = k_0 a^\dagger$, and $A_T = k_0 a_T$, $A_T^\dagger = k_0 a_T^\dagger$, where x, t, c, a and $a^\dagger$ denote dimensionless variables. Finally, we take the domain length L to be the relevant length scale and choose $T_0 = L/\sqrt{v}\sqrt{D_C}$ and define the (positive) dimensionless lumped parameters

$$\varepsilon = \frac{\sqrt{D_C}}{L\sqrt{v}}, \qquad D_a = \frac{D_A}{vL^2}, \qquad \alpha = \frac{k_0^2}{v}. \tag{2.9}$$

In this non-dimensionalisation, L represents a typical cell diameter (on the order of micrometres). The dissociation constant of the reaction rate v is typically $O(1)$ per second. The diffusion coefficients are typically $O(1)$ squared micrometres per second. Since $\varepsilon \ll D_a$, ε is small, we let $D_a \approx O(1)$ with respect to ε, *i.e.* $\sqrt{D_C/v} \approx L$. This assumption means that the

protein can diffuse across the domain on the time scale of the biological reaction [49]. In the majority of our simulations in Section 2.2.3, we consider the dimensionless time unit to be approximately 10 seconds (s), although we also discuss the behaviour of the system over faster ($t = 0.5$ s) and slower ($t = 50$ s) time scales.

Under this non-dimensionalisation, the system is given by

$$\varepsilon \frac{\partial a}{\partial t} = D_a \frac{\partial^2 a}{\partial x^2} - \alpha \mathscr{K}(c) a a^\dagger + c, \tag{2.10}$$

$$\varepsilon \frac{\partial a^\dagger}{\partial t} = D_a \frac{\partial^2 a^\dagger}{\partial x^2} - \alpha \mathscr{K}(c) a a^\dagger + c, \tag{2.11}$$

$$\varepsilon \frac{\partial c}{\partial t} = \varepsilon^2 \frac{\partial^2 c}{\partial x^2} + \alpha \mathscr{K}(c) a a^\dagger - c, \tag{2.12}$$

with conserved quantities

$$a_T = \int_0^1 (a(x,t) + c(x,t))\,\mathrm{d}x, \tag{2.13}$$

$$a_T^\dagger = \int_0^1 (a^\dagger(x,t) + c(x,t))\,\mathrm{d}x, \tag{2.14}$$

and zero-flux boundary conditions

$$\frac{\partial a}{\partial x} = \frac{\partial a^\dagger}{\partial x} = \frac{\partial c}{\partial x} = 0 \tag{2.15}$$

at $x = 0$ and $x = 1$.

2.2.2 Steady state and stability analysis

In this section, we first investigate the existence and uniqueness of any positive spatially uniform steady state (SUSS) solution to the system (2.10)–(2.15). We then conduct a classical Turing analysis to verify that a stable positive SUSS can exhibit a diffusion-driven instability in this model.

Existence and uniqueness of positive SUSS

We seek a positive SUSS of the system (2.10)–(2.12) of the form $a(x,t) \equiv a^*$, $a^\dagger(x,t) \equiv a^{\dagger *}$, $c(x,t) \equiv c^*$. Substituting this into our model, we find that any SUSS must satisfy

$$\alpha \mathscr{K}(c^*) a^* a^{\dagger *} - c^* = 0, \tag{2.16}$$

$$a^* + c^* = a_T, \tag{2.17}$$

$$a^{\dagger *} + c^* = a_T^\dagger. \tag{2.18}$$

Using equations (2.16)–(2.18) to write $a^{\dagger *}$ and a^* in terms of c^*, we obtain

$$\alpha \mathscr{K}(c^*)(a_T - c^*)(a_T^\dagger - c^*) = c^*. \tag{2.19}$$

In the absence of feedback ($\mathscr{K} = 1$), equation (2.19) simplifies to a quadratic equation, which has two real positive solutions since the model is conservative. Admissible solutions must satisfy

$$c^* \leq \max(a_T, a_T^\dagger). \tag{2.20}$$

There is therefore a unique admissible root given by

$$c^* = \frac{1}{2\alpha}\left(\alpha a_T + \alpha a_T^\dagger + 1 - \sqrt{(\alpha a_T + \alpha a_T^\dagger + 1)^2 - 4\alpha^2 a_T a_T^\dagger}\right). \tag{2.21}$$

In this case, we have

$$a^* = \frac{1}{2\alpha}\left(\alpha a_T - \alpha a_T^\dagger - 1 + \sqrt{(\alpha a_T + \alpha a_T^\dagger + 1)^2 - 4\alpha^2 a_T a_T^\dagger}\right), \tag{2.22}$$

$$a^{\dagger *} = \frac{1}{2\alpha}\left(\alpha a_T^\dagger - \alpha a_T - 1 + \sqrt{(\alpha a_T + \alpha a_T^\dagger + 1)^2 - 4\alpha^2 a_T a_T^\dagger}\right). \tag{2.23}$$

This shows that the system (2.10)–(2.12) without feedback always has a unique SUSS, which means that in this case patterning is never obtained. However, in the presence of feedback ($\mathscr{K}$ is a monotonic increasing function of the complex), the existence and uniqueness of the steady state depends on the type of feedback and the choice of parameters. We return to this point when considering two specific forms of feedback in Section 2.2.3.

Linear stability of SUSS

We now examine the linear stability of any SUSS. We let $a = a^* + \tilde{a}$, $a^\dagger = a^{\dagger *} + \tilde{a}^\dagger$, and $c = c^* + \tilde{c}$, where $\tilde{a}$, $\tilde{a}^\dagger$, $\tilde{c}$ are small perturbations. Substituting into (2.10)–(2.12) and dropping higher-order terms, we obtain the linearised system

$$\varepsilon \frac{\partial \tilde{a}}{\partial t} = D_a \frac{\partial^2 \tilde{a}}{\partial x^2} - \alpha a^{\dagger *} \mathscr{K} \tilde{a} - \alpha a^* \mathscr{K} \tilde{a}^\dagger + \left(1 - \alpha a^* a^{\dagger *} \mathscr{K}'\right) \tilde{c}, \tag{2.24}$$

$$\varepsilon \frac{\partial \tilde{a}^\dagger}{\partial t} = D_a \frac{\partial^2 \tilde{a}^\dagger}{\partial x^2} - \alpha a^{\dagger *} \mathscr{K} \tilde{a} - \alpha a^* \mathscr{K} \tilde{a}^\dagger + \left(1 - \alpha a^* a^{\dagger *} \mathscr{K}'\right) \tilde{c}, \tag{2.25}$$

$$\varepsilon \frac{\partial \tilde{c}}{\partial t} = \varepsilon^2 \frac{\partial^2 \tilde{c}}{\partial x^2} + \alpha a^{\dagger *} \mathscr{K} \tilde{a} + \alpha a^* \mathscr{K} \tilde{a}^\dagger - \left(1 - \alpha a^* a^{\dagger *} \mathscr{K}'\right) \tilde{c}, \tag{2.26}$$

where $\mathscr{K} \equiv \mathscr{K}(c^*)$ and $\mathscr{K}' \equiv \mathscr{K}'(c^*)$. After removing tildes, the above system can be written in matrix form as

$$\varepsilon \frac{\partial \mathbf{w}}{\partial t} = D \frac{\partial^2 \mathbf{w}}{\partial x^2} + J\mathbf{w}, \tag{2.27}$$

where

$$D = \begin{pmatrix} D_a & 0 & 0 \\ 0 & D_a & 0 \\ 0 & 0 & \varepsilon^2 \end{pmatrix}, \qquad J = \begin{pmatrix} -f_a & -f_{a^\dagger} & -f_c \\ -f_a & -f_{a^\dagger} & -f_c \\ f_a & f_{a^\dagger} & f_c \end{pmatrix}. \tag{2.28}$$

Here, $\mathbf{w} = (\tilde{c}, \tilde{a}, \tilde{a}^{\dagger})^{\intercal}$ and

$$f(a, a^{\dagger}, c) = \alpha \mathscr{K}(c) a a^{\dagger} - c, \tag{2.29}$$

such that f_a, $f_{a^{\dagger}}$ and f_c denote partial derivatives of f with respect to a, $a^{\dagger}$ and c respectively.

For this model to exhibit patterning via a diffusion-driven instability, we require the SUSS to be linearly stable in the absence of diffusion ($D_a = 0$). In this case, eigenvalues of the Jacobian of the system (2.27) satisfy the characteristic equation

$$-\lambda^3 - \left(1 + a^* + a^{\dagger *}\right) \lambda^2 = 0, \tag{2.30}$$

which has roots $\lambda_{1,2} = 0$ and $\lambda_3 = f_c - f_a - f_{a^{\dagger}}$. The zero eigenvalues here reflect that the three-variable system (2.10)–(2.12) is in fact a single-variable system once the mass-conservation constraints (2.17) and (2.18) are applied. In the absence of feedback ($\mathscr{K} = 1$), we have $\lambda_3 = -1 - a^* - a^{\dagger *}$, which is negative since the (in this case, unique) SUSS is positive. Hence, the unique positive SUSS (a^*, $a^{\dagger *}$, c^*) is linearly stable in the absence of diffusion and feedback. However, in the presence of feedback ($\mathscr{K}$ is a monotonic increasing function), then the linear stability of the SUSS requires $\Delta < 0$, where we define $\Delta = f_c - f_a - f_{a^{\dagger}}$. Hence, the linear stability of the SUSS largely depends on the choice of functional form for the feedback and on parameter values.

In the presence of diffusion ($D_a \geq 0$), since no-flux boundary conditions are imposed we seek a solution to (2.27) of the form

$$\mathbf{w}(t) = \mathbf{w}_0 e^{\lambda t} \cos(\sigma x), \tag{2.31}$$

where $\mathbf{w}_0$ is a constant vector and $\sigma = n\pi$ for an integer n. Substituting this into (2.27), and requiring a non-trivial solution, we obtain the characteristic equation

$$0 = \lambda^3 - \tau_2\lambda^2 + \tau_1\lambda + h(\sigma^2), \tag{2.32}$$

where

$$\tau_2 = f_c - f_a - f_{a^\dagger} - (\varepsilon^2 + 2D_a)\sigma^2, \tag{2.33}$$

$$\tau_1 = (\varepsilon^2 + D_a)(f_a + f_{a^\dagger})\sigma^2 - 2D_a f_c\sigma^2 + D_a(2 + D_a\sigma^2)\sigma^2, \tag{2.34}$$

$$h(\sigma^2) = \varepsilon^2 D_a\sigma^6 + \varepsilon^2 D_a f_a\sigma^4 + \varepsilon^2 D_a f_{a^\dagger}\sigma^4 - D_a^2 f_c\sigma^4. \tag{2.35}$$

In the absence of feedback ($\mathscr{K} = 1$) the coefficients (2.33)–(2.35) are all positive. By Descartes' rule of signs, the above characteristic (2.32) has no positive eigenvalues. Thus, the positive SUSS (a^*, $a^{\dagger *}$, c^*) remains linearly stable in the absence of feedback, even in the presence of diffusion. In other words, this model cannot exhibit a diffusion-driven instability in the absence of a feedback interaction.

In the presence of a feedback interactions, the stability of the SUSS can be examined via the eigenvalues of the corresponding system (2.32). For $\sigma = 0$, the characteristic equation (2.32) has three solutions: $\lambda_{1,2} = 0$ and $\lambda_3 = f_c - f_a - f_{a^\dagger} \equiv \tau_0$. Hence, the SUSS is stable for $\sigma = 0$ if $\tau_0 < 0$.

For $\sigma \neq 0$, (2.32) has at least one root with negative real part if $\tau_2 < 0$ and $h(\sigma^2) > 0$. Now, since

$$\tau_2 = -(\varepsilon^2 + 2D_a)\sigma^2 + \tau_0, \tag{2.36}$$

we see that $\tau_2 < 0$ if $\tau_0 < 0$. Also, we note that

$$\begin{aligned} h(\sigma^2) &= \varepsilon^2 D_a^2 \sigma^6 - f_c D_a^2 \sigma^4 + f_c D_a \varepsilon^2 \sigma^4 - f_c D_a \varepsilon^2 \sigma^4 + f_a D_a \varepsilon^2 \sigma^4 + f_{a^\dagger} D_a \varepsilon^2 \sigma^4 \\ &= \varepsilon^2 D_a^2 \sigma^6 - f_c (D_a^2 - \varepsilon^2) \sigma^4 - \tau_0 \varepsilon^2 D_a \sigma^4 \end{aligned} \tag{2.37}$$

is positive if $f_c < 0$, since $D_a^2 \gg \varepsilon^2$ by assumption. If instead $f_c > 0$, then we define $0 < \pi \leq \sigma$, then

$$\begin{aligned} \frac{h(\sigma^2)}{\sigma^4} &= \varepsilon^2 D_a^2 \sigma^2 - f_c (D_a^2 - \varepsilon^2) - \tau_0 \varepsilon^2 \\ &\geq \varepsilon^2 D_a \pi^2 - f_c (D_a^2 - \varepsilon^2) - \tau_0 \varepsilon^2. \end{aligned} \tag{2.38}$$

This implies $\varepsilon^2 (D_a^2 \pi^2 + f_c - \tau_0) - f_c D_a^2 > 0$ as $\tau_0 < 0$, meaning that $f_c < f_a + f_{a^\dagger}$. We can then deduce the condition

$$D_a^2 > \varepsilon^2 > \frac{f_c D_a^2}{D_a^2 \pi^2 + f_c} > \frac{f_c D_a^2}{D_a^2 \pi^2 + f_a + f_{a^\dagger}}. \tag{2.39}$$

Hence, the right-hand side of (2.39) is less than D_a^2. Therefore, the SUSS is stable to perturbations as long as $\tau_0 < 0$ and $D_a^2 > \varepsilon^2$; otherwise, the condition

$$\tau_0 \equiv f_c - f_a - f_{a^\dagger} > 0 \tag{2.40}$$

suffices for the SUSS to be unstable to perturbations.

In summary, we have shown that the SUSS is always stable in the absence of diffusion and nonlinear feedback. In the presence of diffusion, the SUSS is still stable in the absence of feedback, hence, patterning cannot be obtained in this case. In the presence of nonlinear feedback, we hypothesise that the SUSS can lose stability if $\tau_0 > 0$, which depends on the

choice of the functional form of the nonlinear function $\mathscr{K}$. We verify our analytical results using specific feedback functional forms numerically in Section 2.2.3.

2.2.3 Numerical simulations

In this section we verify the above analytical results numerically and explore the patterning that can arise in this model.

We solve the system (2.10)-(2.12) numerically using the method of lines [52]. This method involves discretizing space into a mesh $x_i = i\Delta x$, for $i \in \{0,\dots,N\}$, and approximating second spatial derivatives using a central finite difference approximation. Using this method, the PDE system (2.10)-(2.12) is approximated by a large system of coupled ODEs governing the temporal evolution of the monomer and complex concentrations at each point in space. We then solve this ODE system numerically using a variable-step, variable-order method (implemented using the function `odeint` from `scipy.integrate` in Python). Unless otherwise stated, we use $N = 100$, so that $\Delta x = 0.01$, having verified that the numerical solution does not change significantly if a finer mesh is used.

Choice of feedback functions

For our numerical simulations, we must choose specific functional forms for our feedback function $\mathscr{K}$. We consider two functional forms, which reflect feedback that is either *non-saturating* (in the sense that there is no upper limit on the magnitude of $\mathscr{K}$) or *saturating* (in the sense that as the local complex concentration becomes large, $\mathscr{K}$ approaches some upper limit). The dimensional form of each feedback function is given by:

$$k(C) = \begin{cases} u + zC^2 & \text{(non-saturating)} \quad (2.41) \\ u + \dfrac{zC^2}{{K_m}^2 + C^2} & \text{(saturating)} \quad (2.42) \end{cases}$$

for real positive parameters u and z. To obtain the non-dimensionalised form of (2.41) and (2.42), we take $k_0 = u+z$ to be the rescaling factor in (2.9), obtaining

$$\mathscr{K}(c) = \begin{cases} \beta + c^2 & \text{(non-saturating)} \quad (2.43) \\ \beta + \dfrac{c^2}{\omega^2 + c^2} & \text{(saturating)} \quad (2.44) \end{cases}$$

where we define β by u/z and $u/(z(u+z)^2)$ in the non-saturating and saturating cases, respectively, and we define ω by $K_m/(u+z)$. Note that the rescaling factor k_0 corresponds to a baseline value of $k(C)$ in the non-saturating case (2.41), but to the maximal value of $k(C)$ in the saturating case (2.41).

Pattern formation for saturating and non-saturating feedback

We start by numerically verifying the linear stability analysis presented in Section 2.2.2 for the chosen functional forms of feedback (2.43)–(2.44). For a chosen parameter set, we plot the largest eigenvalue of the characteristic polynomial (2.32) in each case, verifying that there exists a range of values of σ for which this eigenvalue is positive, and thus we may expect to observe patterns (Fig. 2.2).

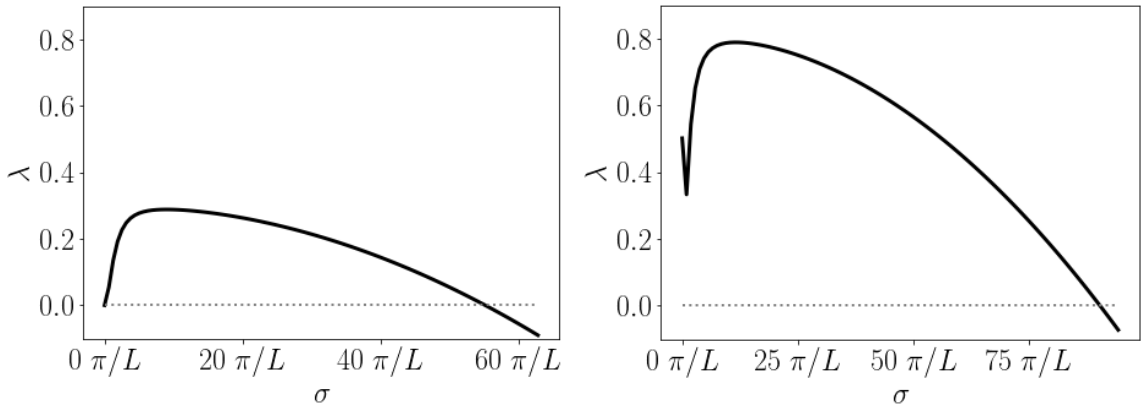

(a) (b)

Fig. 2.2 Plot of the largest eigenvalue of the characteristic polynomial (2.32) of the conservative PDE system (2.10)–(2.12), in the case of (a) non-saturating and (b) saturating feedback. Parameter values are $\alpha = 1$, $\beta = 0.05$, $\omega = 1$, $D_a = 1$, $\varepsilon = 0.01$, $a_T = 2.5$ and $a_T^\dagger = 2$.

We next simulate the PDE system (2.10)–(2.12) using initial condition

$$\begin{aligned} a(x,0) &= a_0 + 0.1\xi(x), \\ a^\dagger(x,0) &= a_0^\dagger + 0.1\xi^\dagger(x), \\ c(x,0) &= 0, \end{aligned} \tag{2.45}$$

where $\xi(x)$, $\xi^\dagger(x)$ denote independent standard uniform random variables at each point x, and the parameters a_0, $a_0^\dagger$ are determined in each simulation such that the total protein concentrations of a, $a^\dagger$ have the chosen values a_T, $a_T^\dagger$.

Fig. 2.3 shows the resulting dynamics over a timescale $t \sim O(1)$ for non-saturating and saturating feedback. We see that with non-saturating feedback, the system quickly develops multiple 'spike' in complex concentration, each with a different height (see the solution at time $t = 0.1$ in Fig. 2.3a), which collapse onto a single spike over time. With saturating feedback (Fig. 2.3b), the system also evolves to a pattern featuring multiple 'peaks', but these are wider and more mesa-like than in the non-saturating case, and have not yet collapsed onto a single peak by the end of the simulation.

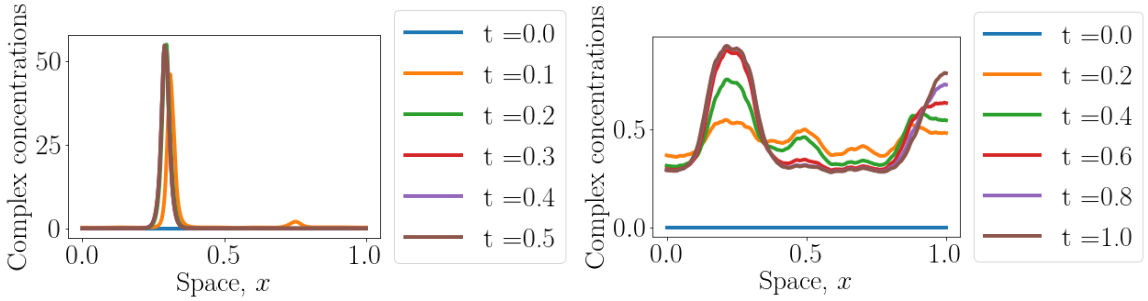

(a) Non-saturating feedback.

(b) Saturating feedback.

Fig. 2.3 Numerical solution of the mass conserved model (2.10)-(2.12) with no-flux boundary conditions (2.15) and initial condition (2.45) over short time scales. Solutions $c(x,t)$ are shown at the indicated times. Parameter values are $\varepsilon = 0.01$, $D_a = 1$, $\beta = 0.05$, $\omega = 1$, $a_T = 2.5$, $a_T^\dagger = 2$ and $\alpha = 0.5$.

Running our simulations over a longer timescale sheds more light on the stability of each pattern (Fig. 2.4.) Simulating each model up to $t = 25$, we find that for non-saturating feedback the system has quickly evolved to a stable, single spike solution (Fig. 2.4a). However, for saturating feedback the system has still not evolved to a single mesa solution by $t = 25$, with several additional smaller stable peaks still present by this time (Fig. 2.4b).

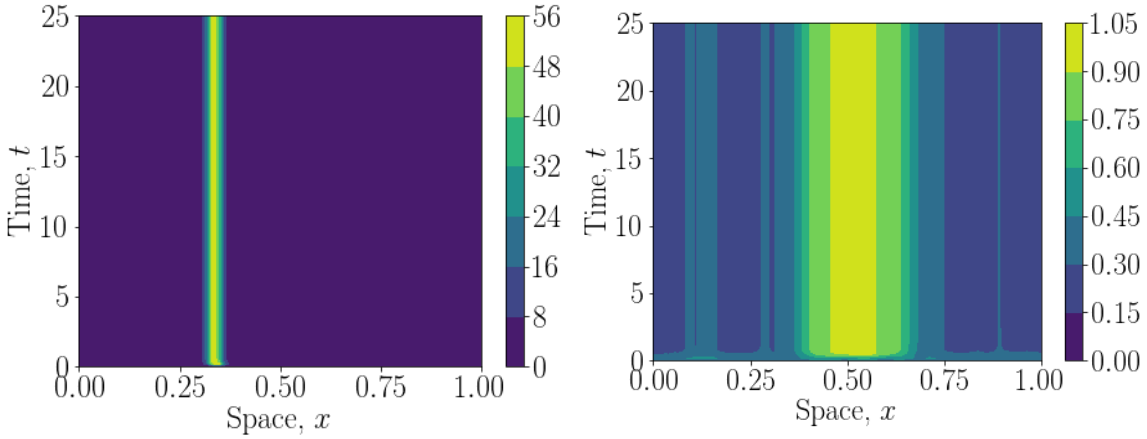

(a) Non-saturating feedback.

(b) Saturating feedback.

Fig. 2.4 Numerical solution of the mass conserved model (2.10)-(2.12) with no-flux boundary conditions (2.15) and initial condition (2.45) over longer time scales. Parameter values are $\varepsilon = 0.01$, $D_a = 1$, $\beta = 0.05$, $\omega = 1$, $a_T = 2.5$, $a_T^\dagger = 2$ and $\alpha = 0.5$.

Pattern dependence on model parameters and initial condition

To explore the effect of total protein concentrations on the system dynamics, we next simulate our model for a range of different values of a_T, while $a_T^\dagger$ is kept fixed. Fig. 2.5 shows that while in the case of non-saturating the resulting spike becomes higher as a_T increases (Fig. 2.5a–2.5c), for saturating feedback the single mesa retains approximately the same height (Fig. 2.5d–2.5e) for a range of values of a_T, above which the complex formation saturates over the whole domain and the system evolves to a SUSS (Fig. 2.5f).

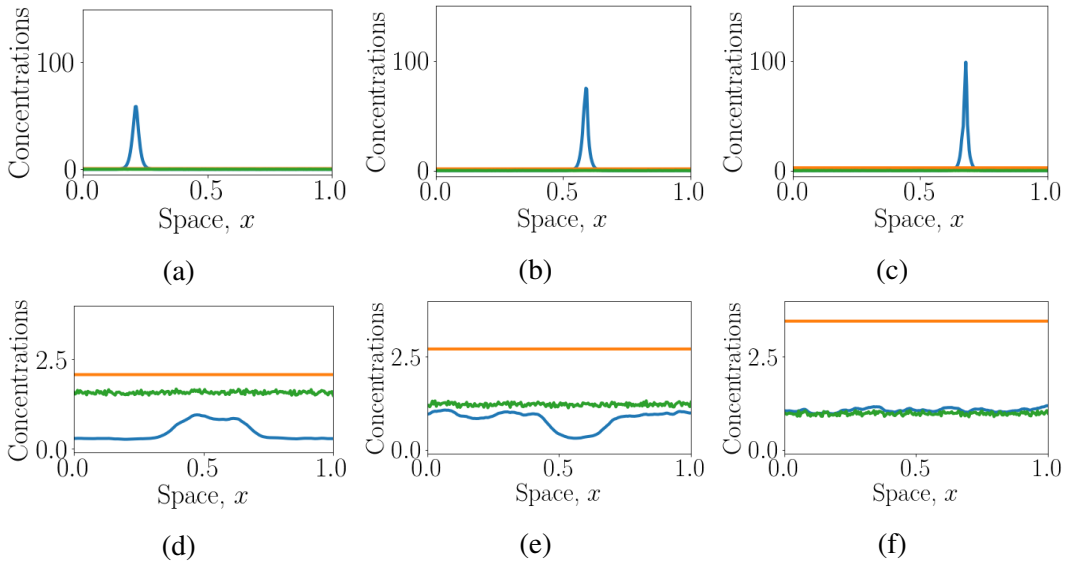

Fig. 2.5 Numerical solution of the mass conserved model (2.10)-(2.12) with no-flux boundary conditions (2.15) and initial condition (2.45) for a range of values of a_T. Upper row: non-saturating feedback; lower row: saturating feedback. Blue: c; orange: a; green: $a^\dagger$. Numerical solution shown at $t = 10$. Values of a_T are: (a and d) 2.5; (b and e) 3.5; (c and f) 4.5. Other parameter values are $\varepsilon = 0.01$, $D_a = 1$, $\beta = 0.05$, $\omega = 1$, $a_T^\dagger = 2$ and $\alpha = 0.5$.

We next extend our investigation to include the dependence of model dynamics on our choice of initial condition. We replace (2.45) with the initial condition

$$\begin{aligned} a(x,0) &= a_0 + 0.1(1+\cos(2\pi(kx+\phi))), \\ a^\dagger(x,0) &= a_0^\dagger + 0.1(1+\cos(2\pi(kx+\phi))), \\ c(x,0) &= 0, \end{aligned} \tag{2.46}$$

for specified values of phase angle $\phi \in [0,1)$ and wavenumber k, where a_0, $a_0^\dagger$ are as described for (2.45). By varying the parameter values in (2.46), we can investigate the dependence of the pattern on the shape of our initial 'stimulus'.

For non-saturating feedback, the results of our investigations are summarised in Fig. 2.6. For non-saturating feedback with relatively weak feedback and relatively little total protein concentration, we find that the system evolves to a single spike in complex concentration in

the centre of the spatial domain (Fig. 2.6a). A greater total protein concentration a_T results in this spike 'splitting' into two shorter (though approximately similarly wide) spikes of equal size, concomitant with a greater spatially uniform steady-state value of a (Fig. 2.6b and Fig. 2.6c). Multiple spikes can also be observed with relatively low total protein concentrations if instead we increase the feedback strength α (Fig. 2.6d and Fig. 2.6e), though in this case a sufficiently high total protein concentration a_T can result in a single, broader spike (Fig. 2.6f). A further increase in feedback strength can result in more than two spikes (Fig. 2.6g, Fig. 2.6h, and Fig. 2.6i).

In summary, for this choice of initial condition, we find that 'overexpression' of total protein concentration in one cell junction (while the other is fixed) leads to multiple 'stable' spikes in the non-saturating feedback model. In contrast, there is a range of 'intermediate' feedback strengths for which the saturating system exhibits a mesa-like pattern, above which it does not polarise.

We next explore the effect of varying the wavenumber k of the initial sinusoidal perturbation in (2.46) on the resulting pattern. In the case of saturating feedback, we find that the number of mesas increases as we increase the wavenumber of the initial 'stimulus' for certain intermediate feedback strengths (Fig. 2.7b, Fig. 2.7e, and Fig. 2.7h). In addition, increasing the feedback strength leads to narrower mesas (Fig. 2.7a, Fig. 2.7b, and Fig. 2.7c). However, if the feedback strength is too high, and seemingly if the wavenumber of the initial stimulus is too high, then the system no longer exhibits patterning (Fig. 2.7i). In the case of non-saturating feedback, we observe a single spike that changes its position as we vary the wavenumber k (results not shown).

We next verify that this model is capable of exhibiting multiple stable peaks, now assuming initial condition (2.46). Fig. 2.8 confirms that multiple stable spikes and mesas do seem possible in the case of non-saturating (Fig. 2.8a) and saturating (Fig. 2.8b), respectively, in an appropriate parameter regime.

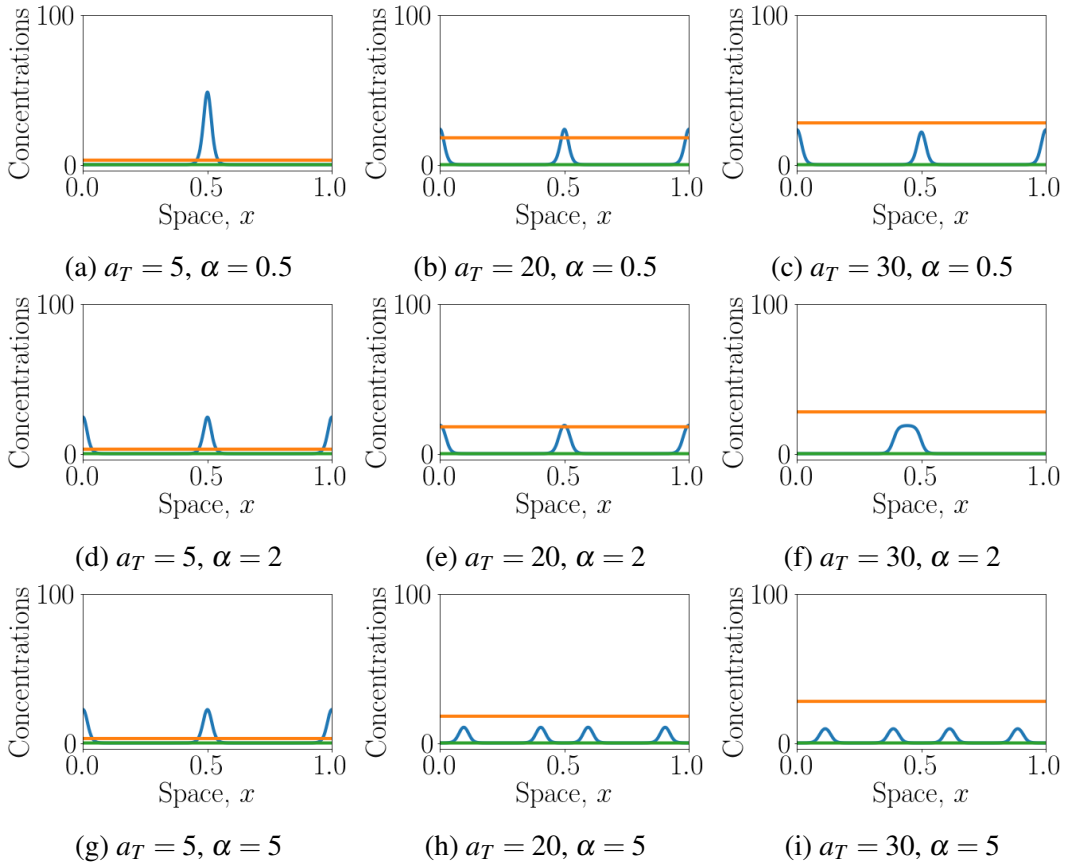

(a) $a_T = 5$, $\alpha = 0.5$ (b) $a_T = 20$, $\alpha = 0.5$ (c) $a_T = 30$, $\alpha = 0.5$

(d) $a_T = 5$, $\alpha = 2$ (e) $a_T = 20$, $\alpha = 2$ (f) $a_T = 30$, $\alpha = 2$

(g) $a_T = 5$, $\alpha = 5$ (h) $a_T = 20$, $\alpha = 5$ (i) $a_T = 30$, $\alpha = 5$

Fig. 2.6 Numerical solution of the mass conserved model (2.10)-(2.12) with no-flux boundary conditions (2.15) and initial condition (2.46), assuming non-saturating feedback, for a range of feedback strengths α and total protein concentrations a_T. Blue: c; orange: a; green: $a^\dagger$. Numerical solution shown at $t = 10$. Parameter values are $\varepsilon = 0.01$, $D_a = 1$, $\beta = 0.05$, $\omega = 1$, $a_T^\dagger = 2$, $\phi = 0$, $k = 2$.

Continuing this investigation, we next determine the number of patterns that arise in the system (2.10)-(2.12) relative to varying key parameters (Fig. 2.9). To generate this figure, we numerically solve the system with non-saturating (Fig. 2.9a) or saturating (Fig. 2.9b) feedback for different values of the feedback strength a and total protein concentration in one cell a_T, holding the total protein concentration in the other cell $a_T^\dagger$, along with all other parameters, fixed. In each case, we simulate the model for a sufficiently long time ($t = 50$) that it has appeared to numerically converged to a steady state. We then count the number of peaks in the pattern that is obtained, and colour this 'pixel' of the relevant figure according to whether: (i) there are no peaks, i.e. the system evolves to a SUSS; (ii) there is a single

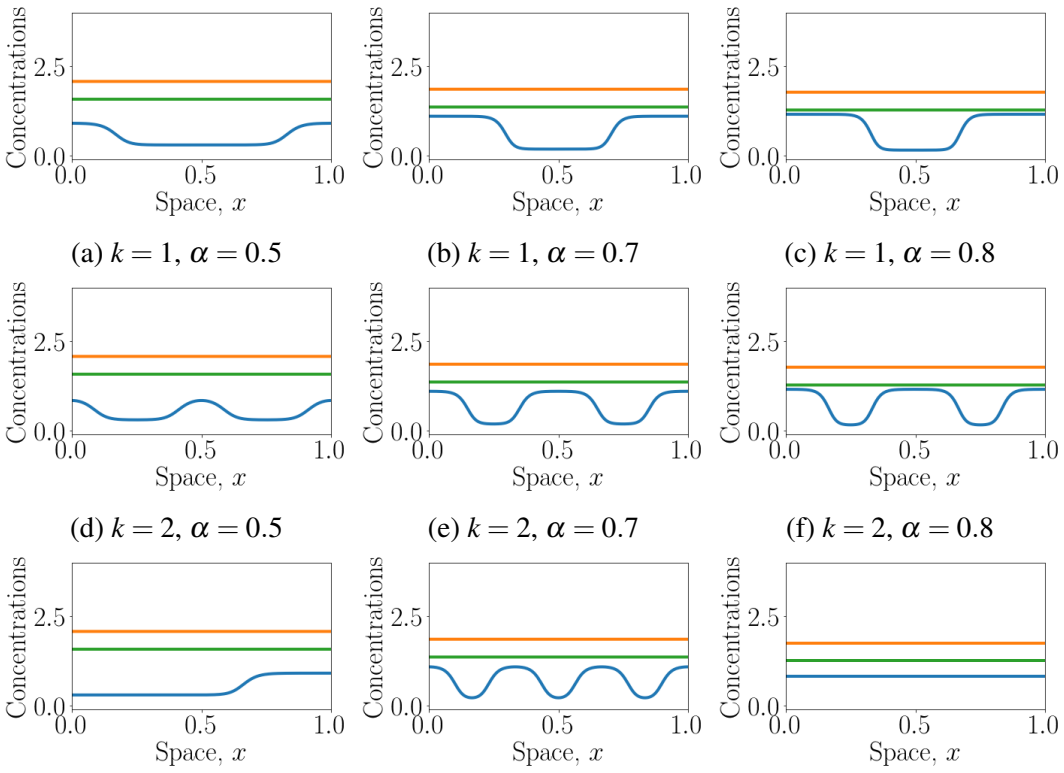

(a) $k = 1$, $\alpha = 0.5$ (b) $k = 1$, $\alpha = 0.7$ (c) $k = 1$, $\alpha = 0.8$

(d) $k = 2$, $\alpha = 0.5$ (e) $k = 2$, $\alpha = 0.7$ (f) $k = 2$, $\alpha = 0.8$

(g) $k = 3$, $\alpha = 0.5$ (h) $k = 3$, $\alpha = 0.7$ (i) $k = 3$, $\alpha = 0.8$

Fig. 2.7 Numerical solution of the mass conserved model (2.10)-(2.12) with no-flux boundary conditions (2.15) and initial condition (2.46), assuming saturating feedback, for a range of initial wavenumber k and feedback strength α. Blue: c; orange: a; green: $a^{\dagger}$. Numerical solution shown at $t = 10$. Parameter values are $\varepsilon = 0.01$, $D_a = 1$, $\beta = 0.05$, $\omega = 1$, $a_T^{\dagger} = 2$, $a_T = 2.5$, $\phi = 0$.

peak; (iii) there are multiple peaks. As Fig. 2.9 shows, for both non-saturating and saturating feedback, we find parameter sets for which (i)-(iii) are possible.

Of course, the 'stable' multiple peaks found in Fig. 2.8 and Fig. 2.9 may in fact be meta-stable, and coalesce into single peaks over a much longer timescale; we revisit this question in our concluding discussion.

In summary, our numerical simulations suggest that in general, higher total protein concentrations a_T lower the required feedback strength α for patterning to occur in this model, and vice versa. Increasing the feedback strength results in either narrower mesas or shorter spikes, depending on whether or not the feedback is saturating. However, while

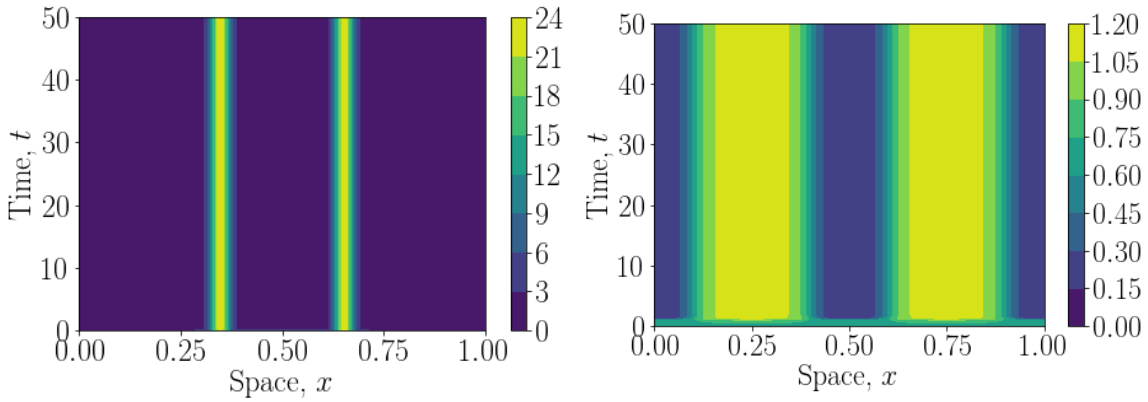

(a) Non-saturating feedback.

(b) Saturating feedback.

Fig. 2.8 Numerical solution of the mass conserved model (2.10)-(2.12) with no-flux boundary conditions (2.15) and initial condition (2.46) over longer time scales, assuming: (a) non-saturating feedback with parameter values $\alpha = 5$, $k = 1$, $a_T = 5$; (b) saturating feedback with parameter values $\alpha = 0.7$, $k = 2$, $a_T = 2.5$. Other parameter values are $\varepsilon = 0.01$, $D_a = 1$, $\beta = 0.05$, $\omega = 1$, $a_T = 2.5$, $a_T^\dagger = 2$, $\alpha = 0.5$, $\phi = 0.5$.

the number of mesas in the saturating feedback model depends only on the wavenumber of the initial condition, the non-saturating feedback model can exhibit multiple spikes given sufficiently high total protein concentration a_T or feedback strength α.

2.2.4 Asymptotic analysis

So far, we have used steady state and linear stability analysis, as well as numerical simulation, to explore the possible patterns that can arise in our mass-conserved model (2.10)–(2.12). We have found that with a range of parameter sets, this model exhibits spike-like patterns in the case of non-saturating feedback, and mesa-like patterns in the case of saturating feedback. We shall now restrict our focus on the latter case, since it arguably represents a more biologically plausible assumption, and because we are interested in the size, shape and location of mesas in this case. To this end, here we use singular perturbation theory to obtain an approximate half-mesa solution, and derive an algebraic expression for its spatial location. We then discuss how this may be extended to construct a whole mesa solution.

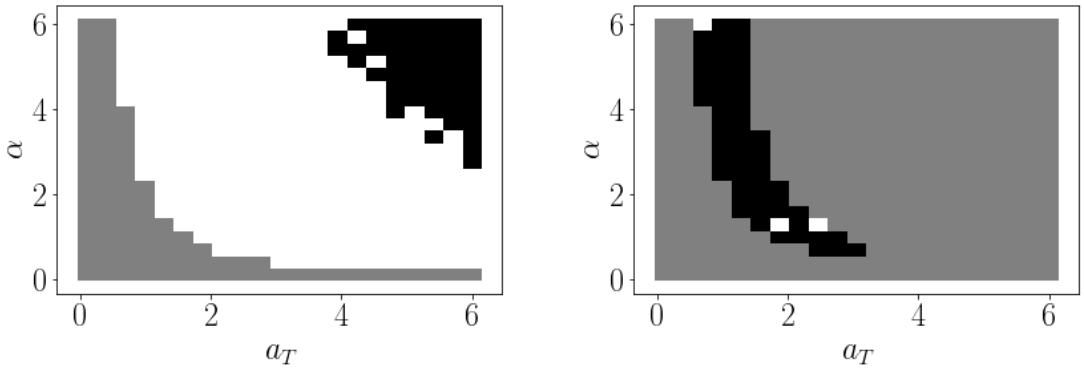

(a) Non-saturating feedback.

(b) Saturating feedback.

Fig. 2.9 Characterisation of steady-state solutions of the system (2.10)–(2.12) with no-flux boundary conditions (2.15) and initial condition (2.46) for a range of values of feedback strength α and total protein concentration a_T. Other parameter values are $\varepsilon = 0.01$, $D_a = 1$, $\beta = 0.05$, $\omega = 1$, $a_T = 2.5$, $a_T^\dagger = 2$, $\alpha = 0.5$, $\phi = 0.5$, and (a) $k = 1$, (b) $k = 2$. Steady state approximated by numerical solution at $t = 50$. Pixels are coloured according to whether the steady state exhibits no peaks (grey), a single peak (white), or multiple peaks (black).

Reduced mass conserved model

In the following, we make the following additional simplifying assumption that $a(x,t)$ and $a^\dagger(x,t)$ follow identical dynamics (for example, due to having identical initial conditions and total concentrations). This allows us to reduce our model (2.10)–(2.12) to a two-variable PDE system, which is more amenable to mathematical analysis.

The focus of our asymptotic analysis is thus on the two-component reaction-diffusion system given by

$$\varepsilon \frac{\partial a}{\partial t} = D_a \frac{\partial^2 a}{\partial x^2} + F(c,a), \tag{2.47}$$

$$\varepsilon \frac{\partial c}{\partial t} = \varepsilon^2 \frac{\partial^2 c}{\partial x^2} + G(c,a), \tag{2.48}$$

with boundary conditions

$$\frac{\partial a}{\partial x} = \frac{\partial c}{\partial x} = 0 \tag{2.49}$$

at $x = 0$ and $x = 1$, and the single conservation law

$$a_T = \int_0^1 (a(x,t) + c(x,t))\, \mathrm{d}x. \tag{2.50}$$

Here, for ease in the following analysis, we introduce the notation

$$F(a,c) = \alpha \left(\beta + \frac{c^2}{\omega^2 + c^2} \right) a^2 - c, \tag{2.51}$$

$$G(a,c) = -F(a,c), \tag{2.52}$$

reiterating that we shall restrict our focus to the case of saturating feedback throughout.

Existence of heteroclinic orbit and half-mesa solution

Recall from our numerical simulations (e.g. Fig. 2.7) that the full system (and thus, we shall assume, the reduced system) can exhibit 'mesa' patterns. Here, a mesa is characterised as two spatially uniform steady-state solutions, occupying distinct regions of space, which are smoothly connected. Mathematically, this corresponds to a *heteroclinic orbit* connecting the 'lower' and 'higher' steady states of the system.

For two-variable PDE systems of the general form (2.47)–(2.48), it has been shown [49, 53] that if the nonlinear function F satisfy the following mathematical properties:

P1: for a fixed value of $a \equiv \mathscr{A}$, F has distinct roots $c^{\pm}(\mathscr{A})$ and $c_m(\mathscr{A})$, such that

$$\frac{\partial F}{\partial c}(\mathscr{A}, c_{\pm}(\mathscr{A})) < 0 \quad \text{and} \quad \frac{\partial F}{\partial c}(\mathscr{A}, c_m(\mathscr{A})) > 0; \tag{2.53}$$

P2: The homogeneous steady states $(\mathscr{A}, c_{\pm}(\mathscr{A}))$ are the stable steady states of the system;

P3: The *Maxwell condition*

$$\int_{c^-(\mathscr{A})}^{c^+(\mathscr{A})} F(\mathscr{A},s)\,\mathrm{d}s = 0 \tag{2.54}$$

is satisfied;

then the system admits a heteroclinic orbit, corresponding to an *approximate* 'half mesa' solution. In our model, this approximate solution is given by

$$a(x) \approx \begin{cases} \mathscr{A} + \dfrac{F^+}{2}\left(\ell^2 - x^2\right) & \text{if } 0 \le x < \ell, \\ \mathscr{A} + F^-\left((x-\ell) + \frac{1}{2}(\ell^2 - x^2)\right) & \text{if } \ell < x \le 1, \end{cases} \tag{2.55}$$

and

$$c(x) \approx \begin{cases} c^+ + \dfrac{F^+F_a^+}{2G_c^+}\left(\ell^2 - x^2\right) & \text{if } 0 \le x < \ell, \\ c^- - \dfrac{F^-F_a^-}{G_c^-}\left((x-\ell) + \frac{1}{2}(\ell^2 - x^2)\right) & \text{if } \ell < x \le L, \end{cases} \tag{2.56}$$

where $F_a^\pm \equiv \partial F/\partial a(\mathscr{A}, c^\pm(\mathscr{A}))$ and $G_c^\pm \equiv \partial G/\partial c(\mathscr{A}, c^\pm(\mathscr{A}))$, and the location of the transition is defined by

$$\ell = \frac{F^-}{F^- - F^+}. \tag{2.57}$$

We now verify that our choice of saturating feedback function satisfies the above properties. First, we note that equations (2.16)–(2.18) for the SUSS can be reduced to the quartic equation

$$\begin{aligned} 0 =& \alpha(1+\beta)c^{*4} - (2\alpha(1+\beta)a_T + 1)c^{*3} + \alpha(a_T^2(1+\beta) + \beta\omega^2)c^{*2} - \omega^2(2\alpha\beta a_T + 1)c^* \\ &+ \alpha\beta\omega^2 a_T^2 \\ \equiv& f(c). \end{aligned} \tag{2.58}$$

By Descartes' rule of signs, (2.58) has at least two positive roots (which we denote $c^{\pm}$) if $a^4 > 3\omega^2/\alpha^2(1+\beta)^2$. Fig. 2.10a illustrates this situation for some fixed parameters. For a non-zero fixed value of a that is determined by a_T, it is straightforward to see that $c_{\pm}$ are both stable fixed points of the ODE $dc/dt = f(c)$, while the two remaining roots (which we denote $c_m \in (c^-, c^+)$ and $c_{\text{out}} > c^+$) are unstable fixed points. Hence, the properties **P1** and **P2** are satisfied.

Next, consider the integral

$$\begin{aligned} I &= \int_{c_-}^{c_+} \left[\alpha \left(\frac{c^2}{\omega^2 + c^2} + \beta \right) \mathscr{A}^2 - c \right] \mathrm{d}c \\ &= \alpha \mathscr{A}^2 \left\{ (1+\beta)(c_+ - c_-) - \omega \left(\tan^{-1}\left(\frac{c_+}{\omega}\right) - \tan^{-1}\left(\frac{c_-}{\omega}\right) \right) + \omega^2 (c_- - c_+) \right\} \\ &\quad - \frac{1}{2}(c_+^2 - c_-^2). \end{aligned} \tag{2.59}$$

Fig. 2.10a provides a numerical example where the integral (2.59) vanishes, thus verifying that property **P3** is satisfied. We conclude by demonstrating that the linear stability condition (2.40) is satisfied for our chosen feedback function and parameter values (Fig. 2.10b).

Having verified that our choice of the function F in the reduced mass conserved model (2.47)-(2.48) satisfy the properties **P1**–**P3**, we can now construct a half-mesa solution that connects the lower SUSS (c_-) to the upper SUSS (c_+). This solution is given by (2.55)–(2.56). In particular, the location of the half mesa (and thus the width of any mesas in a mesa-like pattern) depends on the total concentration of a, the fixed value of $\mathscr{A}$ and the stable steady states $c^{\pm}$. These high and low states are connected by an interface region [54]. In the phase plane, this interface region is characterised by a heteroclinic orbit in the case of mesa patterns (and a homoclinic orbit in the case of spikes; results not shown) [55].

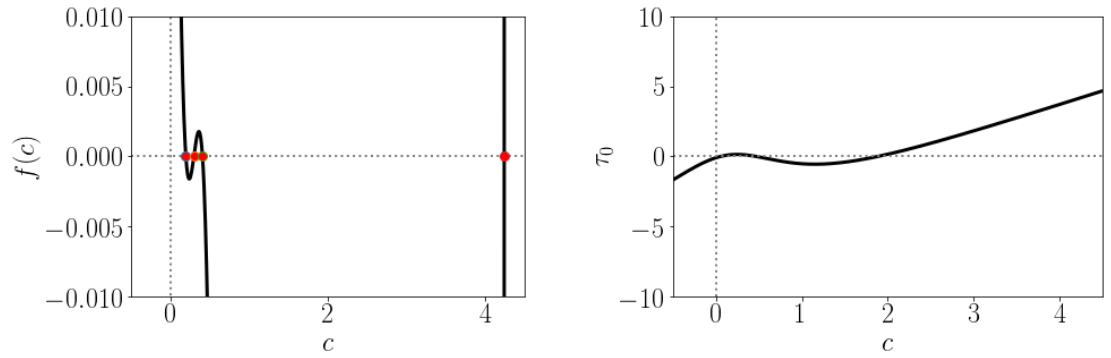

(a) (b)

Fig. 2.10 Steady states and linear stability of the reduced mass conserved model (2.47)-(2.48) in the case of saturating feedback with $\alpha = 0.955$, $\beta = 0.025$, $\omega = 1$ and $a_T = 2$. (a) Graph of $f(c) \equiv f(\mathscr{A}, c)$ defined by (2.58). Red dots denote the roots $c^- \approx 0.2$, $c_m \approx 0.29$, $c^+ \approx 0.41$, and $c_{\text{out}} \approx 4.1$. For the chosen parameter values, the integral of $f(c)$ between the first and third roots is zero, and thus the Maxwell condition (property **P3**) is satisfied. (b) Numerical verification that condition (2.40) is satisfied for the chosen parameter values.

Comparison with asymptotic analysis

We conclude this section by comparing the numerical solution of the reduced PDE system (2.47)–(2.48) with saturating feedback, and the approximated location of the half-mesa, with the approximate form obtained by asymptotic analysis. We use Newton's method and used a solution guess of the hyperbolic tangent that is closed to the actual mesa-type solution. We then solve the boundary value problem associated with the PDE system (2.47)–(2.48). The results are shown in Fig. 2.11a. We see a good agreement between the numerical and asymptotic solution, with the former exhibiting a consistently slightly lower complex concentration c than the latter.

Having identified the half-mesa solution (2.55)–(2.57), it is possible use this to construct steady-state solutions of the reduced mass conserved model (2.47)–(2.48) featuring multiple mesas, using the reflection theory proposed by Nishiura [56].

This theory precisely reflects the half-mesa solution and fits it into the spatial domain by rescaling the diffusion coefficient of a: if we require n half-mesas in our pattern, then we

replace D_a by D_a/n^2. Fig. 2.11b illustrates an example construction featuring 4 half-mesas, i.e. 2 full mesas. (We emphasise that these are solutions to the steady-state system, though the reflection theory itself tells us nothing about their *stability*.)

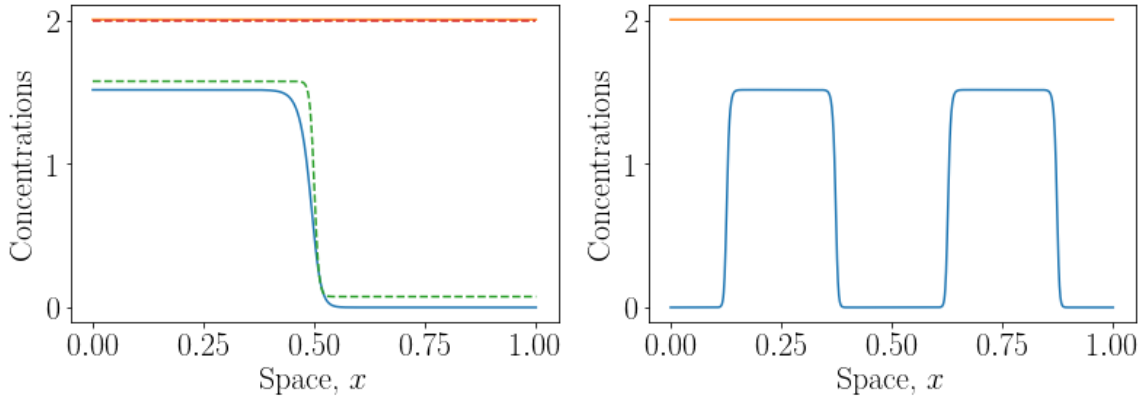

(a) (b)

Fig. 2.11 (a) Comparison of numerical solution and asymptotic approximation of a half-mesa exhibited by the reduced mass conserved model (2.47)–(2.48) with saturating feedback. Solid curve: numerical solution obtained using Newton's method; dashed curve: asymptotic approximation (2.55)–(2.57). (b) Construction of higher-order solutions, corresponding to multiple mesas, using the reflection theory proposed by Nishiura [56]. Blue/green: c; orange/red: a. Parameter values are $\varepsilon = 0.01$, $\beta = 0.05$, $\omega = 1$, $D = 1$ and $a(0) = 2.5$.

In this section, we applied perturbation theory to the reduced PDE system (2.47)–(2.48) with the saturating feedback introduced in Section 2.2. We used techniques from the literature to derive an algebraic expression for the location of the transition in the case of a half-mesa solution. In the next section, we explore how our analytic, numerical, and asymptotic results are affected if we 'break' the assumption of mass conservation by introducing protein trafficking to and from the plasma membrane.

2.3 Breaking mass conservation through protein trafficking

The formation and regulation of membrane subdomains depends on the active exchange of cytosolic material within the cell membrane [57]. This process is referred to as 'recycling'. Since the clustering process on its own could lead to ever larger clusters, it is reasonable to

expect there is some form of removal mechanism to balance the distribution of cluster sizes. One possible mechanism is endocytosis, a form of trafficking from the plasma membrane to the cytosol that, in the case of the cell-cell adhesion protein E-cadherin for example, may specifically target larger clusters [4]. In this section, we explore how such trafficking affects the resulting formation of patterns in our model. In particular, we address whether the addition of an extra constant source term and a linear degradation term to our original model presented in Section 2.2 affects patterning.

2.3.1 Governing equations

Biologically, we may describe the flux of proteins and complexes to and from cell-cell junctions, respectively, by introducing monomer trafficking and complex recycling. Mathematically, we assume that the molecules A and $A^\dagger$ are deposited to the membrane at a fixed rate J_{on}. Additionally, both monomers and the complex are assumed to be removed at rates of ${J^A}_{\text{off}}$ and ${J^C}_{\text{off}}$, respectively. Since in the present work we are not interested in the *distribution* of puncta sizes, but just in the formation and stability of puncta of any size, we assume that the complex C could generally represent a cluster of any size. Thus, the system of governing equations for our adapted model given by

$$\frac{\partial A}{\partial T} = D_A \frac{\partial^2 A}{\partial X^2} + J_{\text{on}} - {J^A}_{\text{off}} A - kAA^\dagger + vC, \tag{2.60}$$

$$\frac{\partial A^\dagger}{\partial T} = D_A \frac{\partial^2 A^\dagger}{\partial X^2} + J_{\text{on}} - {J^A}_{\text{off}} A^\dagger - kAA^\dagger + vC, \tag{2.61}$$

$$\frac{\partial C}{\partial T} = D_C \frac{\partial^2 C}{\partial X^2} - {J^C}_{\text{off}} C + kAA^\dagger - vC. \tag{2.62}$$

Considering the same boundary and initial conditions (2.5)–(2.6), the above system is not conserved. In the absence of cluster depletion J_{off}, the protein concentration on both cell edges would eventually saturate to the junction in a monomeric form. On the other hand, large clusters would only remain on junctions when monomer deposition rate J_{on} is absent.

Using the same scaling in Section 2.2.1, and substituting into the system (2.60)–(2.62), we obtain the non-dimensionalised system

$$\varepsilon\frac{\partial a}{\partial t} = D_a\frac{\partial^2 a}{\partial x^2} + j_{\text{on}} - j^a{}_{\text{off}}a - \alpha\mathscr{K}(c)aa^\dagger + c, \tag{2.63}$$

$$\varepsilon a_t^\dagger = D_a\frac{\partial^2 a^\dagger}{\partial x^2} + j_{\text{on}} - j^a{}_{\text{off}}a^\dagger - \alpha\mathscr{K}(c)aa^\dagger + c, \tag{2.64}$$

$$\varepsilon\frac{\partial c}{\partial t} = \varepsilon^2\frac{\partial^2 c}{\partial x^2} - j^c{}_{\text{off}}c + \alpha\mathscr{K}(c)aa^\dagger - c, \tag{2.65}$$

where we define the dimensionless parameters

$$j_{\text{on}} = \frac{J_{\text{on}}}{k_0 v}, \qquad j^a{}_{\text{off}} = \frac{J^A{}_{\text{off}}}{v}, \qquad j^c{}_{\text{off}} = \frac{J^C{}_{\text{off}}}{v}. \tag{2.66}$$

and the parameters α, ε, and D_a are as defined in (2.9). Note that we assume that only the binding rate depends on the complex concentration, as in Sections 2.2 and 2.2.4.

Following a similar simplification to Section 2.2.4, we now further assume that the unbound protein concentrations a and $a^\dagger$ on either side of the cell-cell junction behave identically ($a \equiv a^\dagger$). This leads to the reduced non-dimensionalised system

$$\varepsilon\frac{\partial a}{\partial t} = D_a\frac{\partial^2 a}{\partial x^2} + j_{\text{on}} - j^a{}_{\text{off}}a - \alpha\mathscr{K}(c)a^2 + c, \tag{2.67}$$

$$\varepsilon\frac{\partial c}{\partial t} = \varepsilon^2\frac{\partial^2 c}{\partial x^2} - j^c{}_{\text{off}}c + \alpha\mathscr{K}(c)a^2 - c, \tag{2.68}$$

where as before, we either have $\mathscr{K} = 1$ (corresponding to no feedback) or $\mathscr{K}$ is a monotonic increasing function of the form (2.43) or (2.44) (corresponding to non-saturating or saturating feedback, respectively).

2.3.2 Steady-state and stability analysis

Existence and uniqueness of positive SUSS

As in Section 2.2.2, we seek positive spatially uniform steady-state solutions (SUSS) of the form $a(x,t) \equiv a^*$ and $c(x,t) \equiv c^*$. Substituting into our model (2.67)–(2.68), we find that any SUSS must satisfy

$$j_{\text{on}} - j^a_{\text{off}} a^* - j^c_{\text{off}} c^* = 0, \tag{2.69}$$

$$j^c_{\text{off}} c^* - \alpha \mathscr{K}(c^*) a^{*2} + c^* = 0. \tag{2.70}$$

We use (2.69) to eliminate a^* from (2.70) to get

$$(j^a_{\text{off}})^2 (j^c_{\text{off}} + 1) c^* - \alpha \mathscr{K}(c^*) (j^c_{\text{off}} c^* - j_{\text{on}})^2 = 0. \tag{2.71}$$

In the absence of feedback ($\mathscr{K} = 1$), (2.71) simplifies to the quadratic equation

$$\alpha (j^c_{\text{off}})^2 c^{*2} - (2\alpha j_{\text{on}} j^c_{\text{off}} + (j^a_{\text{off}})^2 (j^c_{\text{off}} + 1)) c^* + \alpha j^2{}_{\text{on}} = 0, \tag{2.72}$$

which has two real positive roots. The unique admissible root is the one that is given by

$$c^* = \frac{1}{2\alpha (j^c_{\text{off}})^2} \left(M - \sqrt{M^2 - 4\alpha^2 (j^c_{\text{off}})^2 j^2_{\text{on}}} \right), \tag{2.73}$$

where we define $M \equiv 2\alpha j_{\text{on}} j^c_{\text{off}} + (j^a_{\text{off}})^2 (j^c_{\text{off}} + 1)$. The corresponding root for a can be obtained using (2.69).

In the presence of monotonic increasing feedback, the existence of the SUSS depends on the feedback parameters. We examine the saturating and non-saturating feedback behaviours numerically in Section 2.3.3.

Linear stability of SUSS

To examine the linear stability of the positive SUSS (a^*, c^*), we introduce small perturbations $\tilde{a}$ and $\tilde{c}$, such that $a = a^* + \tilde{a}$ and $c = c^* + \tilde{c}$, as in Section 2.2.2. Substituting into (2.67) and (2.68) and dropping the higher-order terms, we obtain the linearised system

$$\varepsilon \frac{\partial \tilde{a}}{\partial t} = D_a \frac{\partial^2 \tilde{a}}{\partial x^2} - (2\alpha a^* \mathscr{K} + j^a_{\text{off}})\,\tilde{a} + \left(1 - \alpha a^{*2} \mathscr{K}'\right)\tilde{c}, \tag{2.74}$$

$$\varepsilon \frac{\partial \tilde{c}}{\partial t} = \varepsilon^2 \frac{\partial^2 \tilde{c}}{\partial x^2} + 2\alpha a^* \mathscr{K}\,\tilde{a} - \left(1 - \alpha a^{*2} \mathscr{K}' + j^c_{\text{off}}\right)\tilde{c}, \tag{2.75}$$

where $\mathscr{K} \equiv \mathscr{K}(c^*)$ and $\mathscr{K}' \equiv \mathscr{K}'(c^*)$. This above system can be written in matrix form as

$$\varepsilon \frac{\partial \mathbf{w}}{\partial t} = D \frac{\partial^2 \mathbf{w}}{\partial x^2} + J\mathbf{w}. \tag{2.76}$$

where $\mathbf{w} = (\tilde{a}, \tilde{c})^\intercal$ and

$$D = \begin{pmatrix} D_a & 0 \\ 0 & \varepsilon^2 \end{pmatrix}, \qquad J = \begin{pmatrix} -2\alpha a^* \mathscr{K} - j^a_{\text{off}} & 1 - \alpha a^{*2} \mathscr{K}' \\ 2\alpha a^* \mathscr{K} & -(1 - \alpha a^{*2} \mathscr{K}' + j^c_{\text{off}}) \end{pmatrix}. \tag{2.77}$$

For spatial patterning in this model, in the absence of diffusion ($D_a = 0$) we require the SUSS to be linearly stable. Eigenvalues λ of the Jacobian of the system (2.76) satisfy the characteristic equation

$$\lambda^2 + \left(2\alpha a^* \mathscr{K} + 1 + j^a_{\text{off}} + j^c_{\text{off}} - \alpha a^{*2} \mathscr{K}'\right)\lambda + j^a_{\text{off}}\left(1 + j^c_{\text{off}} - \alpha a^{*2} \mathscr{K}'\right) + 2\alpha a^* j^c_{\text{off}} \mathscr{K} = 0. \tag{2.78}$$

In the absence of feedback ($\mathscr{K} \equiv 1$), Descartes' rule of signs implies that the roots of (2.78) are all negative and hence, the spatially uniform steady state (a^*, c^*) is linearly stable. In the case of nonlinear feedback (saturating or non-saturating feedback), the SUSS will always be

stable as long as

$$\alpha \leq \frac{1 + j^c{}_{\text{off}}}{a^{*2}\mathscr{K}'}. \tag{2.79}$$

In the presence of diffusion ($D_a > 0$), since no-flux boundary conditions are imposed we seek a solution to (2.76) of the form

$$\mathbf{w}(x,t) = \mathbf{w}_0 e^{\lambda t}\cos(\sigma x), \tag{2.80}$$

where $\mathbf{w}_0$ is a constant vector and $\sigma = n\pi$ for an integer n. Substituting this into (2.76), we obtain the characteristic equation

$$\lambda^2 + \left(2\alpha a^*\mathscr{K} + j^a{}_{\text{off}} + \sigma^2 D_a + \sigma^2\varepsilon^2 + 1 + j^c{}_{\text{off}} - \alpha a^{*2}\mathscr{K}'\right)\lambda + h(\sigma^2) = 0, \tag{2.81}$$

where

$$\begin{aligned} h(\sigma^2) = {} & \sigma^4 D_a\varepsilon^2 + \sigma^2 D_a\left(1 + j^c{}_{\text{off}} - \alpha a^{*2}\mathscr{K}'\right) + \sigma^2\varepsilon^2\left(2\alpha a^*\mathscr{K} + j^a{}_{\text{off}}\right) \\ & + \left(1 + j^c{}_{\text{off}} - \alpha a^{*2}\mathscr{K}'\right) j^a{}_{\text{off}} + 2\alpha a^*\mathscr{K}\, j^c{}_{\text{off}}. \end{aligned} \tag{2.82}$$

In the absence of feedback ($\mathscr{K} \equiv 1$, $\mathscr{K}' = 0$), we find that all roots of (2.81) are negative, hence the SUSS is linearly stable even in the presence of diffusion. In the presence of feedback, the SUSS becomes unstable if

$$\tau_0 \equiv 1 + j^c{}_{\text{off}} - \alpha a^{*2}\mathscr{K}' < 0. \tag{2.83}$$

The sign of τ_0 depends on the choice of the feedback function and parameter values.

In summary, we find that the SUSS is always linearly stable in the absence of diffusion. In the presence of diffusion, however, there are some restrictions regarding the model

parameters, via the condition (2.83), for a patterning instability to arise in the presence of feedback. In the next section we verify these analytical results numerically using specific feedback functional forms numerically.

2.3.3 Numerical simulations

Throughout this section, we refer to the non-saturating and saturating feedback functions defined by (2.43) and (2.44). We also assume that protein complexes are trafficked more rapidly than unbound proteins (${j^c}_{\text{off}} \gg {j^a}_{\text{off}}$). We simulate the system (2.63)-(2.65) numerically using the same boundary and initial conditions, and numerical method, as described in Section 2.2.3.

Pattern formation for saturating and non-saturating feedback

We start by numerically verifying the linear stability analysis presented in Section 2.3.2 for the chosen functional forms of feedback. For a chosen parameter set, we plot the largest eigenvalue of the characteristic polynomial (2.81) in each case, verifying that there exists a range of values of σ for which this eigenvalue is positive, and thus we may expect to observe patterns (Fig. 2.12).

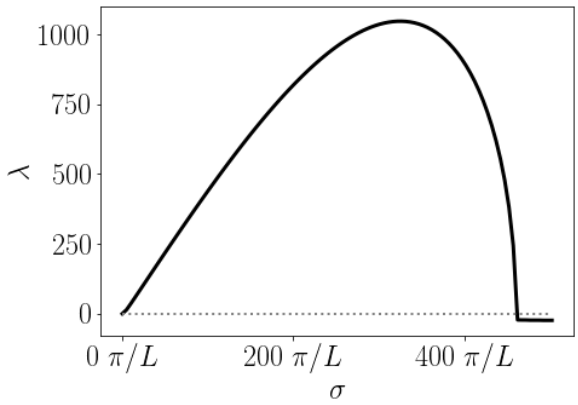

Fig. 2.12 Plot of the largest positive eigenvalue of the characteristic polynomial (2.81) of the reduced non-conservative model (2.67)–(2.67). Parameter values are $\alpha = 1$, $\beta = 0.05$, $\omega = 1$, $D_a = 1$, $a_T = 2.5$ and $a_T^\dagger = 2$.

We next simulate the full non-conservative model (2.63)–(2.65) using initial condition (2.45). Fig. 2.12 shows the resulting dynamics over a timescale $t \sim O(1)$. We see that with non-saturating feedback (Fig. 2.13a), the system quickly evolves to a single spike in complex concentration, while with saturating feedback (Fig.2.13b), the system evolves to a pattern featuring multiple mesas. These dynamics are similar to those observed in the mass conserved model.

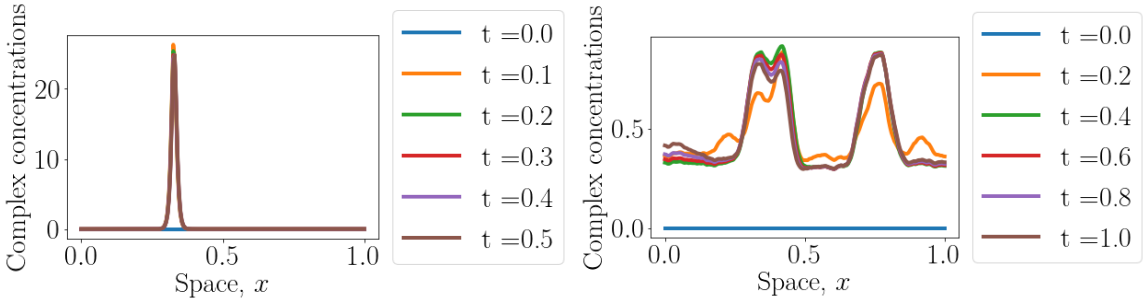

(a) Non-saturating feedback.

(b) Saturating feedback.

Fig. 2.13 Numerical solution of the non-conservative model (2.63)-(2.65) with no-flux boundary conditions (2.15) and initial condition (2.45), with (a) non-saturating and (b) saturating feedback respectively, over short time scales. Solutions $c(x,t)$ are shown at the indicated times. Parameter values are $a_T(0) = 2.5$, $a_T^\dagger(0) = 2$, $\alpha = 0.5$, $\beta = 0.05$, $\omega = 1$, ${j^a}_{\text{off}} = 0.1$, ${j^c}_{\text{off}} = 1.5$, $j_{\text{on}} = 1$, $D_a = 1$, and $\varepsilon = 0.01$.

We next investigate the dependence of the pattern on the shape of our initial 'stimulus' (2.46). In the case of non-saturating feedback, we find that multiple spike solutions are obtained when varying the feedback strength and the initial total protein concentrations (Fig. 2.14). For feedback strength $\alpha = 1$, and sufficiently high initial concentration a, the model generates multiple transient spikes in the middle of the domain (Fig. 2.14e and 2.14f). However, these patterns are not stable.

The non-conserved system with saturating feedback also exhibits multiple mesas (Fig. 2.15). In fact, the wavenumber of the initial 'stimulus', along with sufficiently high feedback strength, determines the number of mesas: if the feedback strength $\alpha = 1$, for instance, then we can obtain up to four mesas within the domain depending on the initial wavenumber (k).

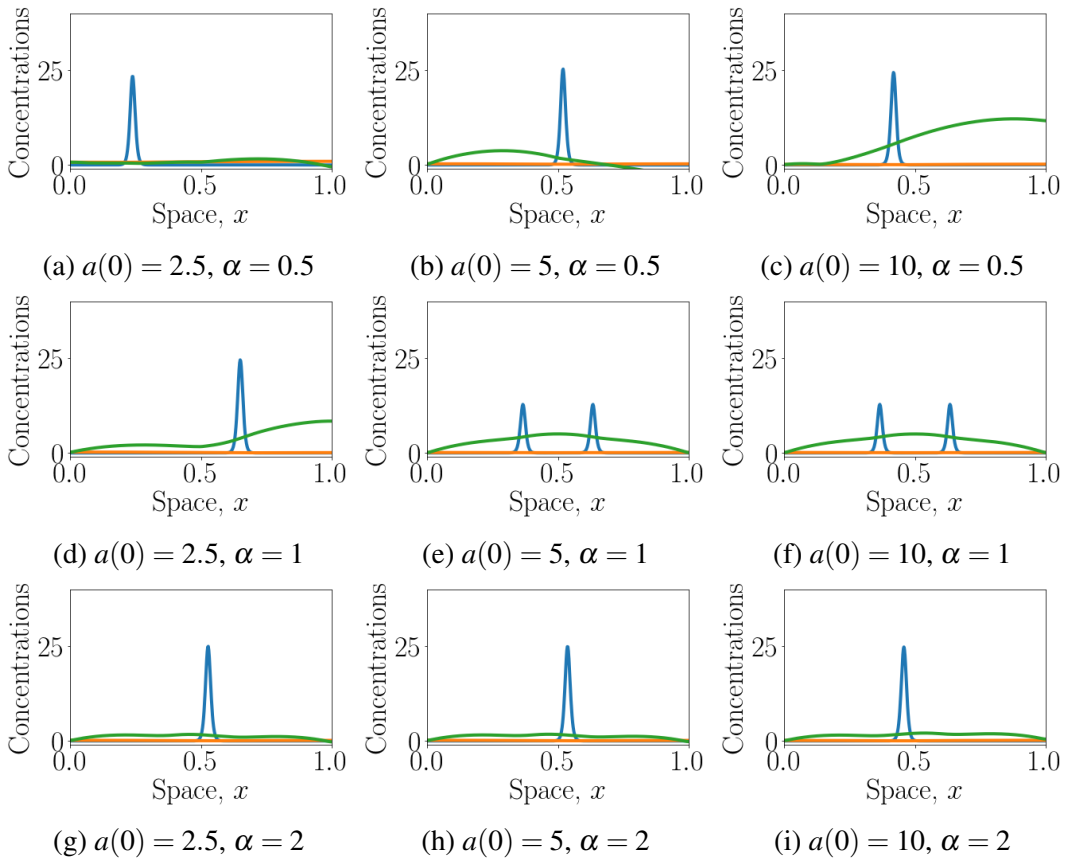

(a) $a(0) = 2.5$, $\alpha = 0.5$ (b) $a(0) = 5$, $\alpha = 0.5$ (c) $a(0) = 10$, $\alpha = 0.5$

(d) $a(0) = 2.5$, $\alpha = 1$ (e) $a(0) = 5$, $\alpha = 1$ (f) $a(0) = 10$, $\alpha = 1$

(g) $a(0) = 2.5$, $\alpha = 2$ (h) $a(0) = 5$, $\alpha = 2$ (i) $a(0) = 10$, $\alpha = 2$

Fig. 2.14 Numerical solution of the non-conservative model (2.63)-(2.65) with no-flux boundary conditions (2.15) and initial condition (2.46), assuming non-saturating feedback, for a range of feedback strengths α and initial protein concentrations $a(0)$. Blue: c; orange: a; green: $a^{\dagger}$. Numerical solution shown at $t = 10$. Parameter values are $a_T^{\dagger}(0) = 2$, $\alpha = 0.5$, $\beta = 0.05$, $\omega = 1$, $j^a{}_{\text{off}} = 0.1$, $j^c{}_{\text{off}} = 1.5$, $j_{\text{on}} = 1$, $D_a = 1$, $\varepsilon = 0.01$, $\phi = 0$.

Beyond that, the number of mesas will decrease again to a single final mesa, which localises to the middle of the spatial domain.

Fig. 2.16b gives us more insight into the early generation of multiple mesas, and their eventual coalesence into a single mesa over time, in the presence of saturating feedback. Finally, we note that for certain parameter values, the complex concentration in the saturating feedback model can exhibit spatio-temporal oscillations (Fig. 2.16b and Fig. 2.17). This behaviour is qualitatively distinct to the stable patterns that we observed for all parameter sets considered in the mass conserved model in Section 2.2. This behaviour may correspond to an oscillation between two steady states that are close enough to each other.

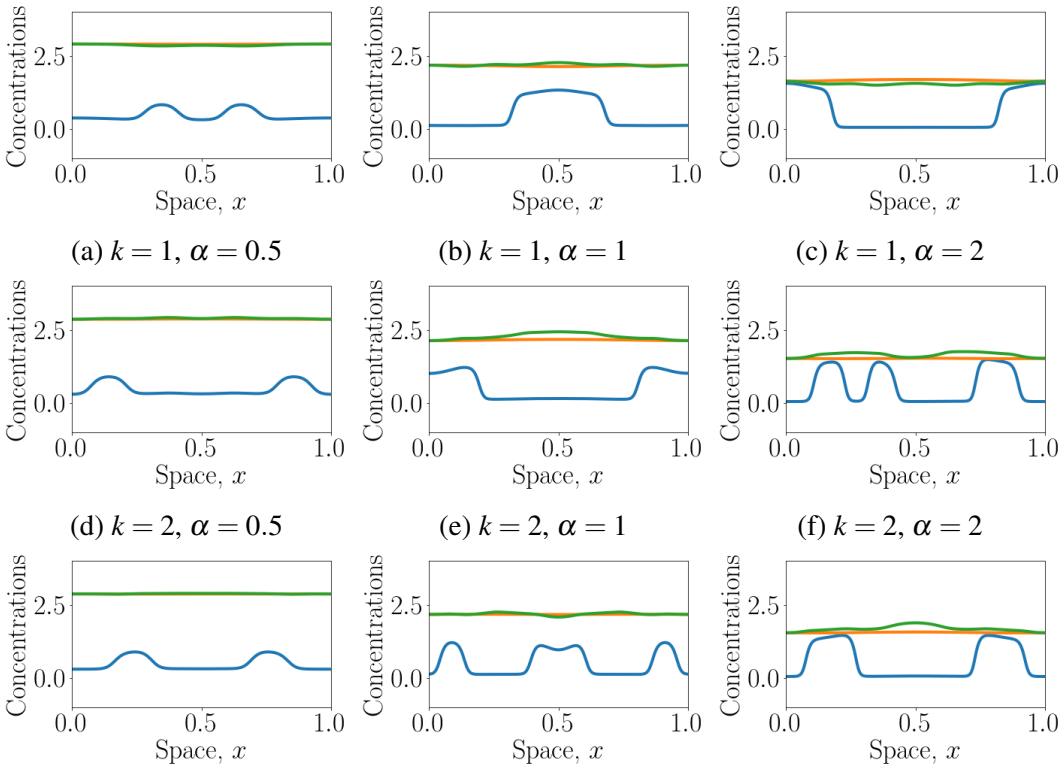

(a) $k = 1$, $\alpha = 0.5$ (b) $k = 1$, $\alpha = 1$ (c) $k = 1$, $\alpha = 2$

(d) $k = 2$, $\alpha = 0.5$ (e) $k = 2$, $\alpha = 1$ (f) $k = 2$, $\alpha = 2$

(g) $k = 3$, $\alpha = 0.5$ (h) $k = 2$, $\alpha = 1$ (i) $k = 3$, $\alpha = 2$

Fig. 2.15 Numerical solution of the non-conservative model (2.63)-(2.65) with no-flux boundary conditions (2.15) and initial condition (2.46), assuming saturating feedback, for a range of initial wavenumbers k and feedback strengths α. Blue: c; orange: a; green: $a^\dagger$. Numerical solution shown at $t = 10$. Parameter values are $a^\dagger(0) = 2$, $\alpha = 0.5$, $\beta = 0.05$, $\omega = 1$, $j^a{}_{\text{off}} = 0.1$, $j^c{}_{\text{off}} = 1.5$, $j_{\text{on}} = 1$, $D_a = 1$, $\varepsilon = 0.01$, $\phi = 0$.

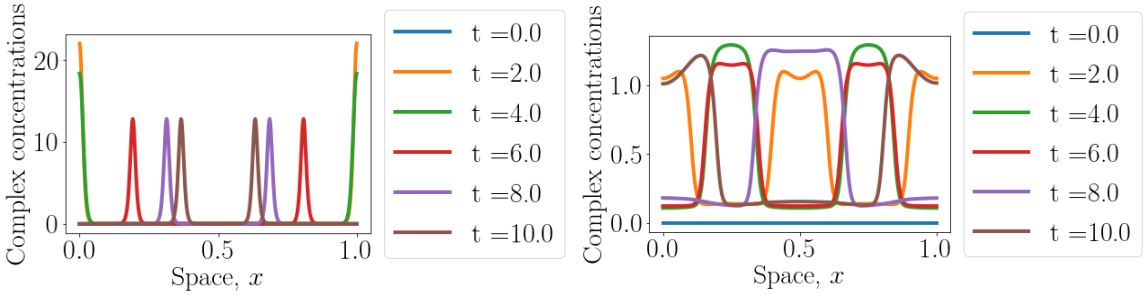

(a) Non-saturating feedback. (b) Saturating feedback.

Fig. 2.16 Numerical solution of the non-conservative model (2.63)-(2.65) with no-flux boundary conditions (2.15) and initial condition (2.45), with (a) non-saturating and (b) saturating feedback respectively, over short time scales. Solutions $c(x,t)$ are shown at the indicated times. The initial total concentration of protein A is given by (a) $a(0) = 5$ and (b) $a(0) = 2.5$, respectively. Other parameter values are $a_T^\dagger(0) = 2$, $\alpha = 1$, $k = 2$, $\beta = 0.05$, $\omega = 1$, $j^a{}_{\text{off}} = 0.1$, $j^c{}_{\text{off}} = 1.5$, $j_{\text{on}} = 1$, $D_a = 1$, $\varepsilon = 0.01$, $\phi = 0$.

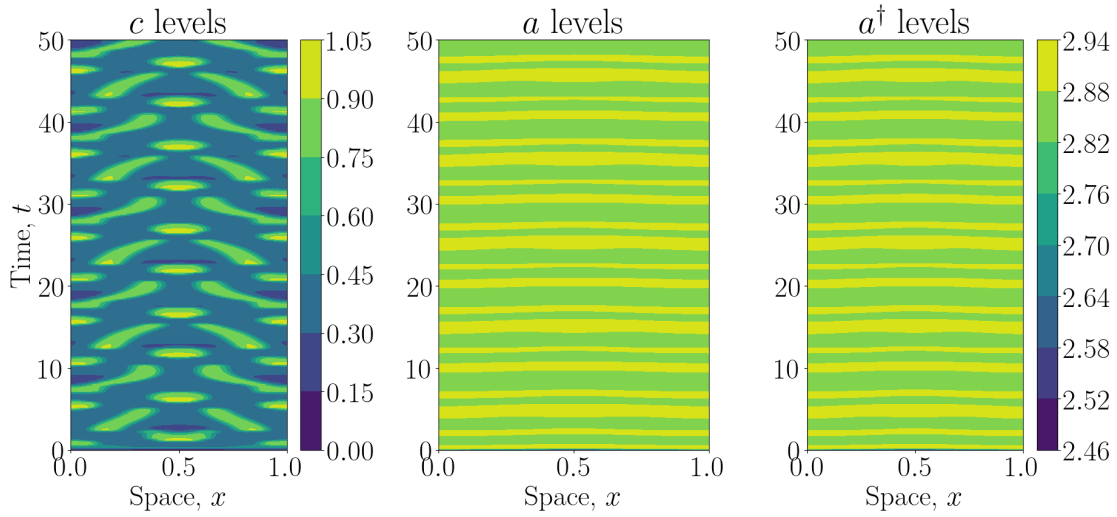

Fig. 2.17 Numerical solution of the non-conservative model (2.63)-(2.65) with no-flux boundary conditions (2.15) and initial condition (2.45), with saturating feedback, over longer time scales. Parameter values are $a(0) = 2.5$, $a^\dagger(0) = 2$, $\alpha = 0.5$, $\beta = 0.05$, $\omega = 1$, ${j^a}_{\text{off}} = 0.1$, ${j^c}_{\text{off}} = 1.5$, $j_{\text{on}} = 1$, $D_a = 1$, $\varepsilon = 0.01$, $k = 1$, $\phi = 0$.

In summary, introducing breaking mass conservation by introducing protein/complex recycling in our model can lead to the appearance of multiple, transient peaks in patterns of complex concentration. Intriguingly, it can also lead to the occurrence of spatio-temporal oscillations in complex concentrations, concomitant with temporal oscillations in the spatially uniform concentrations of unbound protein.

We conclude by noting that in the case of saturating feedback, it is possible to construct an approximate half-mesa solution using asymptotic analysis exactly as described in Section 2.2.4, since that analysis does not require the model to be mass conserved.

2.4 Discussion

In this chapter, we have identified two qualitatively distinct forms of spatial pattern that can arise in a reaction-diffusion model of local protein complex clustering. These are spikes and mesas, and occur depending on whether the nonlinear feedback that locally stabilises protein complexes is non-saturating or saturating, respectively. From a geometrical point of view, *wave-pinning* patterns or mesas are associated with the existence of a heteroclinic orbit between high and low steady states, whereas *Turing* patterns or spikes are associated with the existence of a homoclinic orbit of the system.

A key difference between these two mechanisms with biological implications is that wave-pinning systems require a sufficiently large initial perturbation to evolve to a pattern [58], whereas an arbitrarily small perturbation can suffice to drive Turing systems toward a pattern. Another key difference is that in the case of non-saturating (Turing) feedback, most early peaks rapidly coalesce into single 'spike' if there is mass conservation [59] (Fig. 2.3a), whereas for saturating (wave-pinning) feedback, mesas could exist in a meta-stable state over a long time scale, depending on parameter values [50].

Our modelling suggests that whether the system is mass conserved can play an important role in the shape, amplitude and the position of the resulting pattern. In general, our model

always requires a spatially non-uniform initial unbound protein concentration and zero initial complex concentration for patterning to occur.

Our work in this chapter is to some extent biologically motivated by E-cadherin cluster formation in developing epithelial tissues [4, 60, 61]. E-cadherin clusters have been shown to be more stable and less mobile than unbound proteins [4]. This is why we assumed that complexes can diffuse but at a very low rate in comparison with unbound proteins.

Our modelling shares similarities with other models of mass-conserved reaction-diffusion systems [25, 49, 59]. However, those models take into account only two chemical species, and suggest that the corresponding kinetic reaction (a quadratic non-saturating feedback or a saturating feedback with Hill coefficient 2) yields three SUSS solutions. In contrast, our modelling considers three species and yields four SUSS solutions. There is scope for further model comparison under different assumptions on the form of feedbacks. A further means of of extending our work would be to apply local equilibria theory to characterise the dynamics from a graphical perspective [62, 54]. Local equilibria theory is an approach that dissects space into local compartments and allows spatial-temporal characterisation of dynamics on the basis of the phase space of local reaction kinetics [54].

It is instructive to compare our modelling to an alternative model, tailored to E-cadherin cluster formation, proposed by Quang et al. [4]. In that model, *trans*-membrane binding is assumed to be irreversible, whereas we assume that unbinding may occur. In addition, that model explicitly includes the presence of higher-order complexes, formed of multiple unbound proteins in either cell; a potential avenue for future work would be to include such additional 'species' in our modelling framework. Another natural avenue for future work would be to incorporate multiple distinct protein species and allow for heterodimers; this would be the first step toward modelling puncta in planar polarity pathway complexes [47], for example.

Chapter 3

Feedback requirements for cell-to-tissue scale planar polarity

3.1 Introduction

As described in Chapter 1, planar polarity involves the coordinated orientation of cells within a tissue. In this process, each cell generates its own polarity due to the asymmetric localisation of certain proteins to different ends of the cell, where they form oriented transmembrane protein complexes with adjacent cells. It is thought that this asymmetric localisation is established through an initial 'bias' that is amplified via some form of *feedback interaction* [63]. Such feedback has been suggested to involve mutual stabilisation of 'like' complexes of the same orientation and/or destabilisation of 'unlike' complexes of opposite orientations (Fig. 3.1) and may amplify small biases in protein localisation induced by global cues [19].

The likely presence of nonlinear feedback mechanisms has precluded the intuitive understanding of cell-scale planar polarisation through experimentation alone. Mathematical modelling can help us to disentangle this complexity by exploring whether the proposed mechanisms account for observed behaviours under normal and perturbed conditions [17, 34, 64].

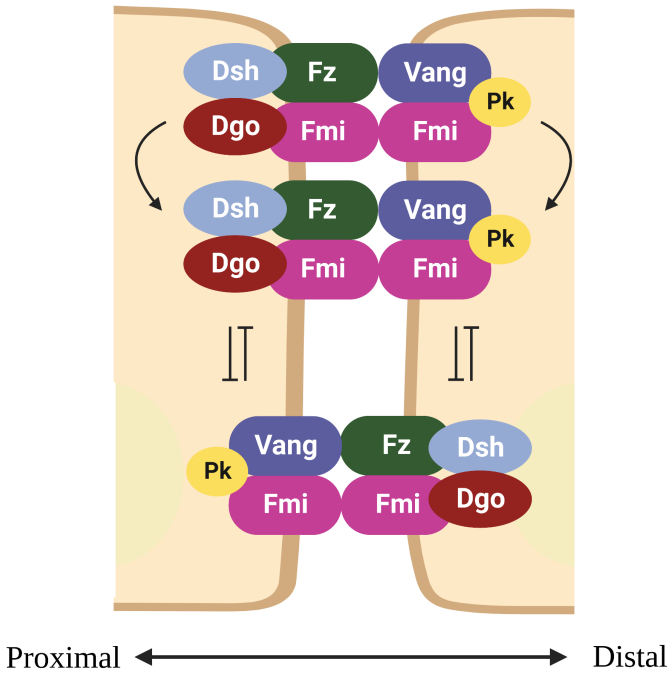

Fig. 3.1 Diagram of the intercellular complexes formed by core pathway proteins at a junction between two neighbouring cells, highlighting possible feedback interactions. These interactions may involve mutual stabilisation of 'like' complexes of the same orientation (pointed arrows) and/or destabilisation of 'unlike' complexes of opposite orientations (flat-headed arrows). This schematic is created with BioRender.

A notable mathematical model of planar polarisation was proposed by Amonlirdviman et al. [38], who used a system of reaction-diffusion partial differential equations to simulate the evolution of protein localisation over time in a two-dimensional cell grid relating to a part of the fly wing. In their model, a Fz feedback loop is represented by reactions between Dsh, Fz, Vang and Pk to form protein complexes, with a feedback inhibition term and a global directional cue that is provided for each cell as an asymmetric input. This model explains phenotypes in several Fz mutants, and predicts that non-autonomy occurs only in mutants where Fz in one cell does not recruit Vang to neighbouring cells. However, the model does not allow the authors to distinguish how the directional cue might influence the Fz feedback loop.

Another notable model, comprising a stochastic reaction-diffusion system, was proposed by Le Garrec et al. [65]. In this model, a Fz gradient arises due to the graded formation of Fmi-based asymmetric intercellular complexes. While the model explores whether Fmi dimerisation is required for forming a Fz homodimer, it places strict limitations on the strength, direction and duration of the assumed Fz activity gradient.

The involvement of the transmembrane core pathway proteins Fz, Vang, and Fmi in cell-cell signalling is experimentally well-established [66]. However, it remains unclear whether that signalling is transmitted between cells in a *monodirectional* (only by Fz on Vang) or *bidirectional* form (also by Vang on Fz). In double clones lacking both Vang and Fz, bidirectional signalling would – if the bidirectional signals are of equal strength – imply that neighbouring cells have normal polarity, as they are not affected by mutant cells lacking both Vang and Fz [66]. Monodirectional signalling would imply otherwise, since under this hypothesis, Vang acts as a Fz receptor in which cells can sense the Fz levels of their neighbouring cells [67]. Recent experiments have supported the existence of bidirectional signalling mechanisms, though this is not yet definitive [66, 68].

In a recent interdisciplinary study, Fisher et al. [63] develop a mathematical model of the core planar polarity pathway in the fly wing, abstracted to a one-dimensional line of cells, and simulated wild-type and mutant clone behaviours under a variety of hypothesised feedback mechanisms. The authors compare their simulation results qualitatively with experimental data on polarisation in (i) normal tissue, (ii) cells neighbouring single Fz^-, $Vang^-$ or Fmi^- clones, and (iii) cells neighbouring $Vang^-Fz^-$ clones. Rejecting model assumptions for which simulations cannot recapitulate these cases, particular (iii) where domineering non-autonomy was experimentally observed to be inhibited, the authors deduce that some form of bidirectional signalling must be present, mediated either indirectly via bidirectional feedbacks or directly via differential protein binding affinities. Fisher et al. [63] note some differences when comparing simulations of mutant clone phenotypes under stabilising and destabilising

feedbacks. First, in the case of balanced stabilising feedback between 'like' complexes, cells neighbouring Fmi^{-} clones were found to propagate a 'period two' pattern, whereby every other cell exhibits the opposite polarity. Second, due to the reduced sorting of complexes, the system tends to polarise more slowly in the presence of stabilising feedback than with destabilising feedback of equivalent strength.

The above studies involve detailed models of the core pathway and therefore do not lend themselves easily to mathematical analysis. In an alternate approach, Schamberg et al. [69] propose a simple feedback/diffusion model that abstracts the activity of planar polarity to two variables per cell. For all parameter sets considered, the authors find that sufficiently strong intercellular feedback and sufficiently weak intracellular diffusion suffice to achieve planar polarisation [69]. However, it is difficult to link the 'generic activity' state variables in this model directly to physical quantities such as protein concentrations and (un)binding rates.

3.1.1 Aim of work

While modelling has shed some light on planar polarisation, the circumstances under which feedback interactions can sufficiently amplify initial biases to establish planar polarity remain unclear. In particular, it is challenging to extract such conditions through mathematical analysis of biochemically detailed models such as that of Fisher et al. [63]. To address this, in this chapter we consider a minimal biochemically-motivated model to gain a qualitative understanding of the requirements for (de)stabilising feedback to establish planar polarisation.

Our approach is based on the reversible binding of two protein species to form transmembrane complexes at cell-cell junctions and intracellular protein diffusion. For simplicity, we consider a one-dimensional line of cells, each comprising two compartments corresponding to its left and right edges. We explore a variety of different hypothesised feedback mechanisms, extending the work of [63] to consider feedback on rates of intracellular protein transport and membrane trafficking in addition to (un)binding. In each case, we combine

steady state, linear stability and bifurcation analysis with numerical simulations to explore the conditions under which feedback interactions suffice for cell-scale polarisation and for tissue-scale polarisation. We also consider the polarisation of cells neighbouring mutant clones in which the total concentration and/or production rate of each protein is perturbed. For ease of navigation, we summarise the various cases considered in Tab. 3.1.

Feedback target	Feedback type	Figures	Single clone prediction	Double clone prediction
Binding	Destabilising	3.3, 3.4a, 3.5a, 3.7, 3.9a	Non-autonomy	No non-autonomy
	Stabilising	3.4b, 3.5b, 3.8, 3.9b	Non-autonomy	Period two patterns
Trafficking	Destabilising	3.10, 3.11a, 3.12a, 3.13, 3.15a	Non-autonomy	No non-autonomy
	Stabilising	3.11b, 3.12b, 3.14, 3.15b	Non-autonomy	Period two patterns
Degradation	Destabilising	3.16, 3.17, 3.18, 3.19, 3.20	No non-autonomy	No non-autonomy

Table 3.1 Summary of planar polarity models considered in this chapter.

The remainder of this chapter is structured as follows. In Section 3.2, we consider a 'binding feedback' model, where (de)stabilising feedback interactions modulate the rate of protein (un)binding. In Section 3.3, we consider an alternative 'trafficking feedback' model, where feedback interactions instead modulate the rate of intracellular protein transport. In Section 3.4, we consider a 'degradation feedback' model, where – in contrast to the first two models – the total concentration of each protein in each cell is not conserved, but instead we include protein production and allow feedback interactions to modulate the rate at which protein complexes are recycled from the cell membrane (i.e. degraded). We conclude in Section 3.5 with a discussion of our theoretical results and their implications for advancing our understanding of the role of feedback mechanisms in planar polarisation.

3.2 Binding feedback model

We propose a simplified planar polarity system operating in a one-dimensional ring of N cells (Fig. 3.2). In all of the models considered in this chapter two proteins, A and B are allowed to bind and unbind across neighbouring cells to form an intercellular complex C according to the reversible reactions

$$A_i^L + B_{i-1}^R \rightleftharpoons C_i^L, \tag{3.1}$$

$$A_{i-1}^R + B_i^L \rightleftharpoons C_{i-1}^R, \tag{3.2}$$

and diffuse between sides of each cell according to the 'reactions'

$$A_i^L \rightleftharpoons A_i^R, \tag{3.3}$$

$$B_i^L \rightleftharpoons B_i^R, \tag{3.4}$$

for each cell $i \in \{0,\ldots,N-1\}$. In equations (3.1)–(3.4), superscripts L and R denote the left and right edge of a cell, while subscript i denotes the ith cell, modulo N (Fig. 3.2). We assume that reactions (3.1)–(3.2) each proceed with a forward rate coefficient k and a backward rate coefficient v. We also assume that proteins A and B diffuse between cell compartments with diffusion coefficients D_A and D_B, respectively. In this section, we assume that D_A and D_B are constant, while v and k may depend on the local complex concentration.

3.2.1 Governing equations

Let $A_i^j(T)$, $B_i^j(T)$, and $C_i^j(T)$ denote the concentrations of molecules A, B and C in cell i, compartment $j \in \{L,R\}$, at time T. Using the Law of Mass Action, reactions (3.1)–(3.4)

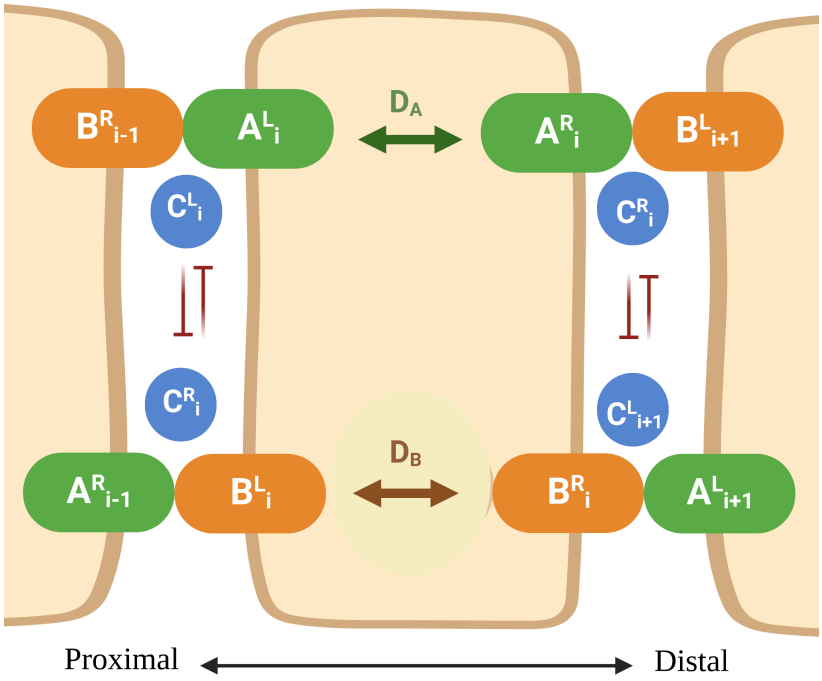

Fig. 3.2 Schematic of the biochemical reactions summarised in equations (3.1)–(3.4). This schematic is created with BioRender.

may be converted into the ordinary differential equation (ODE) system

$$\frac{dA_i^L}{dT} = -kA_i^L B_{i-1}^R + vC_i^L + D_A(A_i^R - A_i^L), \tag{3.5}$$

$$\frac{dA_i^R}{dT} = -kA_i^R B_{i+1}^L + vC_i^R + D_A(A_i^L - A_i^R), \tag{3.6}$$

$$\frac{dB_i^L}{dT} = -kA_{i-1}^R B_i^L + vC_{i-1}^R + D_B(B_i^R - B_i^L), \tag{3.7}$$

$$\frac{dB_i^R}{dT} = -kA_{i+1}^L B_i^R + vC_{i+1}^L + D_B(B_i^L - B_i^R), \tag{3.8}$$

$$\frac{dC_i^L}{dT} = kA_i^L B_{i-1}^R - vC_i^L, \tag{3.9}$$

$$\frac{dC_i^R}{dT} = kA_i^R B_{i+1}^L - vC_i^R. \tag{3.10}$$

As can be verified by taking suitable linear combinations of equations (3.5)–(3.10), the total (bound and unbound) concentrations of A and B are conserved in each cell, that is

$$A_i^L + A_i^R + C_i^L + C_i^R = A_{\text{tot}}, \tag{3.11}$$

$$B_i^L + B_i^R + C_{i-1}^R + C_{i+1}^L = B_{\text{tot}}, \tag{3.12}$$

where the constants A_{tot} and B_{tot} are determined by the initial conditions.

We non-dimensionalise this model as follows. We write $k = k_0\mathscr{K}$ and $v = v_0\mathscr{V}$, where k_0 and v_0 denote baseline values for the forward and backward rate coefficients, respectively, while $\mathscr{K}$ and $\mathscr{V}$ may be either equal to 1 (corresponding to no feedback in that reaction) or given by some nonlinear function of the local complex concentration (corresponding to feedback in that reaction). We write $T = t/k_0A_{\text{tot}}$ and $A_i^j = A_{\text{tot}}a_i^j$, $B_i^j = B_{\text{tot}}b_i^j$, $C_i^j = A_{\text{tot}}c_i^j$ for $j \in \{L,R\}$, where a_i^j, b_i^j, c_i^j and t denote dimensionless variables. Finally, we define dimensionless lumped parameters

$$\nu = \frac{v_0}{k_0A_{\text{tot}}}, \qquad \gamma = \frac{B_{\text{tot}}}{A_{\text{tot}}}, \qquad \delta = \frac{D_A}{k_0A_{\text{tot}}}, \qquad \sigma = \frac{D_B}{D_A}. \tag{3.13}$$

Substituting into (3.5)–(3.10), and using dots to denote differentiation with respect to t, we obtain the non-dimensionalised system

$$\dot{a}_i^L = -\gamma\mathscr{K}(c_i^L)a_i^Lb_{i-1}^R + \nu\mathscr{V}(c_{i-1}^R)c_i^L + \delta(a_i^R - a_i^L), \tag{3.14}$$

$$\dot{a}_i^R = -\gamma\mathscr{K}(c_i^R)a_i^Rb_{i+1}^L + \nu\mathscr{V}(c_{i+1}^L)c_i^R + \delta(a_i^L - a_i^R), \tag{3.15}$$

$$\dot{b}_i^L = -\mathscr{K}(c_{i-1}^R)a_{i-1}^Rb_i^L + \frac{\nu}{\gamma}\mathscr{V}(c_i^L)c_{i-1}^R + \sigma\delta(b_i^R - b_i^L), \tag{3.16}$$

$$\dot{b}_i^R = -\mathscr{K}(c_{i+1}^L)a_{i+1}^Lb_i^R + \frac{\nu}{\gamma}\mathscr{V}(c_i^R)c_{i+1}^L + \sigma\delta(b_i^L - b_i^R), \tag{3.17}$$

$$\dot{c}_i^L = \gamma\mathscr{K}(c_i^L)a_i^Lb_{i-1}^R - \nu\mathscr{V}(c_{i-1}^R)c_i^L, \tag{3.18}$$

$$\dot{c}_i^R = \gamma\mathscr{K}(c_i^R)a_i^Rb_{i+1}^L - \nu\mathscr{V}(c_{i+1}^L)c_i^R, \tag{3.19}$$

with non-dimensionalised conservation laws

$$a_i^L + a_i^R + c_i^L + c_i^R = 1, \tag{3.20}$$

$$\gamma b_i^L + \gamma b_i^R + c_{i-1}^R + c_{i+1}^L = \gamma. \tag{3.21}$$

The initial and boundary conditions are defined in Section 3.2.3.

3.2.2 Steady state and linear stability analysis

We next consider the existence and linear stability of any steady state(s). For simplicity, we consider only *homogeneous* steady states and perturbations, where

$$a_i^L(t) \equiv a^L(t), \qquad b_i^L(t) \equiv b^L(t), \qquad c_i^L(t) \equiv c^L(t), \tag{3.22}$$

$$a_i^R(t) \equiv a^R(t), \qquad b_i^R(t) \equiv b^R(t), \qquad c_i^R(t) \equiv c^R(t), \tag{3.23}$$

for all i. However, we allow spatially *non-uniform* steady states, for which $a^L(t) \not\equiv a^R(t)$, $b^L(t) \not\equiv b^R(t)$ and $c^L(t) \not\equiv c^R(t)$. Equations (3.14)–(3.19) therefore simplify to

$$\dot{a}^L = -\gamma \mathscr{K}(c^L) a^L b^R + \nu \mathscr{V}(c^R) c^L + \delta(a^R - a^L), \tag{3.24}$$

$$\dot{a}^R = -\gamma \mathscr{K}(c^R) a^R b^L + \nu \mathscr{V}(c^L) c^R + \delta(a^L - a^R), \tag{3.25}$$

$$\dot{b}^L = -\mathscr{K}(c^R) a^R b^L + \frac{\nu}{\gamma} \mathscr{V}(c^L) c^R + \sigma\delta(b^R - b^L), \tag{3.26}$$

$$\dot{b}^R = -\mathscr{K}(c^L) a^L b^R + \frac{\nu}{\gamma} \mathscr{V}(c^R) c^L + \sigma\delta(b^L - b^R), \tag{3.27}$$

$$\dot{c}^L = \gamma \mathscr{K}(c^L) a^L b^R - \nu \mathscr{V}(c^R) c^L, \tag{3.28}$$

$$\dot{c}^R = \gamma \mathscr{K}(c^R) a^R b^L - \nu \mathscr{V}(c^L) c^R, \tag{3.29}$$

with conservation laws

$$a^L + a^R + c^L + c^R = 1, \tag{3.30}$$

$$\gamma b^L + \gamma b^R + c^L + c^R = \gamma. \tag{3.31}$$

Existence and uniqueness of positive SUSS

We first seek positive spatially uniform steady state (SUSS) solution(s) of the homogeneous system (3.24)–(3.29) of the form $a^L = a^R = a$, $b^L = b^R = b$, and $c^L = c^R = c$. Substituting into equations (3.24), (3.30) and (3.31), we find that a, b and c must satisfy

$$-\gamma \mathscr{K}(c)ab + \nu \mathscr{V}(c)c = 0, \tag{3.32}$$

$$2a + 2c = 1, \tag{3.33}$$

$$2\gamma b + 2c = \gamma. \tag{3.34}$$

We next consider the existence and uniqueness of the SUSS satisfying equations (3.32)–(3.34). In the absence of feedback, the forward and backward rate coefficients do not depend on complex concentrations, hence $\mathscr{K} = \mathscr{V} = 1$. In this case, eliminating b and c from equations (3.32)–(3.34), we find that a must satisfy

$$2a^2 + (\gamma + 2\nu - 1)a - \nu = 0. \tag{3.35}$$

By Descartes' rule of signs [70], regardless of the sign of $\gamma + 2\nu - 1$, there is a unique positive root of (3.35) given by

$$a = \frac{1}{4}\left(1 - \gamma - 2\nu + \sqrt{(\gamma + 2\nu - 1)^2 + 8\nu}\right). \tag{3.36}$$

The corresponding values of b and c are also positive and are given by

$$b = \frac{1}{4\gamma}\left(-1+\gamma-2\nu+\sqrt{(\gamma+2\nu-1)^2+8\nu}\right), \tag{3.37}$$

$$c = \frac{1}{4}\left(1+\gamma+2\nu-\sqrt{(\gamma+2\nu-1)^2+8\nu}\right). \tag{3.38}$$

Thus, in the absence of feedback, the system has a unique positive SUSS.

In the presence of destabilising feedback, we assume that the higher the concentration of c in one orientation between two neighbouring cells is, the faster the reverse reaction proceeds in the opposite orientation. This corresponds to $\mathscr{K} = 1$ and $\mathscr{V}$ being a monotonic increasing function satisfying $\mathscr{V}(0) = 1$. In this case, any SUSS must satisfy

$$4\nu c\mathscr{V}(c) = (1-2c)(\gamma-2c). \tag{3.39}$$

Since the left-hand side of (3.39) is monotonic increasing from 0, and the right-hand side is monotonic decreasing from γ to 0 for $c < \min\{1/2, \gamma/2\}$, there must be at least one positive root, and hence at least one positive SUSS.

In the presence of stabilising feedback, we assume that the higher the concentration of c in one orientation between two neighbouring cells is, the slower the reverse reaction proceeds in the opposite orientation. This corresponds to $\mathscr{V} = 1$ and $\mathscr{K}$ being a monotonic increasing function such that $\mathscr{K}(0) = 1$. In this case, any SUSS must satisfy the nonlinear equation

$$4\nu c = (1-2c)(\gamma-2c)\mathscr{K}(c). \tag{3.40}$$

It is less straightforward to show that in general there must be a positive root of (3.40), but the numerical results presented in Section 3.2.3 support this claim.

By inspection of (3.39) and (3.40), it is clear that we cannot guarantee uniqueness of the positive SUSS in the presence of feedback. In the following, when referring to a positive

SUSS, we implicitly assume this to be that branch that tends to the unique stable positive SUSS in the 'limit' of no feedback.

Linear stability of positive SUSS

We next examine the linear stability of the positive SUSS (a,b,c) to homogeneous perturbations by letting

$$a^j = a + \tilde{a}^j, \qquad b^j = b + \tilde{b}^j, \qquad c^j = c + \tilde{c}^j \tag{3.41}$$

for $j \in \{L,R\}$. Substituting into equations (3.24)–(3.29) and dropping higher-order terms, we obtain the linearised system

$$\dot{\tilde{a}}^L = -(\gamma\mathscr{K} b + \delta)\tilde{a}^L + \delta\tilde{a}^R - \gamma\mathscr{K} a\tilde{b}^R + (\nu\mathscr{V} - \gamma\mathscr{K}' ab)\tilde{c}^L + \nu\mathscr{V}' c\tilde{c}^R, \tag{3.42}$$

$$\dot{\tilde{a}}^R = -(\gamma\mathscr{K} b + \delta)\tilde{a}^R + \delta\tilde{a}^L - \gamma\mathscr{K} a\tilde{b}^L + (\nu\mathscr{V} - \gamma\mathscr{K}' ab)\tilde{c}^R + \nu\mathscr{V}' c\tilde{c}^L, \tag{3.43}$$

$$\dot{\tilde{b}}^L = -\mathscr{K} b\tilde{a}^R - (\mathscr{K} a + \sigma\delta)\tilde{b}^L + \sigma\delta\tilde{b}^R + \frac{\nu}{\gamma}\mathscr{V}' c\tilde{c}^L + \frac{1}{\gamma}(\nu\mathscr{V} - \gamma\mathscr{K}' ab)\tilde{c}^R, \tag{3.44}$$

$$\dot{\tilde{b}}^R = -\mathscr{K} b\tilde{a}^L - (\mathscr{K} a + \sigma\delta)\tilde{b}^R + \sigma\delta\tilde{b}^L + \frac{\nu}{\gamma}\mathscr{V}' c\tilde{c}^R + \frac{1}{\gamma}(\nu\mathscr{V} - \gamma\mathscr{K}' ab)\tilde{c}^L, \tag{3.45}$$

$$\dot{\tilde{c}}^L = \gamma\mathscr{K} b\tilde{a}^L + \gamma\mathscr{K} a\tilde{b}^R - (\nu\mathscr{V} - \gamma\mathscr{K}' ab)\tilde{c}^L - \nu\mathscr{V}' c\tilde{c}^R, \tag{3.46}$$

$$\dot{\tilde{c}}^R = \gamma\mathscr{K} b\tilde{a}^R + \gamma\mathscr{K} a\tilde{b}^L - (\nu\mathscr{V} - \gamma\mathscr{K}' ab)\tilde{c}^R - \nu\mathscr{V}' c\tilde{c}^L, \tag{3.47}$$

where $\mathscr{K} \equiv \mathscr{K}(c)$ and so on. Introducing the change of variables

$$s_a = \tilde{a}^L + \tilde{a}^R, \qquad s_b = \tilde{b}^L + \tilde{b}^R, \qquad s_c = \tilde{c}^L + \tilde{c}^R, \tag{3.48}$$

$$d_a = \tilde{a}^L - \tilde{a}^R, \qquad d_b = \tilde{b}^L - \tilde{b}^R, \qquad d_c = \tilde{c}^L - \tilde{c}^R, \tag{3.49}$$

and writing $\mathbf{s} = (s_a, s_b, s_c)$, $\mathbf{d} = (s_a, s_b, s_c)$, we obtain the block diagonal system

$$\begin{pmatrix} \dot{\mathbf{s}} \\ \dot{\mathbf{d}} \end{pmatrix} = \begin{pmatrix} M_s & 0 \\ 0 & M_d \end{pmatrix}, \tag{3.50}$$

where

$$M_s = \begin{pmatrix} -\gamma\mathscr{K}b & -\gamma\mathscr{K}a & \nu(\mathscr{V}+\mathscr{V}'c) - \gamma\mathscr{K}'ab \\ -\mathscr{K}b & -\mathscr{K}a & \frac{1}{\gamma}[\nu(\mathscr{V}+\mathscr{V}'c) - \gamma\mathscr{K}'ab] \\ \gamma\mathscr{K}b & \gamma\mathscr{K}a & -[\nu(\mathscr{V}+\mathscr{V}'c) - \gamma\mathscr{K}'ab] \end{pmatrix}, \tag{3.51}$$

$$M_d = \begin{pmatrix} -(\gamma\mathscr{K}b + 2\delta) & \gamma\mathscr{K}a & \psi+\phi-\nu \\ \mathscr{K}b & -(\mathscr{K}a + 2\sigma\delta) & -\frac{1}{\gamma}[\psi+\phi-\nu] \\ \gamma\mathscr{K}b & -\gamma\mathscr{K}a & -[\psi+\phi-\nu] \end{pmatrix}, \tag{3.52}$$

and $\phi \equiv \nu - \gamma\mathscr{K}'ab$, $\psi \equiv \nu(\mathscr{V} - \mathscr{V}'c)$.

Since (3.50) has block diagonal form, its characteristic polynomial $F(\lambda)$ is given by the product of those of M_s and M_d. These, in turn, are given by

$$F_s(\lambda) = -\lambda^2[\lambda + \mathscr{K}a + \gamma\mathscr{K}b + \nu(\mathscr{V}+\mathscr{V}'c) + \phi - \nu], \tag{3.53}$$

$$F_d(\lambda) = -\lambda^3 - \alpha_2\lambda^2 - \alpha_1\lambda - \alpha_0, \tag{3.54}$$

where

$$\alpha_0 = 4\sigma\delta^2(\psi+\phi-\nu), \tag{3.55}$$

$$\alpha_1 = 2\delta[\mathscr{K}a + \sigma\gamma\mathscr{K}b + 2\sigma\delta + (\psi+\phi-\nu)(1+\sigma)], \tag{3.56}$$

$$\alpha_2 = \mathscr{K}a + \gamma\mathscr{K}b + \psi + \phi - \nu + 2(1+\sigma)\delta, \tag{3.57}$$

In the absence of feedback ($\mathscr{K} = \mathscr{V} = 1$), the roots of (3.53) are given by $\lambda_{1,2} = 0$ and $\lambda_3 = -a - \gamma b - \nu < 0$. Considering $F_d(\lambda)$, since the SUSS and all parameters are positive,

so are α_0, α_1, α_2, hence by Descartes' rule of signs (3.54) has no positive roots. Therefore, the SUSS is linearly stable to spatially homogeneous perturbations.

In the case of destabilising feedback ($\mathscr{K} = 1$, $\mathscr{V}$ a monotonic increasing function), the roots of (3.53) are $\lambda_{1,2} = 0$ and $\lambda_3 = -a - \gamma b - \nu(\mathscr{V} + \mathscr{V}'c) < 0$. The number of positive roots of equation (3.54) can again be deduced using Descartes' rule of signs, and depends on ψ: (i) if $\psi \geq 0$, there are no positive roots, hence the SUSS is linearly stable; (ii) if $\psi < 0$, there is at least one positive root, hence the SUSS is linearly unstable.

The case of stabilising feedback ($\mathscr{V} = 1$, $\mathscr{K}$ a monotonic increasing function) is similar. In this case, the roots of (3.53) are $\lambda_{1,2} = 0$ and $\lambda_3 = -a\mathscr{K} - \gamma b\mathscr{K} - (\nu - \gamma\mathscr{K}'ab) < 0$, while the number of positive roots of equation (3.54) depends on the sign and magnitude of ϕ: (i) if $\phi \geq 0$, there are no positive roots of (3.54), hence the SUSS is linearly stable; (ii) if $\phi < 0$, there is at least one positive root, hence the SUSS is linearly unstable.

In summary, we have obtained inequalities that must be satisfied for the SUSS to become linearly unstable to spatially homogeneous perturbations in our binding feedback model. These inequalities ($\psi < 0$ for destabilising feedback, $\phi < 0$ for stabilising feedback) may, if a particular feedback function were chosen, be related to the minimum *strength* of feedback required for the SUSS to lose stability to spatially homogeneous perturbations. Of course, the SUSS might go unstable to spatially *inhomogeneous* perturbations at even lower feedback strengths, but a more general stability analysis quickly becomes intractable.

3.2.3 Numerical simulations

In this section we verify our analytical results numerically. We also examine the behaviour of the system in the case of verifying key parameters (feedback strength and sharpness; total protein concentrations). Finally, we simulate a variety of mutant clones and compare our findings to experimentally observed phenotypes such as domineering non-autonomy.

We solve the non-dimensionalised model (3.14)-(3.19) numerically using a variable-step, variable-order method (implemented using the function `odeint` from `scipy.integrate` in Python) for a ring of $N = 30$ cells of equal size (Fig. 3.2). We impose periodic boundary conditions at the left edge of cell 0 and the right edge of cell $N-1$. Starting from specified initial conditions (see below), the ODE system is solved numerically and allowed to evolve to a steady state. Simulations are run to ensure that a steady state is achieved by plotting solutions over time to ensure no further change in levels.

For simplicity, we assume that proteins a and b have the same diffusion coefficient ($\sigma = 1$), and assume the same total concentration in each cell ($\gamma = 1$), unless stated otherwise. We fix $\delta = 0.01$ and $\nu = 0.1$. We assume that initially no complex is present, with equal concentrations of b on the left and right edges of each cell, and a slightly higher concentration of a on the right rather than on the left edges [63]:

$$a^L(0) = \frac{1}{2} - \varepsilon, \quad a^R(0) = \frac{1}{2} + \varepsilon, \quad b^L(0) = b^R(0) = \frac{1}{2}, \quad c^L(0) = c^R(0) = 0, \tag{3.58}$$

where $\varepsilon = 0.01$. Biologically, we may relate this initial bias to some directional cue [71]. It is important to note that we are not explicitly modelling the *source* of such a cue; instead, we are simply assuming that there is some upstream cue that leads to the initial conditions to be asymmetric. We return to this point in the discussion (Section 3.5).

For our numerical simulations, we must choose specific functional forms for our feedback functions $\mathscr{V}$ and $\mathscr{K}$. We choose sigmoidal functions

$$\mathscr{V}(c) = 1 + \frac{(\eta - 1)c^n}{\kappa^n + c^n}, \tag{3.59}$$

$$\mathscr{K}(c) = 1 + \frac{(\mu - 1)c^m}{\rho^m + c^m}, \tag{3.60}$$

where η and μ denote the maximal relative level of destabilising and stabilising feedback in the binding rate, κ and ρ denote the concentrations at which the corresponding feedback is half-maximal, n and m represent the steepness of each type of feedback, respectively.

Polarisation in the presence of binding feedback

We first illustrate how the presence of binding feedback can result in polarisation in this model. Fig. 3.3 shows numerical results in the case of destabilising feedback for an example parameter set. Qualitatively similar results are obtained in the case of stabilising feedback (results not shown). We find that for our chosen parameter values, the system exhibits planar polarisation. Note that as a result of diffusion, the complex concentrations $c^L(t)$ and $c^R(t)$ in each cell tend to different steady-state values, while the unbound protein concentrations $a^L(t)$ and $a^R(t)$ tend towards the same value, as do $b^L(t)$ and $b^R(t)$ (Fig. 3.3a).

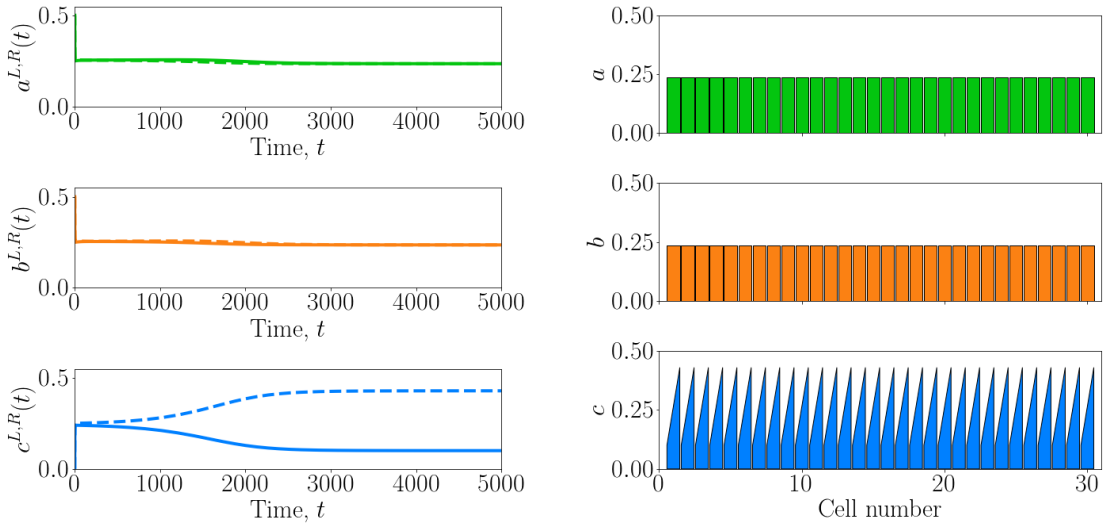

(a) (b)

Fig. 3.3 Numerical solution of the binding feedback model (3.14)–(3.19) with initial condition (3.58) in the presence of destabilising feedback (3.59). Non-dimensional parameter values are $\nu = 0.1$, $\gamma = 1$, $\delta = 0.01$, $\sigma = 1$, $\varepsilon = 0.01$, $\eta = 30$, $\kappa = 1$, $n = 2$. (a) Solid lines: L; dashed lines: R. Numerical solution shown at $t = 10^5$.

The tissue-scale polarised steady state is shown in Fig. 3.3b. Here, each cell has a lower complex concentration on its left side than its right side; this is due to our choice of bias in the initial condition (3.58). Note that in the absence of an initial bias, the system should theoretically evolve over time to the positive SUSS; in practice however, roundoff errors can lead the numerical simulation to evolve to a polarised steady state even in this case (results not shown).

Polarisation dependence on binding feedback strength and sharpness

Next, we explore whether a certain strength, or sharpness, of feedback is required for polarisation. Since we are interested in how the strength of feedback affects the linear stability of the SUSS, we treat the feedback strength parameters η and μ, or feedback sharpness parameters n and m, in (3.59) and (3.60) as bifurcation parameters and consider all remaining parameters as 'fixed'. For simplicity, we consider a single cell with 'periodic' boundary conditions rather than simulating the full tissue.

The upper graphs of Fig. 3.4 show the steady-state values of c^L and c^R (technically, their values reached at $t = 10^5$) for feedback strengths η and μ ranging from 1 to 40. We observe a pitchfork bifurcation, with the SUSS losing stability at critical values of $\eta \approx 19$ (Fig. 3.4a) and $\mu \approx 12$ (Fig. 3.4b), respectively. The lower graphs of Fig. 3.4 show that above these critical values, the terms ψ and ϕ defined in our linear stability analysis above become negative. This confirms our theoretical finding that the SUSS is unstable with destabilising feedback if and only if $\psi < 0$, and with stabilising feedback if and only if $\phi < 0$. In conclusion, sufficiently strong feedback is required to drive the system away from the SUSS and into a stable polarised state.

We next examine how the feedback sharpness affects the system's polarity for a fixed feedback strength. Fig. 3.5 shows that for both feedback types, there is an intermediate sharpness range for which the system exhibits polarity, before the bifurcation moves to a non-

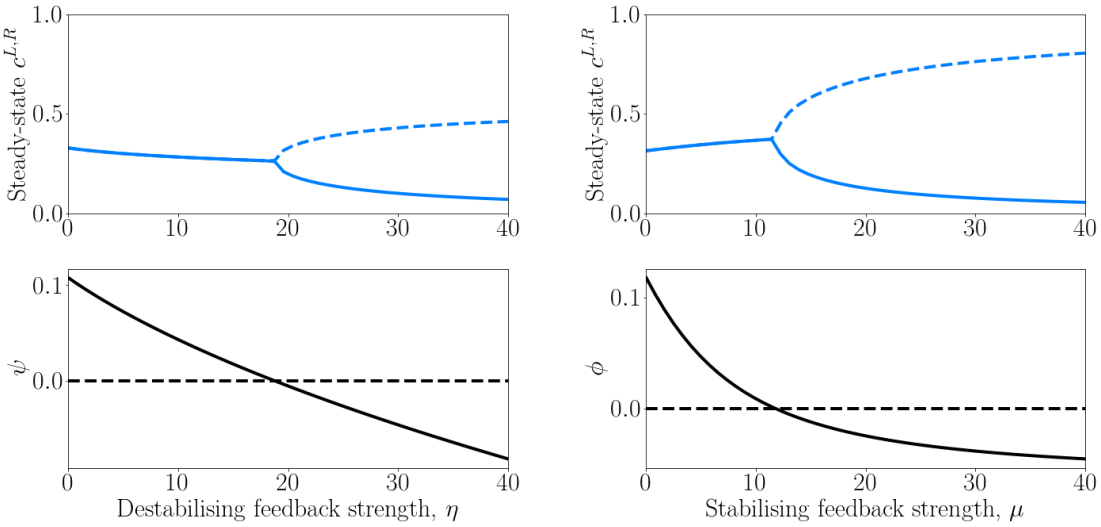

(a) (b)

Fig. 3.4 Bifurcation analysis of the binding feedback model (3.14)–(3.19) with respect to feedback strength. Non-dimensional parameter values are $\nu = 0.1$, $\gamma = 1$, $\delta = 0.01$, $\sigma = 1$, $\varepsilon = 0.01$, $\kappa = 1$, $n = 2$, $\rho = 1$, $m = 2$. Solid lines: L; dashed lines: R (upper panels).

polarised state. This finite range also matches the amplitude of the terms ψ and ϕ (see lower panels of Fig. 3.5). Loosely speaking, we may interpret the feedback sharpness biologically to the degree of *cooperativity* associated with the feedback interaction. In simpler enzymatic reactions such as the binding of oxygen to haemoglobin, this can be related to the number of molecules involved in a reaction. For more complex systems, however, care should be taken with this interpretation [72]. Nevertheless, it is somewhat counter-intuitive that feedback must be sufficiently sharp, but not too sharp, for polarisation to occur in this model.

Polarisation dependence on relative total protein concentrations

We next explore the effect of varying γ, the ratio of B_{tot} to A_{tot}, on polarisation. Here, we consider the strength and sharpness of each form of feedback to be 'fixed'. As shown in Fig. 3.6, in both feedback cases we observe a bifurcation, with a critical value of γ above which polarisation occurs. Comparing Fig. 3.6a with Fig. 3.6b (respectively Fig. 3.6c with Fig. 3.6d), we find that for a stronger feedback, a lower value of γ suffices for polarisation to

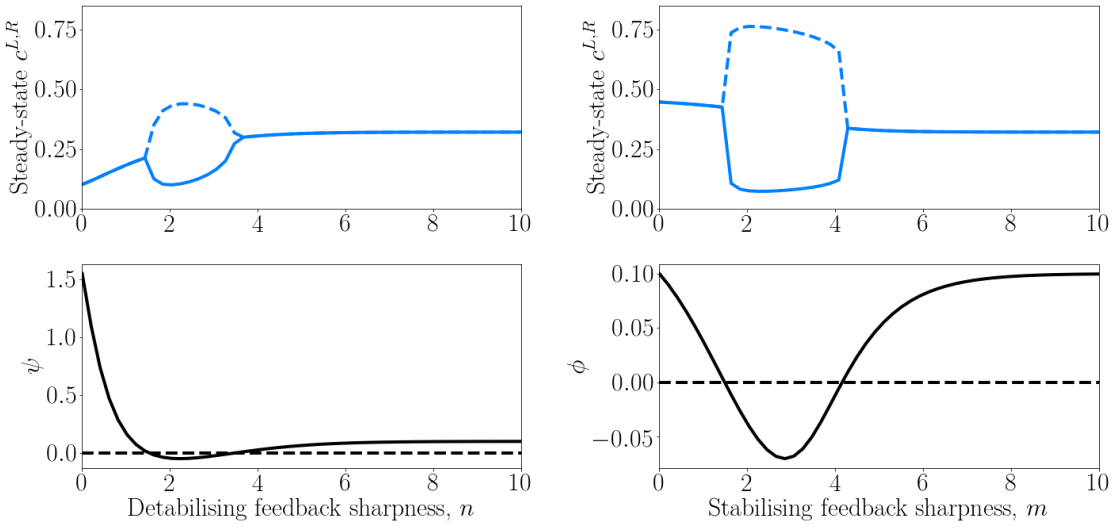

(a) (b)

Fig. 3.5 Bifurcation analysis of the binding feedback model (3.14)–(3.19) with respect to feedback sharpness. Non-dimensional parameter values are $\nu = 0.1$, $\gamma = 1$, $\delta = 0.01$, $\sigma = 1$, $\varepsilon = 0.01$, $\kappa = 1$, $\eta = 30$, $\rho = 1$, $\mu = 30$. Solid lines: L; dashed lines: R (upper panels).

occur. In addition, comparing Fig. 3.6a and Fig. 3.6c, we find that a lower value of γ suffices for polarisation in the case of stabilising feedback than in the case of destabilising feedback. In summary, for a given strength of feedback, it is possible to induce polarisation if the total concentration of protein b is sufficiently large relative to that of protein a in our model.

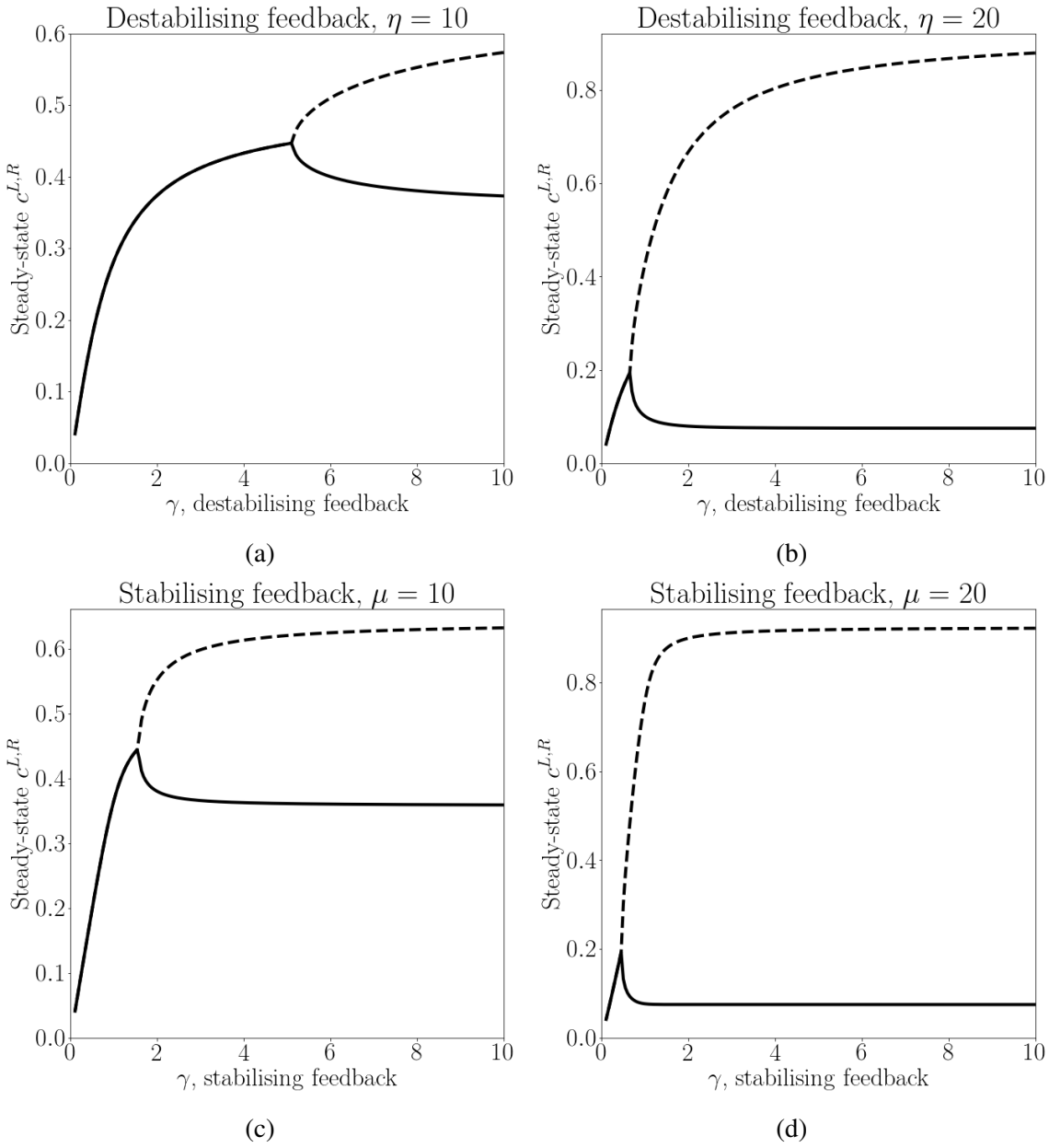

Fig. 3.6 Bifurcation analysis of the binding feedback model (3.14)–(3.19) with respect to the ratio of total protein concentrations in each cell. Non-dimensional parameter values are $\nu = 0.1$, $\delta = 0.01$, $\sigma = 1$, $\varepsilon = 0.01$; feedback parameters are $\kappa = 1$, $n = 2$, $\rho = 1$, and $m = 2$. Solid lines: L; dashed lines: R.

Clone phenotypes

Having explored how different parameters affect the occurrence of polarisation in a normal tissue, we next investigate the behaviour of cells neighbouring a group of cells in which the abundance of each protein is perturbed. This corresponds biologically to the creation of a mutant clone in which the relevant gene is over- or underexpressed (see Section 1.3). In our model, a clone is defined as a set of cell indices $i \in \mathscr{I}$ for which $2a_i + 2c_i = r < 1$ and/or $2\gamma b_i + 2c_i = \gamma r < \gamma$, where the parameter r denotes the fraction of the normal total concentration of protein a and or b in each cell. In the simulations shown below, we take $r = 0.1$ and $\mathscr{I} = \{13, \ldots, 17\}$. We show results for: (i) clones in which only the total amount of a in each mutant cell is underexpressed, referred to as 'single a^- clones'; (ii) clones in which both a and b in each mutant cell are underexpressed, referred to as 'double a^-b^- clones'.

Fig. 3.7 and Fig. 3.8 show example simulations demonstrating perturbed polarisation in cells surrounding single and double clones in the cases of destabilising and stabilising feedback, respectively. For destabilising feedback with a single clone (Fig. 3.7a), we observe that some cells outside the clone have 'reversed' polarity, in the sense that they reach a stable steady state in which $c^L > c^R$, despite the opposing bias in the initial condition (3.58). This corresponds to the *domineering non-autonomy* phenotype that we previously discussed in the context of the core pathway in the fly wing (Section 1.3). This is largely ameliorated in the case of a double clone (Fig. 3.7b), with most cells neighbouring the clone exhibiting the 'correct' polarity. For stabilising feedback, single clones (Fig. 3.8a) induce domineering non-autonomy in a qualitatively similar way to the case of destabilising feedback. However, curiously the cells neighbouring a double clone (Fig. 3.8b) exhibit a 'period two' pattern, with adjacent cells having opposing polarities throughout the tissue. (Note that if a larger number of cells is used in the tissue, then we observe a finite extent of mispolarisation; results

not shown.) In summary, the types of perturbation and feedback interaction both affect the resulting tissue-scale polarisation in our simulations.

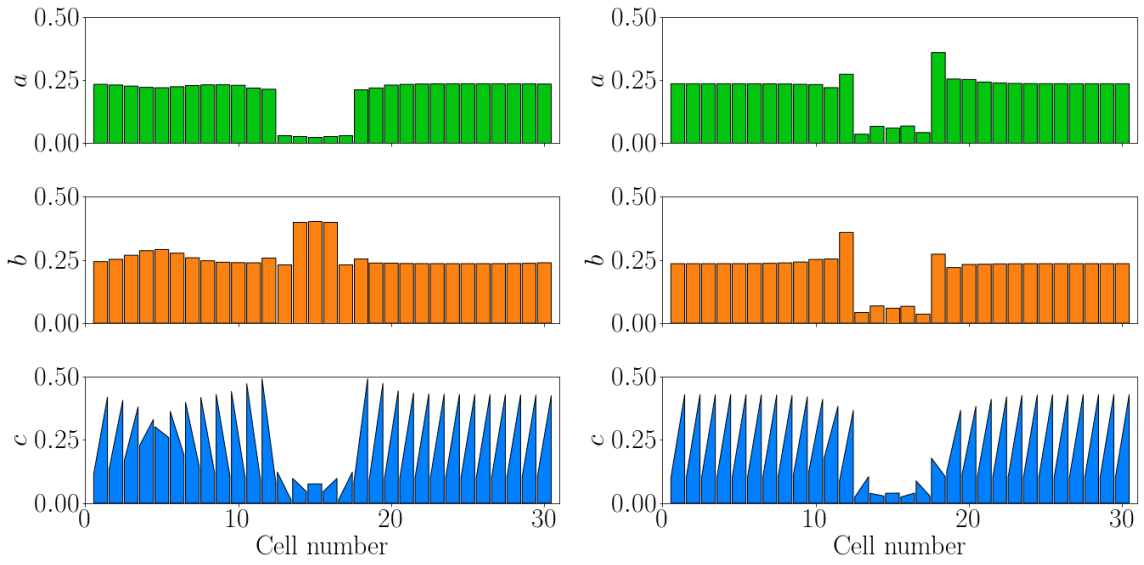

Fig. 3.7 Perturbed polarisation in the binding feedback model (3.14)–(3.19), with destabilising feedback, for cells neighbouring (a) a single a^- clone and (b) a double a^-b^- clone. Non-dimensional parameter values are $\nu = 0.1$, $\gamma = 1$, $\delta = 0.01$, $\sigma = 1$, $\varepsilon = 0.01$, $\eta = 30$, $\kappa = 1$, $n = 2$. Numerical solution shown at $t = 5 \times 10^3$.

Next, we explore how the *range* of domineering non-autonomy (measured by the number of cells with reversed polarity at steady state) around single and double clones for each form of feedback depends on the strength of feedback (Fig. 3.9). We identify two main differences between the cases of destabilising (Fig. 3.9a) and stabilising (Fig. 3.9b) feedback. The first difference is that for destabilising feedback the range of non-autonomy increases with feedback strength up to $\eta \approx 20$, then decreases significantly with higher feedback strengths; whereas for stabilising feedback, the corresponding 'maximum range of non-autonomy' occurs at a lower feedback strength ($\mu \approx 10$), and the decrease at higher feedback strengths is more mild. The second difference is that for destabilising feedback, the range of non-autonomy is much higher around single clones than double clones; whereas for stabilising

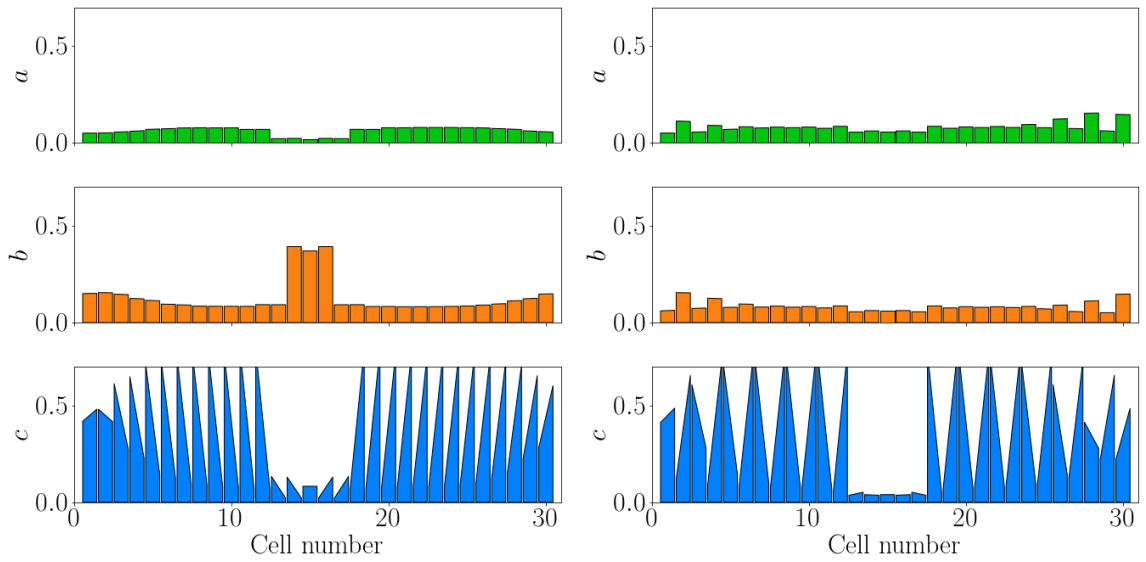

(a) (b)

Fig. 3.8 Perturbed polarisation in the binding feedback model (3.14)–(3.19), with stabilising feedback, for cells neighbouring (a) a single a^- clone and (b) a double a^-b^- clone. Non-dimensional parameter values are $\nu = 0.1$, $\gamma = 1$, $\delta = 0.01$, $\sigma = 1$, $\varepsilon = 0.01$, $\mu = 30$, $\rho = 1$, $m = 2$. Numerical solution shown at $t = 5 \times 10^3$.

feedback the range of non-autonomy appears to be independent of clone type, though the double clone induces a period two pattern rather than simply reversing polarity.

The above results show that either destabilising or stabilising feedback can suffice to drive the SUSS to be unstable and generate planar polarisation in this model. In each case, a minimum strength or sharpness of feedback is required for polarisation to occur. Our clone simulations suggest that the case of destabilising feedback may be more directly related to the experimental findings of Fisher et al. [63], namely that inducing a double Fz^- Vang^- clone in the fly wing largely rescues the domineering non-autonomy phenotype observed for a single Fz^- or Vang^- clone. In the case of single clones, our simulations suggest a counter-intuitive, nonlinear dependence of the range of non-autonomy on feedback strength. In the next section we consider an alternative hypothesised mechanism, whereby an initial bias may be amplified through the modulation of rates of protein *trafficking* within each cell.

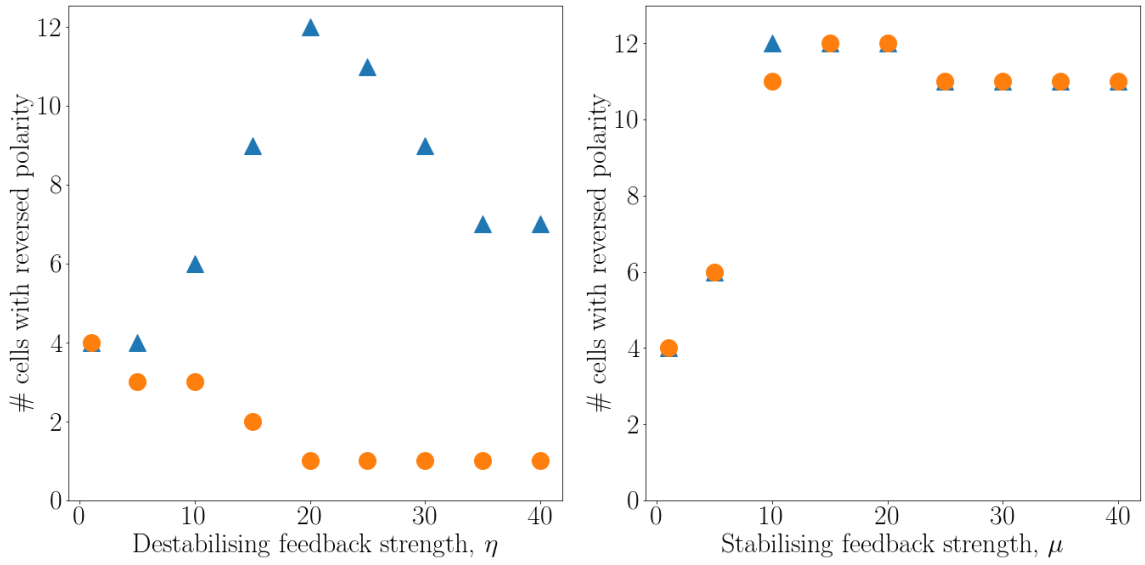

(a) (b)

Fig. 3.9 Range of domineering non-autonomy in the binding feedback model with (a) destabilising and (b) stabilising feedback. Blue triangles: a^- clone; orange circles: a^-b^- clone. Non-dimensional parameter values are $\nu = 0.1$, $\gamma = 1$, $\delta = 0.01$, $\sigma = 1$, $\varepsilon = 0.01$, $\rho = 1$, $m = 2$, $\kappa = 1$, $n = 2$. Numerical solution shown at $t = 10^5$.

3.3 Trafficking feedback model

We now suppose that feedback acts not on (un)binding rates, but instead on the rate of protein trafficking within each cell, which for simplicity we model as a diffusive process. In this model, we assume that the complex C can alter the local rate of endocytosis of unbound proteins from the cell membrane, and hence their rate of transport away to the opposing cell edge. Below, we present the governing equations for this model, which are modifications of (3.5)–(3.10), for two cases: destabilising and stabilising feedback. Unlike Section 3.2, we present each feedback case as a separate model, since it is not so straightforward to write a general model that encompasses both cases.

3.3.1 Governing equations

Destabilising feedback

Here, we assume that the higher the complex concentration of each orientation at a cell-cell interface is, the higher the rate of diffusion of unbound proteins of the opposite orientation away from that cell-cell interface is. This could be biologically interpreted as an increase in the rate of endocytosis followed by unpolarised trafficking back to either the left or right cell edge, as the complex concentration increases. The governing equations are thus given by

$$\dot{A}_i^L = -kA_i^L B_{i-1}^R + vC_i^L + D_{A1}(C_{i+1}^L)A_i^R - D_{A1}(C_{i-1}^R)A_i^L, \tag{3.61}$$

$$\dot{A}_i^R = -kA_i^R B_{i+1}^L + vC_i^R + D_{A1}(C_{i-1}^R)A_i^L - D_{A1}(C_{i+1}^L)A_i^R, \tag{3.62}$$

$$\dot{B}_i^L = -kA_{i-1}^R B_i^L + vC_{i-1}^R + D_{B1}(C_i^R)B_i^R - D_{B1}(C_i^L)B_i^L, \tag{3.63}$$

$$\dot{B}_i^R = -kA_{i+1}^L B_i^R + vC_{i+1}^L + D_{B1}(C_i^L)B_i^L - D_{B1}(C_i^R)B_i^R, \tag{3.64}$$

$$\dot{C}_i^L = kA_i^L B_{i-1}^R - vC_i^L, \tag{3.65}$$

$$\dot{C}_i^R = kA_i^R B_{i+1}^L - vC_i^R, \tag{3.66}$$

where unlike Section 3.2 the rate coefficients k and v are both assumed to be constant, while the diffusion coefficients D_{A1} and D_{B1} may depend on the local complex concentration in a monotonic increasing manner.

For consistency of analysis, we use the same non-dimensionalisation as in Section 3.2, taking $\mathscr{K} = \mathscr{V} = 1$. We also take $D_{A1} = D_{a1}A_{\text{tot}}$ and $D_{B1} = D_{b1}B_{\text{tot}}$, where D_{a1} and D_{b1} denote the dimensionless functions. This gives the non-dimensionalised system

$$\dot{a}_i^L = -\gamma a_i^L b_{i-1}^R + \nu c_i^L + \alpha\left(D_{a1}(c_{i+1}^L)a_i^R - D_{a1}(c_{i-1}^R)a_i^L\right), \tag{3.67}$$

$$\dot{a}_i^R = -\gamma a_i^R b_{i+1}^L + \nu c_i^R + \alpha\left(D_{a1}(c_{i-1}^R)a_i^L - D_{a1}(c_{i+1}^L)a_i^R\right), \tag{3.68}$$

$$\dot{b}_i^L = -a_{i-1}^R b_i^L + \frac{\nu}{\gamma}c_{i-1}^R + \alpha\gamma\left(D_{b1}(c_i^R)b_i^R - D_{b1}(c_i^L)b_i^L\right), \tag{3.69}$$

$$\dot{b}_i^R = -a_{i+1}^L b_i^R + \frac{\nu}{\gamma} c_{i+1}^L + \alpha\gamma\left(D_{b1}(c_i^L) b_i^L - D_{b1}(c_i^R) b_i^R\right), \tag{3.70}$$

$$\dot{c}_i^L = \gamma a_i^L b_{i-1}^R - \nu c_i^L, \tag{3.71}$$

$$\dot{c}_i^R = \gamma a_i^R b_{i+1}^L - \nu c_i^R, \tag{3.72}$$

where γ and ν are as defined in (3.13) and $\alpha = 1/k_0$. Note that $D_{a1}(0) = D_{b1}(0) = 1$, and that the conservation laws given by equations (3.30) and (3.31) still hold for this system. In the following, we assume that if a and b are both affected by destabilising feedback, then they are so in an equivalent manner ($D_{a1} = D_{b1} = D_1$).

Stabilising feedback

Here, we assume that the higher the complex concentration of each orientation at a cell-cell interface is, the lower the rate of diffusion of unbound proteins of that orientation away from that cell-cell interface is. Proceeding in a similar manner to the case of destabilising feedback leads to the non-dimensionalised system of governing equations

$$\dot{a}_i^L = -\gamma a_i^L b_{i-1}^R + \nu c_i^L + \alpha\left(D_{a2}(c_i^R) a_i^R - D_{a2}(c_i^L) a_i^L\right), \tag{3.73}$$

$$\dot{a}_i^R = -\gamma a_i^R b_{i+1}^L + \nu c_i^R + \alpha\left(D_{a2}(c_i^L) a_i^L - D_{a2}(c_i^R) a_i^R\right), \tag{3.74}$$

$$\dot{b}_i^L = -a_{i-1}^R b_i^L + \frac{\nu}{\gamma} c_{i-1}^R + \alpha\gamma\left(D_{b2}(c_{i+1}^L) b_i^R - D_{b2}(c_{i-1}^R) b_i^L\right), \tag{3.75}$$

$$\dot{b}_i^R = -a_{i+1}^L b_i^R + \frac{\nu}{\gamma} c_{i+1}^L + \alpha\gamma\left(D_{b2}(c_{i-1}^R) b_i^L - D_{b2}(c_{i+1}^L) b_i^R\right), \tag{3.76}$$

$$\dot{c}_i^L = \gamma a_i^L b_{i-1}^R - \nu c_i^L, \tag{3.77}$$

$$\dot{c}_i^R = \gamma a_i^R b_{i+1}^L - \nu c_i^R, \tag{3.78}$$

where D_{a2} and D_{b2} may be monotonic *decreasing* functions of their arguments, and we have $D_{a2}(0) = D_{b2}(0) = 1$. In the following, we assume that if a and b are both affected by stabilising feedback, then they are so in an equivalent manner ($D_{a2} = D_{b2} = D_2$).

3.3.2 Steady state and linear stability analysis

Having constructed our trafficking feedback model for the case of destabilising and stabilising feedback, we next consider the existence of any positive SUSS (a,b,c) and its linear stability to spatially homogeneous perturbations.

We first seek positive, homogeneous SUSS solution(s) of the system (3.67)–(3.72). Substituting $a_i^L(t) = a_i^R(t) = a$, $b_i^L(t) = b_i^R(t) = b$, and $c_i^L(t) = c_i^R(t) = c$ into (3.72), (3.30) and (3.31), we find that a, b and c must satisfy

$$\gamma ab - \nu c = 0, \tag{3.79}$$

$$2a + 2c = 1, \tag{3.80}$$

$$2\gamma b + 2c = \gamma, \tag{3.81}$$

regardless of whether feedback is present or absent. A similar result is found in the case of stabilising feedback. This means that, for both forms of feedback, there is always a unique positive SUSS that is given (following the analysis presented in Section 3.2.2) by (3.36)–(3.38). We next consider the linear stability of this SUSS under each form of feedback.

Destabilising feedback

Applying (3.41) to the system (3.67)–(3.72), linearising, then applying (3.48)–(3.49), we obtain the system

$$\dot{s_a} = -\gamma b s_a - \gamma a s_b + \nu s_c, \tag{3.82}$$

$$\dot{s_b} = -b s_a - a s_b + \frac{\nu}{\gamma} s_c, \tag{3.83}$$

$$\dot{s_c} = \gamma b s_a + \gamma a s_b - \nu s_c, \tag{3.84}$$

$$\dot{d_a} = -(\gamma b + 2\alpha D_{a1}) d_a + \gamma a d_b + (\nu + 2\alpha a D'_{a1}) d_c, \tag{3.85}$$

$$\dot{d}_b = bd_a - (a + 2\alpha\gamma D_{b1})d_b - \left(\frac{\nu}{\gamma} + 2\alpha\gamma b D'_{b1}\right) d_c, \tag{3.86}$$

$$\dot{d}_c = \gamma b d_a - \gamma a d_b - \nu d_c. \tag{3.87}$$

Similar to our analysis in Section 3.2.2, we find that the characteristic polynomial $F(\lambda)$ of the Jacobian of (3.82)–(3.87) is given by the product of the two polynomials

$$F_s(\lambda) = -\lambda^2(\lambda + a + \gamma b + \nu), \tag{3.88}$$

$$F_d(\lambda) = -\lambda^3 - \alpha_2\lambda^2 - \alpha_1\lambda - \alpha_0, \tag{3.89}$$

where

$$\alpha_0 = 4\alpha^2\gamma[\nu D_{a1}D_{b1} - \gamma ab(D_{a1}D'_{b1} + D'_{a1}D_{b1})], \tag{3.90}$$

$$\alpha_1 = 2\alpha[D_{a1}(a+\nu) + \gamma D_{b1}(\nu + \gamma b + 2\alpha D_{a1}) - \gamma ab(D'_{a1} + \gamma D'_{b1})], \tag{3.91}$$

$$\alpha_2 = a + \gamma b + \nu + 2\alpha(D_{a1} + \gamma D_{b1}), \tag{3.92}$$

By inspection, the function $F_s(\lambda)$ has roots $\lambda_{1,2} = 0$ and $\lambda_3 = -a - \gamma b - \nu$, the latter being negative since all model parameters and the SUSS are positive.

In the absence of feedback ($D_{a1} = D_{b1} = 1$), we have

$$\alpha_0 = 4\alpha^2\gamma\nu, \tag{3.93}$$

$$\alpha_1 = 2\alpha[a + \nu + \gamma(\nu + \gamma b + 2\alpha)], \tag{3.94}$$

$$\alpha_2 = a + \gamma b + \nu + 2\alpha(1+\gamma), \tag{3.95}$$

which are all positive; hence, by Descartes' rule of signs, (3.89) has no positive roots, and thus the SUSS is linearly stable to spatially homogeneous perturbations.

In the presence of feedback, there are three cases to consider. If feedback acts upon the trafficking of a alone ($D_{b1} = 1$), then there is exactly one positive root when $\nu D_{a1} - \gamma ab D'_{a1} < 0$. Similarly, if feedback acts upon the trafficking of b alone ($D_{a1} = 1$), then there is exactly one positive root when $\nu D_{b1} - \gamma ab D'_{b1} < 0$. Finally, if feedback acts upon the trafficking of both a and b, then there is exactly one positive root when $\Delta = \nu D_1 - 2\gamma ab D'_1 < 0$, where $D_{a1} = D_{b1} = D_1$.

Stabilising feedback

Following a similar approach, in the case of stabilising feedback we find that the characteristic polynomial $F(\lambda)$ whose eigenvalues determine the stability of the SUSS is given by the product of the polynomial $F_s(\lambda)$ given by (3.88) and the polynomial

$$F_d(\lambda) = -\lambda^3 - \alpha_2\lambda^2 - \alpha_1\lambda - \alpha_0, \tag{3.96}$$

where

$$\alpha_0 = 4\alpha^2\gamma[\nu D_{a2}D_{b2} + \gamma ab(D_{a2}D'_{b2} + D'_{a2}D_{b2})], \tag{3.97}$$

$$\alpha_1 = 2\alpha[D_{a2}(a+\nu) + \gamma D_{b2}(2\alpha D_{a2} + \nu) + \gamma ab(D'_{a2} + \gamma D'_{b2})], \tag{3.98}$$

$$\alpha_2 = a + \gamma b + \nu + 2\alpha(D_{a2} + \gamma D_{b2}). \tag{3.99}$$

In the absence of feedback, these coefficients simplify to

$$\alpha_0 = 4\alpha^2\gamma\nu, \tag{3.100}$$

$$\alpha_1 = 2\alpha[a + \nu + \gamma(2+\nu)], \tag{3.101}$$

$$\alpha_2 = a + \gamma b + \nu + 2\alpha(1+\gamma), \tag{3.102}$$

which are all positive; hence, by Descartes' rule of signs, (3.96) has no positive roots, and thus the SUSS is linear stable to spatially homogeneous perturbations.

In the presence of feedback, the situation is very similar to the destabilising case. If feedback acts upon the trafficking of a alone ($D_{b1} = 1$), then there is exactly one positive root when $\nu D_{a2} + \gamma ab D'_{a2} < 0$. Similarly, if feedback acts upon the trafficking of b alone ($D_{a1} = 1$), then there is exactly one positive root when $\nu D_{b2} + \gamma ab D'_{b2} < 0$. Finally, if feedback acts upon the trafficking of both a and b, then there is exactly one positive root when $\Omega = \nu D_2 + 2\gamma ab D'_2 < 0$.

In summary, we have obtained inequalities that must be satisfied for the SUSS to become linearly unstable to spatially homogeneous perturbations in our trafficking feedback model.

3.3.3 Numerical simulations

In this section we verify our analytical results numerically and conduct a similar numerical investigation to that presented in Section 3.2.3 for the binding feedback model. As before, we consider a ring of $N = 30$ cells of equal size, imposing periodic boundary conditions and the initial condition (3.58). Unless stated otherwise, we use the same parameter values as in Section 3.2.3.

For our numerical simulations, we must choose specific functional forms for our feedback functions D_{a1} and D_{a2} (equivalently, D_{b1} and D_{b2}). We choose sigmoidal functions

$$D_{a1}(c) = 1 + \frac{(\eta_D - 1)c^{n_D}}{\kappa_D^{n_D} + c^{n_D}}, \tag{3.103}$$

$$D_{a2}(c) = \mu_D + \frac{(1 - \mu_D)c^{m_D}}{\rho_D^{m_D} + c^{m_D}}, \tag{3.104}$$

emphasising that D_{a1} is monotonic increasing while D_{a2} is monotonic decreasing (assuming $\eta_D > 1$ and $\mu_D > 1$). Note that we use the same symbols for feedback strength and sharpness

as in the binding feedback model (3.59)–(3.60), but include an additional subscript D to highlight that these parameters relate to the trafficking (i.e. diffusion) feedback model.

Polarisation in the presence of trafficking feedback

We first illustrate how the presence of trafficking feedback can result in polarisation in this model. Fig. 3.10 shows numerical results in the case of destabilising feedback for an example parameter set. As with the binding feedback model, qualitatively similar results are obtained in the case of stabilising feedback (results not shown). Note that in contrast to the binding feedback model, here the unbound protein concentrations polarise as well as the complex concentrations in each cell. We also see much stronger steady-state polarisation than for the binding feedback model (compare Fig. 3.10b with Fig. 3.3b), although this of course depends on the chosen parameter set.

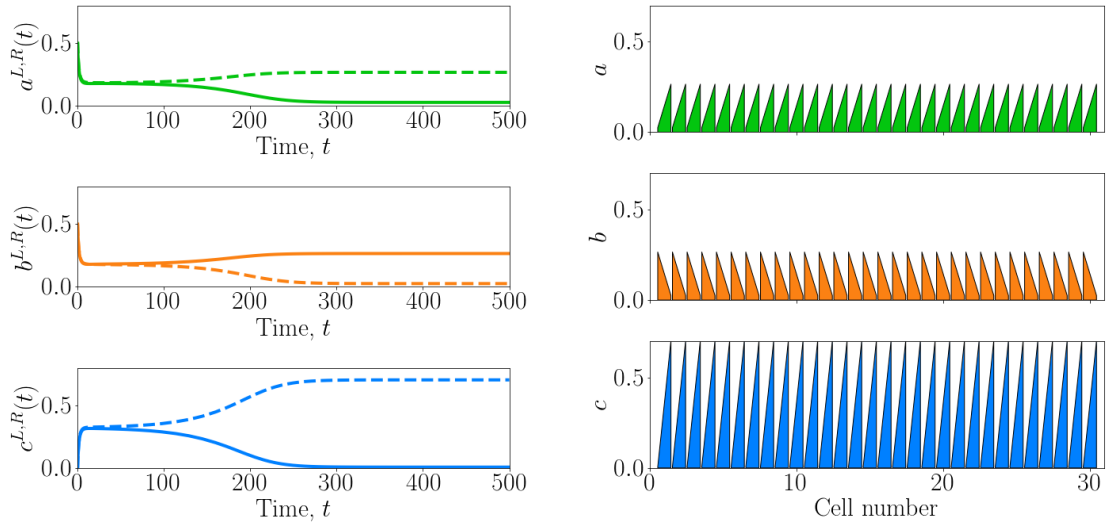

(a) (b)

Fig. 3.10 Numerical solution of the trafficking feedback model with destabilising feedback (3.67)–(3.72) with initial condition (3.58). Non-dimensional parameter values are $\nu = 0.1$, $\gamma = 1$, $\varepsilon = 0.01$, $\alpha = 0.01$, $\eta_D = 30$, $\kappa_D = 1$, $n_D = 2$. (a) Solid lines: L; dashed lines: R. Numerical solution shown at $t = 10^5$.

Dependence of polarisation on trafficking feedback strength and sharpness

Next, we explore whether a certain strength, or sharpness, of trafficking feedback is required for polarisation. We consider a single cell with 'periodic' boundary conditions rather than simulating the full tissue.

The upper graphs of Fig. 3.11 show the steady-state values of c^L and c^R for feedback strengths η_D and μ_D ranging from 1 to 30, in the case where feedback acts upon the diffusion rates of both unbound proteins equally. As with the binding feedback model, we observe a pitchfork bifurcation, with the SUSS losing stability at critical values of $\eta_D \approx 5$ (Fig. 3.11a) and $\mu_D \approx 5$ (Fig. 3.11b), respectively. The lower graphs of Fig. 3.11 show that above these critical values, the terms Δ and Ω defined in our linear stability analysis above become negative. This confirms our theoretical analysis and shows that sufficiently strong feedback is required to drive the system away from the SUSS and into a stable polarised state. Note that the critical feedback strengths for polarisation are much lower than those for the binding feedback model, and holding all other parameters fixed, destabilising trafficking feedback generates much stronger polarity than equivalent destabilising binding feedback.

We next examine how the feedback sharpness affects the system's polarity for a fixed trafficking feedback strength. As Fig. 3.12 shows, there is an intermediate set sharpness values for which polarisation occurs. This is similar to our results for the binding feedback model, albeit with quantitatively difference lower and upper critical values for the sharpness parameters n_D, m_D compared to n, m.

Clone phenotypes

We next investigate the behaviour of cells neighbouring a group of cells in which the abundance of each protein is perturbed. We implement single and double clones as described in Section 3.2.3. Fig. 3.13 and Fig. 3.14 show example simulations demonstrating perturbed polarisation in cells surrounding single and double clones in the cases of destabilising and

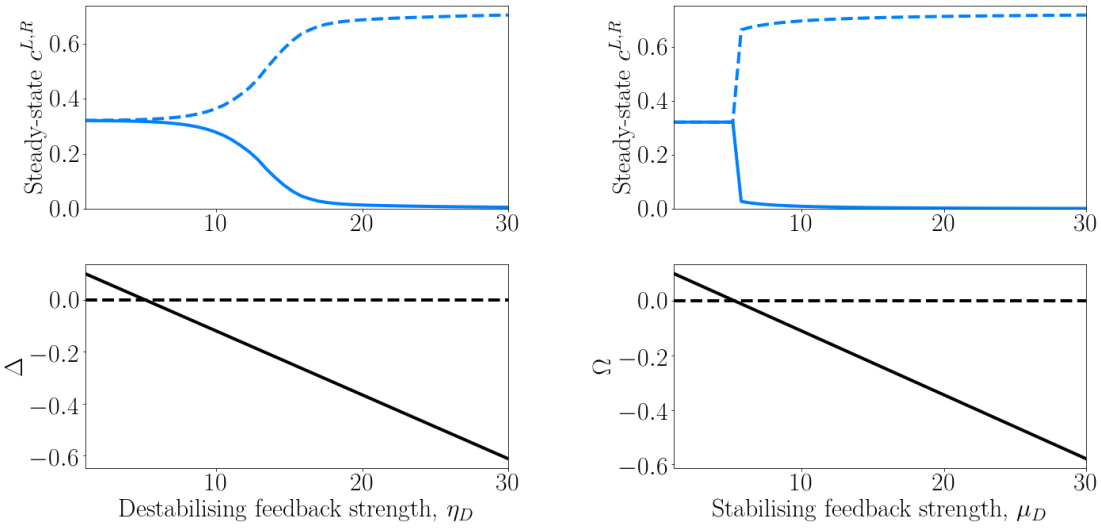

(a) (b)

Fig. 3.11 Bifurcation analysis of the trafficking feedback model with (a) destabilising feedback (3.67)–(3.72) and (b) stabilising feedback (3.73)-(3.78) with respect to feedback strength. For each value of feedback strength, each system is solved numerically for one cell. Non-dimensional parameter values are $\nu = 0.1$, $\gamma = 1$, $\varepsilon = 0.01$, $\alpha = 0.01$, $\kappa_D = 1$, $n_D = 2$, $\rho_D = 0.1$, $m_D = 2$. Numerical solution shown at $t = 10^5$. Solid lines: L; dashed lines: R (upper panels).

stabilising trafficking feedback, respectively. As with the binding feedback model, we find that destabilising and stabilising feedback are both capable of generating non-autonomy around single clones. Cells immediately neighbouring a single a^- clone localise away from the clone (Fig. 3.13a and Fig. 3.14a). These simulations also reveal a variety of non-autonomy behaviours around double a^-b^- clones. For instance, for a high destabilising feedback strength, we observe no non-autonomy around a double a^-b^- clone (Fig. 3.13b), while for all stabilising feedback strengths (e.g. $\mu_D = 30$; Fig. 3.14b), period two patterns are observed.

Fig. 3.15 illustrates how the range of non-autonomy varies with feedback strength for destabilising and stabilising feedback, respectively. In the case of a single a^- clone, maximum disruption is observed for an intermediate value of the feedback strength, whose value is the same for destabilising and stabilising feedback ($\eta_D = \mu_D \approx 5$).

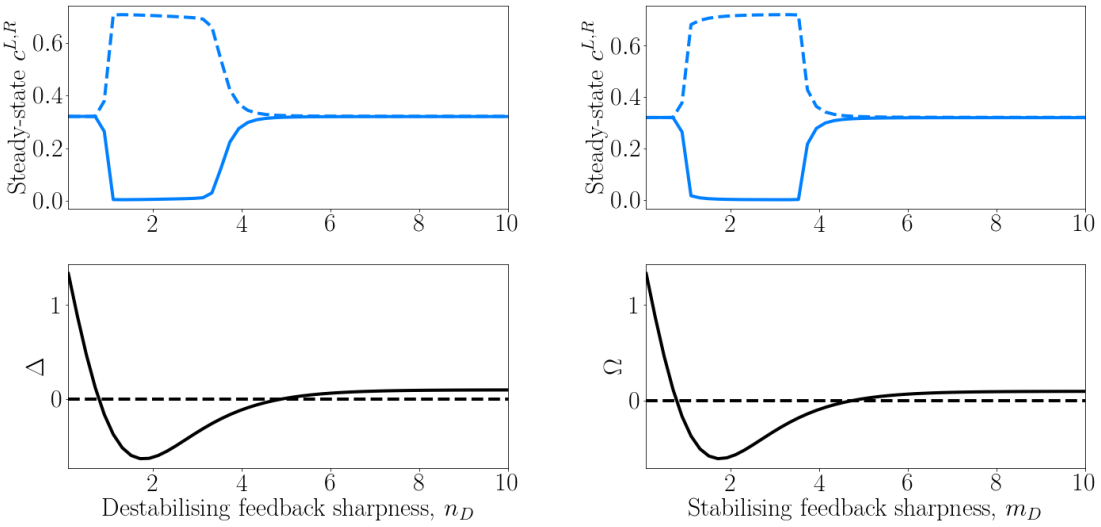

(a) (b)

Fig. 3.12 Bifurcation analysis of the trafficking feedback model with (a) destabilising feedback (3.67)–(3.72) and (b) stabilising feedback (3.73)-(3.78) with respect to feedback sharpness. For each value of feedback sharpness, the systems are solved numerically for one cell. Non-dimensional parameter values are $\nu = 0.1$, $\gamma = 1$, $\varepsilon = 0.01$, $\alpha = 0.01$, $\kappa_D = 1$, $\eta_D = 20$, $\rho_D = 0.1$, $\mu_D = 20$. The solution is shown at $t = 10^5$. Solid lines: L; dashed lines: R (upper panels).

For such clones, with even stronger feedback the range of non-autonomy decreases, counter-intuitively. In the case of a double $a^- b^-$ clone, the range of non-autonomy again has a maximum for $\mu_D \approx 5$ in the case of stabilising feedback (Fig. 3.15b). However, for destabilising feedback (Fig. 3.15a), the range of non-autonomy appears to *decrease* with feedback strength, with no non-autonomy observed beyond a critical feedback strength ($\eta_D \approx 10$).

Taken together, these results suggest that if feedback interactions were to operate by modulating unbound protein trafficking rates within each cell, then we may be able to distinguish whether such feedback is destabilising or stabilising by observing whether there is non-autonomy around double clones. Again, this has potential implications for how to interpret experimental observations of mutant clone phenotypes in the core planar polarity pathway. In the next section we consider a third hypothesised mechanism, whereby an initial

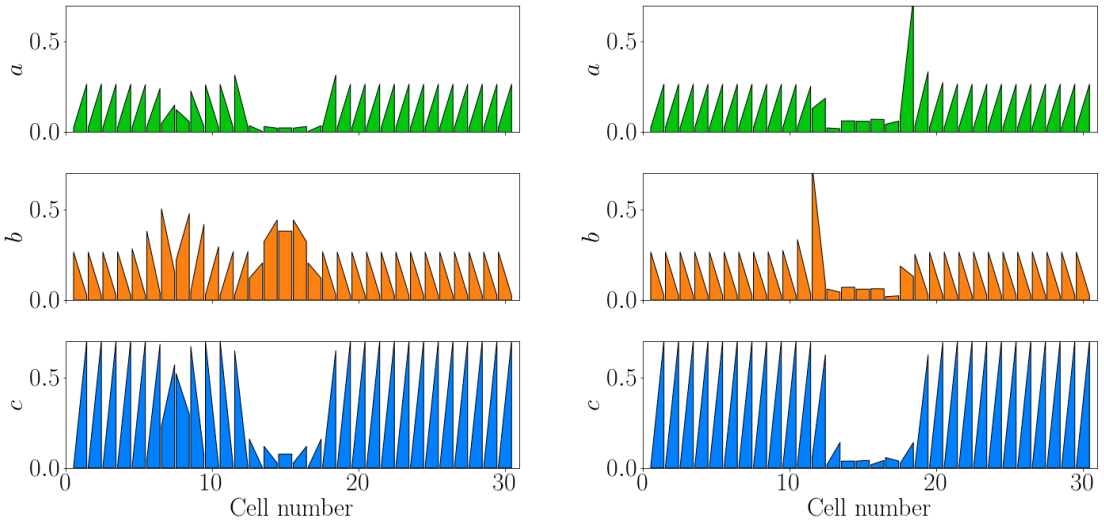

Fig. 3.13 Perturbed polarisation in the trafficking feedback model with destabilising feedback (3.67)–(3.72), for cells neighbouring (a) a single a^- clone and (b) a double a^-b^- clone. Non-dimensional parameter values are $\nu = 0.1$, $\gamma = 1$, $\delta = 0.01$, $\sigma = 1$, $\varepsilon = 0.01$, $\eta_D = 30$, $\kappa_D = 1$, $n_D = 2$. Numerical solution shown at $t = 10^5$.

bias may be amplified through the modulation of rates of protein *degradation* within each cell.

3.4 Degradation feedback model

In our third model, we supposed that feedback acts on the rate of *degradation* of proteins A and/or B. From a biological perspective, a destabilising feedback between complexes of opposing orientations might occur via e.g. targeted ubiquitination [73]. The inclusion of protein degradation in this model necessitates the inclusion of protein 'production' to avoid the protein concentrations tending to zero over time. This also 'breaks' mass conservation, in the sense that the total protein concentrations (3.11) and (3.12) are not conserved over time in this model.

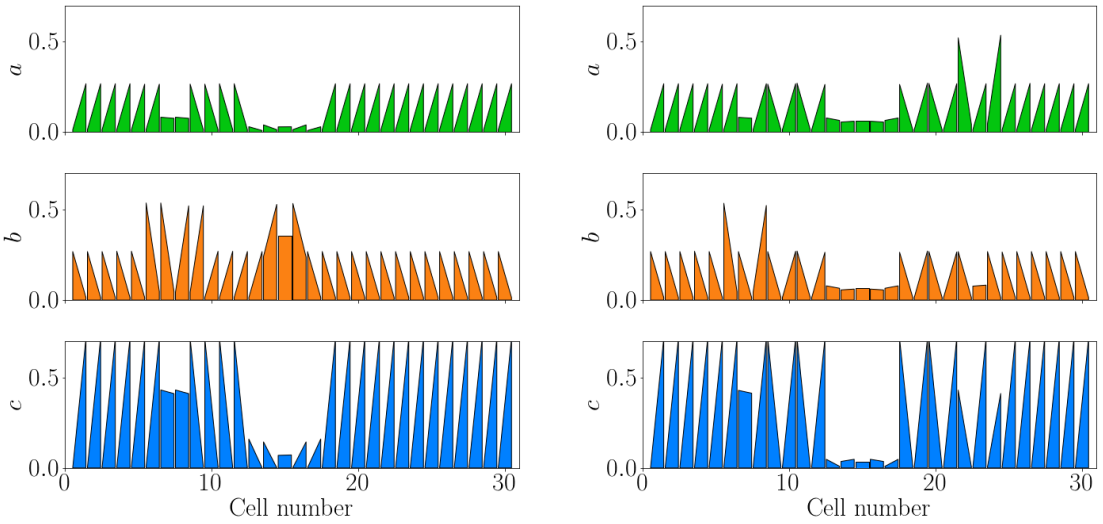

(a) (b)

Fig. 3.14 Perturbed polarisation in the trafficking feedback model with stabilising feedback (3.73)–(3.78), for cells neighbouring (a) a single a^- clone and (b) a double a^-b^- clone. Non-dimensional parameter values are $\nu = 0.1$, $\gamma = 1$, $\delta = 0.01$, $\sigma = 1$, $\varepsilon = 0.01$, $\mu_D = 30$, $\rho_D = 0.1$, $m_D = 2$. Numerical solution shown at $t = 10^5$.

3.4.1 Governing equations

In this model, we assume (as in the trafficking feedback model) that proteins A and B undergo reversible binding according to (3.1)–(3.2) with constant forward and backward rate coefficients k and ν, respectively. In addition, we assume (as in the binding feedback model) that proteins A and B undergo trafficking that may be described by diffusion between cell compartments according to (3.3)–(3.4) with constant diffusion coefficients D_A and D_B, respectively. However, in contrast to the two previous models, we assume that proteins A and B are produced constitutively in each cell compartment according to the reactions

$$\emptyset \longrightarrow A_i^L, \tag{3.105}$$

$$\emptyset \longrightarrow A_i^R, \tag{3.106}$$

$$\emptyset \longrightarrow B_i^L, \tag{3.107}$$

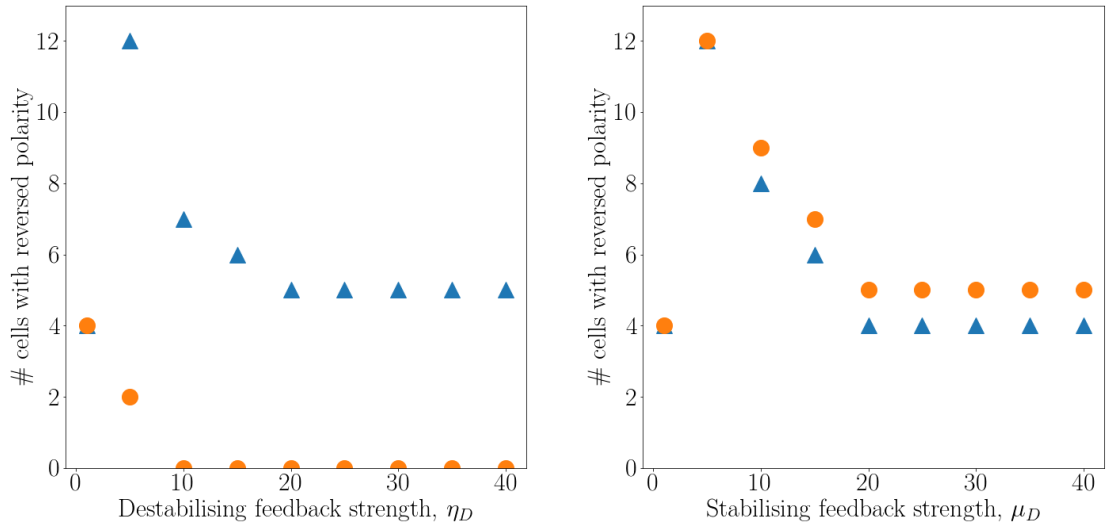

(a) (b)

Fig. 3.15 Range of domineering non-autonomy in the trafficking feedback model with (a) destabilising and (b) stabilising feedback. Blue triangles: a^- clone; orange circles: a^-b^- clone. Non-dimensional parameter values are $\nu = 0.1$, $\gamma = 1$, $\delta = 0.01$, $\sigma = 1$, $\varepsilon = 0.01$, $\rho_D = 0.1$, $m_D = 2$, $\kappa_D = 1$, and $n_D = 2$. Numerical solution shown at $t = 10^5$.

$$\emptyset \longrightarrow B_i^R, \tag{3.108}$$

with constant rate coefficients W_A and W_B, respectively. We also assume that the complex in each cell compartment degrades according to the reactions

$$C_i^L \longrightarrow \emptyset, \tag{3.109}$$

$$C_i^R \longrightarrow \emptyset, \tag{3.110}$$

with shared rate coefficient q that may depend on the local complex concentration (of the opposing orientation). Applying the above assumptions, the governing equations are thus given by

$$\frac{dA_i^L}{dT} = -kA_i^L B_{i-1}^R + \nu C_i^L + D_A(A_i^R - A_i^L) + W_A, \tag{3.111}$$

$$\frac{dA_i^R}{dT} = -kA_i^R B_{i+1}^L + vC_i^R + D_A(A_i^L - A_i^R) + W_A, \tag{3.112}$$

$$\frac{dB_i^L}{dT} = -kA_{i-1}^R B_i^L + vC_{i-1}^R + D_B(B_i^R - B_i^L) + W_B, \tag{3.113}$$

$$\frac{dB_i^R}{dT} = -kA_{i+1}^L B_i^R + vC_{i+1}^L + D_B(B_i^L - B_i^R) + W_B, \tag{3.114}$$

$$\frac{dC_i^L}{dT} = kA_i^L B_{i-1}^R - vC_i^L - q(C_{i-1}^R)C_i^L, \tag{3.115}$$

$$\frac{dC_i^R}{dT} = kA_i^R B_{i+1}^L - vC_i^R - q(C_{i+1}^L)C_i^R. \tag{3.116}$$

We non-dimensionalise this model as follows. We write $q = q_0\mathscr{Q}$, where q_0 denotes a baseline value of the degradation rate coefficient, and $\mathscr{Q}$ may be either equal to 1 (corresponding to no feedback) or given by some monotonic increasing function of its argument. We write $T = t/q_0$ and $A_i^j = q_0 a_i^j$, $B_i^j = q_0 b_i^j$, $C_i^j = q_0 c_i^j$ for $j \in \{L,R\}$, a_i^j, b_i^j, c_i^j and t denote dimensionless variables. Finally, we define dimensionless lumped parameters

$$\beta = \frac{1}{kq_0}, \quad \theta_a = \frac{D_A}{kq_0}, \quad \theta_b = \frac{D_B}{kq_0}, \qquad \omega_a = \frac{W_A}{kq_0^2}, \quad \omega_b = \frac{W_B}{kq_0^2}, \quad \zeta = \frac{1}{k}. \tag{3.117}$$

Substituting into (3.111)–(3.116) and using dots to denote differentiation with respect to t, we obtain the non-dimensionalised system

$$\dot{a}_i^L = -a_i^L b_{i-1}^R + \beta c_i^L + \theta_a(a_i^R - a_i^L) + \omega_a, \tag{3.118}$$

$$\dot{a}_i^R = -a_i^R b_{i+1}^L + \beta c_i^R + \theta_a(a_i^L - a_i^R) + \omega_a, \tag{3.119}$$

$$\dot{b}_i^L = -a_{i-1}^R b_i^L + \beta c_{i-1}^R + \theta_b(b_i^R - b_i^L) + \omega_b, \tag{3.120}$$

$$\dot{b}_i^R = -a_{i+1}^L b_i^R + \beta c_{i+1}^L + \theta_b(b_i^L - b_i^R) + \omega_b, \tag{3.121}$$

$$\dot{c}_i^L = a_i^L b_{i-1}^R - \beta c_i^L - \zeta\mathscr{Q}(c_{i-1}^R)c_i^L, \tag{3.122}$$

$$\dot{c}_i^R = a_i^R b_{i+1}^L - \beta c_i^R - \zeta\mathscr{Q}(c_{i+1}^L)c_i^R. \tag{3.123}$$

3.4.2 Steady state and linear stability analysis

Existence and uniqueness of positive SUSS

We next consider the existence of any positive SUSS (a,b,c) and its linear stability to homogeneous perturbations. We seek positive, homogeneous SUSS solution(s) of the system (3.118)–(3.123). Substituting $a_i^L(t) = a_i^R(t) = a$, $b_i^L(t) = b_i^R(t) = b$, and $c_i^L(t) = c_i^R(t) = c$ into (3.118), (3.120), and (3.122) we find that a, b and c must satisfy

$$-ab + \beta c + \omega_a = 0, \tag{3.124}$$

$$-ab + \beta c + \omega_b = 0, \tag{3.125}$$

$$ab - \beta c - \zeta \mathscr{Q}(c)c = 0. \tag{3.126}$$

Equations (3.124) and (3.125) are incompatible (and thus there exists no SUSS) unless $\omega_a = \omega_b = \omega$. In this case, in the absence of feedback ($\mathscr{Q} = 1$) there is a unique, positive SUSS given by

$$(a,b,c) = \left(a, \frac{\omega(\beta+\zeta)}{\zeta a}, \frac{\omega}{\zeta}\right), \tag{3.127}$$

where a appears to not be unique, but instead determined by the choice of initial condition.

In the presence of feedback, we assume that the higher the concentration of c in one orientation between two neighbouring cells is, the faster the complex of the opposite orientation degrades. This corresponds to $\mathscr{Q} = 1$ being a monotonic increasing function satisfying $\mathscr{Q}(0) = 1$. In this case, any SUSS must satisfy

$$\mathscr{Q}(c) = \frac{\omega}{\zeta c}. \tag{3.128}$$

Since the left-hand side of (3.128) is monotonic increasing from 1, and the right-hand side tends monotonically to ∞ as $c \to 0^+$ and tends monotonically to zero as $c \to \infty$, there must be a unique positive root, and hence a unique positive SUSS.

Linear stability of positive SUSS

We next consider the linear stability of the SUSS under each form of feedback. Similar to the previous two models, we apply (3.41) to the system (3.118)–(3.123), linearise, then apply the change of variables (3.48)–(3.49). This leads to the system

$$\dot{s_a} = -bs_a - as_b + \beta s_c, \tag{3.129}$$

$$\dot{s_b} = -bs_a - as_b + \beta s_c, \tag{3.130}$$

$$\dot{s_c} = bs_a + as_b - \left(\beta + \zeta(\mathscr{Q} + \mathscr{Q}'c)\right) s_c, \tag{3.131}$$

$$\dot{d_a} = -(b + 2\alpha\theta_a)d_a + ad_b + \beta d_c, \tag{3.132}$$

$$\dot{d_b} = bd_a - (a + 2\theta_b)d_b - \beta d_c, \tag{3.133}$$

$$\dot{d_c} = bd_a - ad_b - \left(\beta + \zeta(\mathscr{Q} - \mathscr{Q}'c)\right) d_c. \tag{3.134}$$

We find that the characteristic polynomial $F(\lambda)$ of this system is given by the product of the two polynomials

$$F_s(\lambda) = -\lambda[\lambda^2 + (a + b + \beta + \zeta\mathscr{X})\lambda - \zeta(a+b)\mathscr{X}], \tag{3.135}$$

$$F_d(\lambda) = -\lambda^3 - \beta_2\lambda^2 - \beta_1\lambda - 2\beta_0, \tag{3.136}$$

where

$$\beta_0 = \zeta\mathscr{Y}(a\theta_a + b\theta_b + 2\theta_a\theta_b) + 2\theta_a\theta_b\beta, \tag{3.137}$$

$$\beta_1 = \zeta(a+b)\mathscr{Y} + 2(a\theta_a + b\theta_b) + 2(\theta_a + \theta_b)(\beta + \zeta\mathscr{Y}) + 4\theta_a\theta_b, \tag{3.138}$$

$$\beta_2 = a+b+\beta+2(\theta_a+\theta_b)+\zeta\mathscr{Y}, \tag{3.139}$$

and we have defined $\mathscr{X} := \mathscr{Q}+\mathscr{Q}'c$ and $\mathscr{Y} := \mathscr{Q}-\mathscr{Q}'c$.

The three eigenvalues of (3.135) are $\lambda_1 = 0$ and

$$\lambda_{2,3} = -\frac{1}{2}(a+b+\beta+\zeta\mathscr{X}) \pm \frac{1}{2}\sqrt{(a+b+\beta+\zeta\mathscr{X})^2 - 4\zeta(a+b)\mathscr{X}}. \tag{3.140}$$

Regardless of feedback, we have $\mathscr{X} > 0$, hence all three of these eigenvalues are negative.

In the absence of feedback ($\mathscr{Q} = 1$, hence $\mathscr{X} = \mathscr{Y} = 1$), since the SUSS and all parameters are positive, so are β_0, β_1, β_2. Thus, by applying Descartes' rule of signs, there are no positive roots of (3.136), and there are no positive eigenvalues of the system (3.129)–(3.134). Therefore, the SUSS is linearly stable in respect of spatially homogeneous perturbations in the absence of feedback.

In the presence of feedback, the presence of positive roots of (3.136) can be deduced using Descartes' rule of signs, and depends on $\mathscr{Y}$: (i) if $\mathscr{Y} \geq 0$, then there are no positive roots, hence the SUSS is linearly stable; (ii) if $\mathscr{Y} < 0$, then there is at least one positive root, hence the SUSS is linearly unstable. We verify these analytical results numerically in the next section.

3.4.3 Numerical simulations

In this section we verify our analytical results numerically and conduct a similar numerical investigation to that presented in Section 3.2.3 and Section 3.3.3 for the binding and trafficking feedback models, respectively.

As before, we consider a ring of $N = 30$ cells of equal size, imposing periodic boundary conditions and the initial condition (3.58). Unless stated otherwise, we use the same parameter values as in Section 3.2.3. For our numerical simulations, we must choose a specific

functional form for our feedback function $\mathscr{Q}$. We choose a sigmoidal function of the form

$$\mathscr{Q}(c) = 1 + \frac{(\Pi - 1)c^p}{\tau^p + c^p}, \tag{3.141}$$

where Π is the maximal relative level of feedback in the complex degradation rate, τ denotes the complex concentration at which the feedback effect is half-maximal, and p represents the feedback sharpness.

Polarisation in the presence of degradation feedback

We first verify that the presence of degradation feedback can result in polarisation in this model. Fig. 3.16 shows numerical results for an example parameter set. Note that similar to the trafficking feedback model, and in contrast to the binding feedback model, here the unbound protein concentrations polarise (slightly) as well as the complex concentrations in each cell. A comparison of the time evolution to steady state (Fig. 3.16a) with the previous conservative models (Fig. 3.3a and Fig. 3.10a) suggests that, at least for the parameter sets considered, the degradation feedback model polarises much more quickly. This is due to the diffusion process happening much more rapidly in this model. Note that below, we always assume $\omega_a = \omega_b$ to ensure that a, b, and c all reach steady-state values; simulations with $\omega_a \neq \omega_b$ can exhibit unbounded growth in a or b (results not shown).

Dependence of polarisation on degradation feedback strength and sharpness

Next, we explore whether a certain strength, or sharpness, of degradation feedback is required for polarisation. As for the previous models, we consider a single cell with 'periodic' boundary conditions rather than simulating the full tissue. The upper graphs of Fig. 3.17 show the steady-state values of c^L and c^R for a range of values of feedback strength Π and sharpness p. As with the two previous models, we observe a bifurcation, with the SUSS losing stability at a critical value of Π (Fig. 3.17a) or equivalently of p (Fig. 3.17b). The

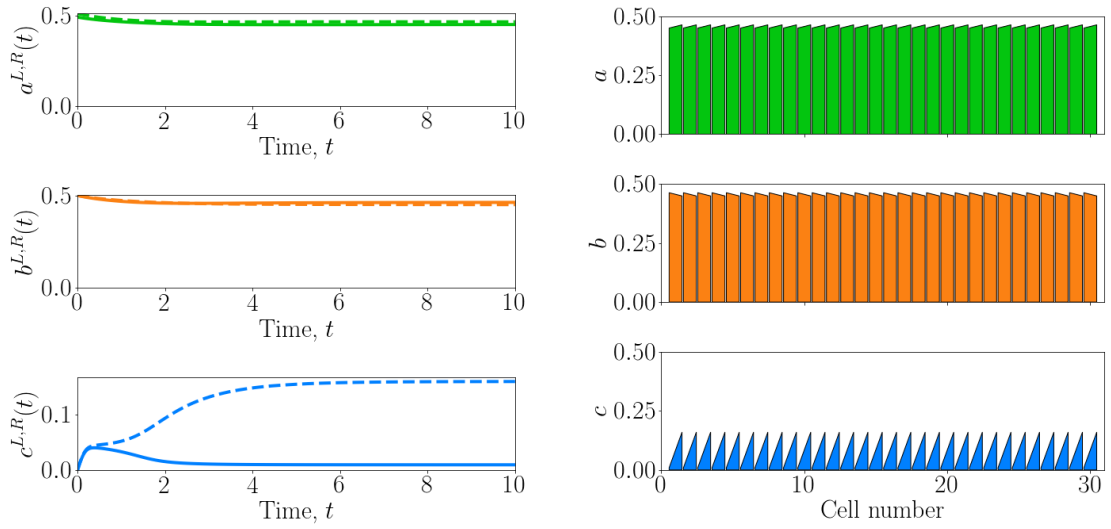

(a) (b)

Fig. 3.16 Numerical solution of the degradation feedback model (3.118)–(3.123) with initial condition (3.58). (a) Solid lines: L; dashed lines: R. (b) Numerical solution shown at $t = 10^5$. Non-dimensional parameter values are $\varepsilon = 0.01$, $\beta = 0.1$, $\zeta = 1$, $\theta_a = 0.1$, $\theta_b = 0.1$, $\omega_a = 0.2$, $\omega_b = 0.2$, $\Pi = 30$, $\tau = 0.1$, $p = 2$.

lower graphs of Fig. 3.17 show that above these critical values, the term $\mathscr{Y}$ defined in our linear stability analysis does indeed become negative.

Clone phenotypes

We next investigate the behaviour of cells neighbouring a group of cells in which the abundance of each protein is perturbed. However unlike the two previous models, we cannot implement single and double clones as described in Section 3.2.3, since the total protein concentration in each cell is not conserved over time. One possibility is to alter the *initial* total concentrations of a and/or b in each mutant cell; however as one might expect, this does not lead to any effect on the surrounding cells in our simulations (results not shown). Therefore, we instead simulate mutant clones assume either through lower production rates (Fig. 3.18) or higher production rates (Fig. 3.19) than normal cells, implemented through varying the parameters ω_a and/or ω_b. Biologically, this arguably provides a more realistic description

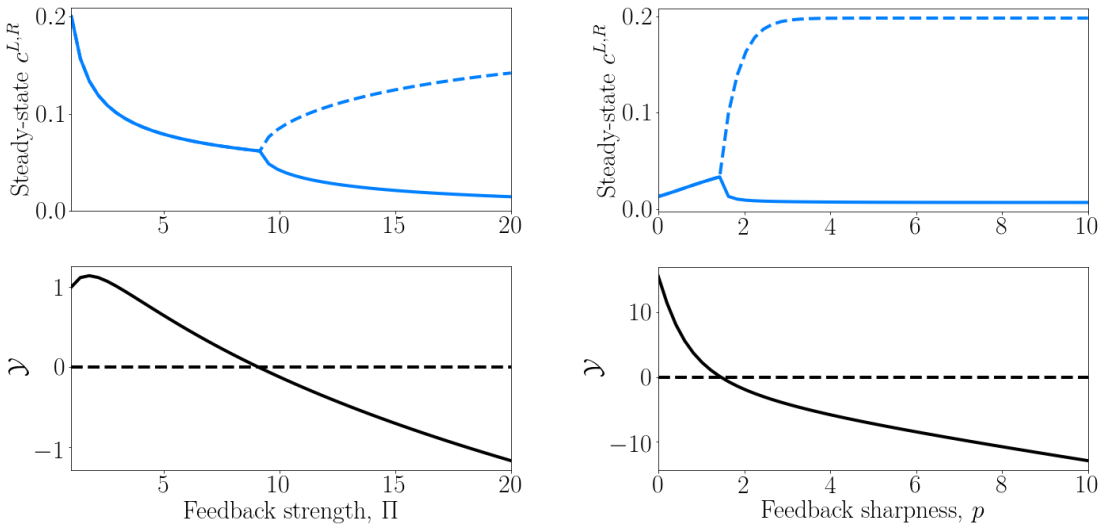

(a) (b)

Fig. 3.17 Bifurcation analysis of the degradation feedback model (3.118)–(3.123) with respect to feedback (a) strength and (b) sharpness. Non-dimensional parameter values are $\varepsilon = 0.01$, $\beta = 0.1$, $\zeta = 1$, $\theta_a = 0.1$, $\theta_b = 0.1$, $\omega_a = 0.2$, $\omega_b = 0.2$, $\Pi = 30$, $\tau = 0.1$, $p = 2$. Solid lines: L; dashed lines: R (upper panels).

of under- or overexpression within mutant cells. Fig. 3.18 and Fig. 3.19 show the results of sets of example simulations demonstrating perturbed polarisation in cells surrounding single and double clones in the cases of underexpression (Fig. 3.18) and overexpression (Fig. 3.19), respectively. In the single clone simulations, the protein concentration a tends to a very low steady state if its production rate is low (Fig. 3.18a). However, if its production rate is high, then a becomes unbounded (Fig. 3.19a). Single b^- clones show similar results to single a^- clones (results not shown).

Counter-intuitively, despite c polarising (mostly) correctly around double a^-b^- clones, we find unpolarised period two patterns in the concentrations of a and b, regardless of whether the clone exhibits underexpression (Fig. 3.18b) or overexpression (Fig. 3.19b). We note that similar period two patterns have been observed in another abstracted planar polarity model by Schamberg et al. [69], as alluded to earlier.

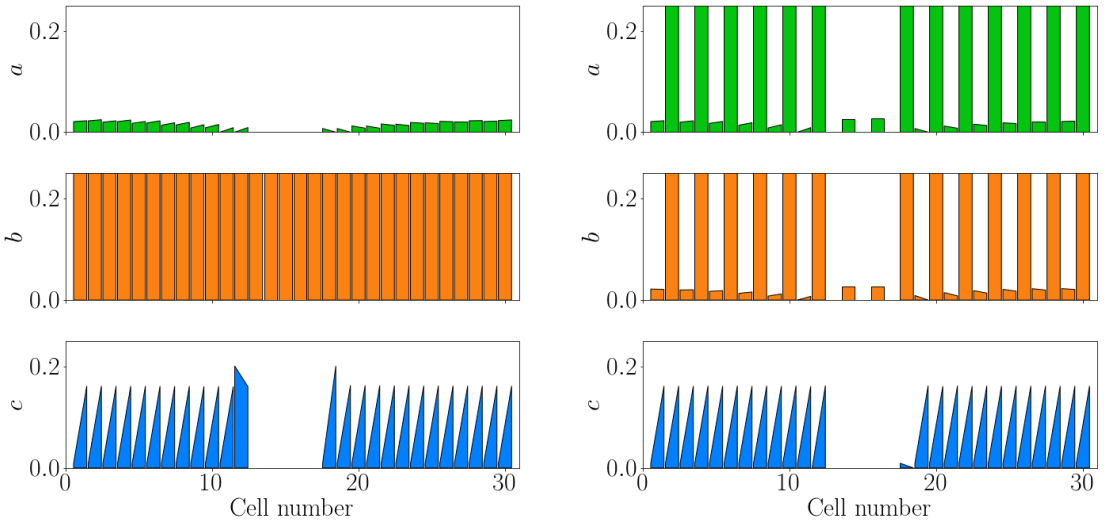

(a) (b)

Fig. 3.18 Perturbed polarisation in the degradation feedback model (3.118)–(3.123) for cells neighbouring (a) a single a^- clone and (b) a double a^-b^- clone. Non-dimensional parameter values are $\varepsilon = 0.01$, $\beta = 0.1$, $\zeta = 1$, $\theta_a = 0.1$, $\theta_b = 0.1$, $\omega_a = 0.2 = \omega_b = 0.2$, $\Pi = 30$, $\tau = 0.1$, $p = 2$. Within clones, $a(0) = b(0) = 0.1$ and $\omega_a = \omega_b = 0$. Numerical solutions shown at $t = 10^5$.

Fig. 3.20 illustrates how the range of non-autonomy (if it occurs) varies with feedback strength in this model, in the case of underexpression (Fig. 3.20a) and overexpression (Fig. 3.20b), respectively. We find that for a single a^- clone, maximum disruption is observed for an intermediate value of the feedback strength, whose value is the same for ($\Pi \approx 12$) regardless of under- or overexpression. This is largely abolished for double a^-b^- clones. Indeed, in contrast to clone simulations in the two previous (mass conserved) models, we do not observe any domineering non-autonomy for a wide variety of feedback strengths (Fig. 3.20). This could be explained by the absence of a travelling wave propagating away from the clone edges as there appeared to be in the previous mass conserved model simulations.

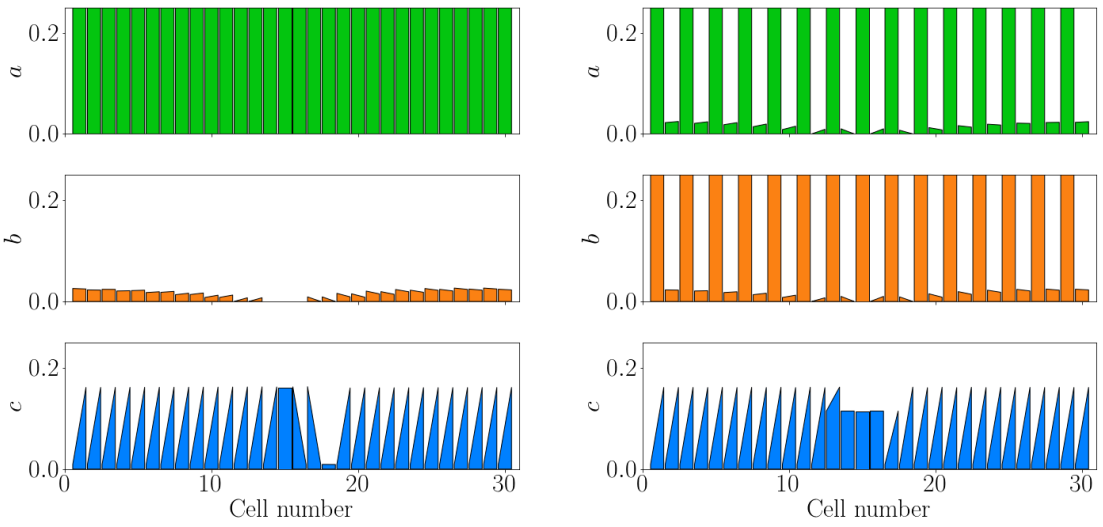

(a) (b)

Fig. 3.19 Perturbed polarisation in the degradation feedback model (3.118)–(3.123) for cells neighbouring (a) a single a^+ clone and (b) a double a^+b^+ clone. Non-dimensional parameter values are $\varepsilon = 0.01$, $\beta = 0.1$, $\zeta = 1$, $\theta_a = 0.1$, $\theta_b = 0.1$, $\omega_a = 0.2 = \omega_b = 0.2$, $\Pi = 30$, $\tau = 0.1$, $p = 2$. Within clones $a(0) = b(0) = 0.1$ and $\omega_a = \omega_b = 2$. Numerical solutions shown at $t = 10^5$.

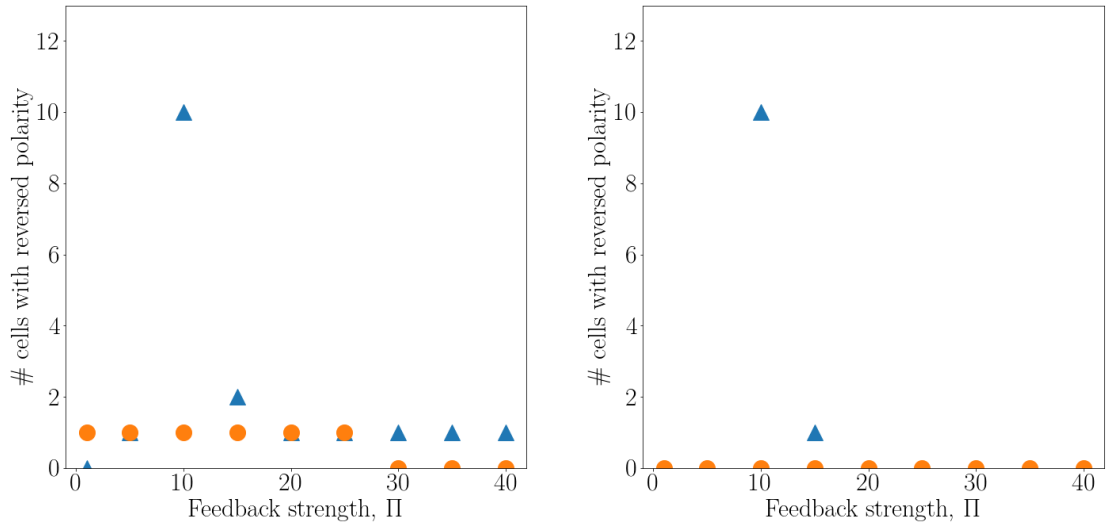

(a) (b)

Fig. 3.20 Range of domineering non-autonomy in the degradation feedback model for clones exhibiting (a) underexpression and (b) overexpression. Blue triangles: a^- clone; orange circles: a^-b^- clone. Non-dimensional parameter values are $\varepsilon = 0.01$, $\beta = 0.1$, $\zeta = 1$, $\theta_a = 0.1$, $\theta_b = 0.1$, $\omega_a = 0.2 = \omega_b = 0.2$, $\Pi = 30$, $\tau = 0.1$, $p = 2$. Within clones $a(0) = b(0) = 0.1$, with (a) $\omega_a = \omega_b = 0$, and (b) $\omega_a = \omega_b = 2$. Numerical solutions shown at $t = 10^5$.

Taken together, these results suggest that if feedback interactions were to operate by modulating protein complex degradation rates within each cell, then we would not expect to see domineering non-autonomy around double clones, but may expect to see counter-intuitive period two patterns in unbound protein concentrations. As with the previous two models considered in this chapter, these theoretical results have potential implications for how to interpret experimental observations of mutant clone phenotypes in the core planar polarity pathway.

3.5 Discussion

In this chapter we have considered a variety of different possible feedback mechanisms that could underlie the amplification of initial asymmetries and drive a tissue to a planar polarised state. For each model, we have shown the presence of a bifurcation whereby a positive SUSS loses stability to homogeneous perturbations, but only given sufficiently strong or sharp feedback.

While sharing many similarities, the three forms of feedback can lead to qualitatively different behaviours in cells neighbouring mutant clones, with domineering non-autonomy observed in simulations of both single and double clones in some cases, and only single clones in other cases. We also found some counter-intuitive behaviours such as period two patterns in unbound protein concentrations.

We have deliberately adopted a minimal modelling approach in this chapter, rather than seeking to construct a detailed biochemical model of a particular planar polarity pathway, in order to explore the generic features of and requirements for amplifying feedback interactions. One particular abstraction in our model, which is worth discussing further in the context of the literature, is our treatment of the initial asymmetry or 'bias' in one unbound protein concentration within each cell. Generally speaking, such a bias could arise as an 'internal' mechanism, whereby planar polarity proteins are expressed as a gradient and themselves

instruct local polarity; alternatively, an 'external' mechanism could operate, whereby the bias comes from an external source to the system [74].

In the case of the core pathway, candidates for an external mechanism include secreted Wnt ligands, which have long been hypothesised to act as a global cue for planar polarisation in many developing tissues. In the fly wing for instance, trichomes along the wing margin point toward the source of Wnts [75]. Although overexpression of Wnt signalling ectopically results in trichomes reorientation [75], it is difficult to demonstrate the instructive role of Wnts in trichome orientation during wing development using loss-of-function mutations (reviewed by Aw and Devenport [19] and Harrison et al. [76]).

The Ft-Ds pathway has also been considered to be an upstream global cue for the core pathway, either via direct interaction [77], or by biasing the apical microtubule cytoskeleton [78]. However, the Ft-Ds pathway mostly affects hair polarity away from the wing margin [78], suggesting the existence of other potential mechanisms or additional signals that generate the global cue; these could include mechanical forces [46].

Work has also been done to determine whether such a bias or cue can be transient, or must be persistent, over the timescale of polarisation. For example, a model by Fischer et al. [71] suggests that while polarisation can be generated using only a transient initial cue, such cues are not enough to ensure the *robustness* of the resulting polarity.

Finally, we note that in the absence of feedback, the presence of a clone can still results in weak tissue-scale polarity in our model, even if the bias in the initial condition (3.58) is removed (results not shown). This suggests that clones can impose polarity and could work as another resource of bias within the system (see Fig. 3.9, in the case that η and μ are 1).

It is important to emphasise that we restricted our analysis in this chapter to one spatial dimension. In the next chapter, we extend this work to two spatial dimensions.

Chapter 4

Moving from one to two spatial dimensions

4.1 Introduction

As discussed in Chapter 3, previous theoretical modelling of the core planar polarity pathway has highlighted the importance of studying the mechanisms underlying tissue-scale polarity coordination. Models that approximate a tissue by a one-dimensional line of cells, in Chapter 3, are generally more amenable to mathematical analysis. However, it is also instructive to consider the richer variety of behaviours of types of patterning that may arise in two spatial dimensions.

Planar polarity models that include two-dimensional geometries vary in terms of biological detail, ranging from those that are generic and abstract to those that consider a large number of detailed biochemical interactions. An example of the former approach is the work of Schamberg [79], who proposes an abstract model based on juxtacrine signalling in an array of square cells to gain a broad understanding of planar polarisation requirements. The author concludes that uniform initial conditions can lead to a polarised state in the case of a

strong feedback and weak diffusion. However, it is difficult to relate this model directly to protein/complex concentrations and specific biological systems.

More biologically detailed models include the works of Amonlirdviman et al. [38] and Le Garrec et al. [65], who examine the roles of protein-protein interactions and global cues in planar polarisation within the fly wing. Both studies show that intercellular interactions of the key core regulators Fz, Dsh, Vang, and Pk can recapitulate experimentally observed asymmetric localisation of these proteins. Although the two models by Amonlirdviman et al. [38] and Le Garrec et al. [65] differ in the details of those interactions, the proposed mechanisms in both cases consist of a persistent global cue and an inhibition feedback loop, with both components required for polarisation.

Returning to less biochemically detailed modelling, detailed mathematical analysis by Fischer et al. [71] in one and two spatial domains suggests that a global cue and positive feedback mechanisms are both necessary for polarisation to occur. These authors explore the requirements for which the two models by Amonlirdviman et al. [38] and Le Garrec et al. [65] should generate polarisation in a single hexagonal cell. They find that depending on the feedback strength and the intercellular diffusion, both models yield a stable 'side' polarised steady state or a 'triangular' polarised steady state; whereas the 'vertex 'polarised state is never robust to asymmetric perturbations in the initial condition (see Section 4.3 for a detailed definition of these different steady states). However, it is unclear whether our own modelling presented in Chapter 3 should yield the same qualitative results in 2D, in particular regarding the lack of stability of a 'vertex' steady state.

4.1.1 Aim of work

In this chapter, we extend the planar polarity modelling work presented in Chapter 3 to explore the feedback requirements for planar polarity in two spatial dimensions. We also consider the stability of alternative forms of polarity, corresponding to different symmetries,

in the presence or absence of feedback interactions. In addition, we investigate the behaviour of cells neighbouring mutant clones in two spatial dimensions in our simulations, and relate these to experimental observations and to previous modelling predictions as discussed above. For simplicity, we restrict our focus to the 'binding feedback' model introduced in Chapter 3, whereby feedback interactions amplify asymmetries through locally affecting the stability of protein complexes of the same, or opposite, orientation.

The remainder of this chapter is structured as follows. In Section 4.2 we introduce the model and governing equations. In Section 4.3, using steady state and linear stability analysis, we explore what other types of polarisation the model yields in the case of different (a)symmetric initial assumptions. In Section 4.4 we present the results of numerical simulations of the model for both a single 'periodic' cell and for sheet of cells. We conclude in Section 4.5 with a discussion of our results and how their implications for understanding tissue-scale polarisation.

4.2 Governing equations

We consider a simplified planar polarity system operating in a doubly-periodic two-dimensional sheet of $M \times N$ hexagonal cells (see Fig. 4.1). A motivating example for choosing hexagonal cells is the surface of the developing fly wing, which comprises an array of cells that are packed hexagonally immediately prior to trichome formation (i.e. during the timescale of core pathway planar polarisation in this tissue) [80]. Two proteins A and B are allowed to bind reversibly across neighbouring cells to form an intercellular complex C according to the set of reversible reactions

$$A^m_{i,j} + B^{m+3}_{i_m,j_m} \rightleftharpoons C^m_{i,j}, \tag{4.1}$$

where the subscript indices (i_m, j_m) transform (i, j) to neighbouring indices in a way that depends on the value of m, as follows:

$$(i_m, j_m) = \begin{cases} (i, j+1) & \text{if } m = 0, \\ (i+1, j+(i+1) \bmod 2) & \text{if } m = 1, \\ (i+1, j-i \bmod 2) & \text{if } m = 2, \\ (i, j-1) & \text{if } m = 3, \\ (i-1, j-i \bmod 2) & \text{if } m = 4, \\ (i-1, j+(i+1) \bmod 2) & \text{if } m = 5. \end{cases} \tag{4.2}$$

Proteins A and B are also allowed to diffuse between neighbouring sides of each cell according to the 'reactions'

$$A^m_{i,j} \rightleftharpoons A^{m\pm1}_{i,j}, \tag{4.3}$$

$$B^m_{i,j} \rightleftharpoons B^{m\pm1}_{i,j}. \tag{4.4}$$

Here subscripts $i \in \{0, \ldots, M-1\}$ and $j \in \{0, \ldots, N-1\}$ refer to the relevant protein in the cell occupying the ith column and jth row, modulo N, starting from the top left (Fig. 4.1), while superscript $m \in \{0, \ldots, 5\}$ refers to the mth edge of the cell going clockwise from the top; we emphasise that superscript indices are understood to be taken mod 6.

We assume that each of the reactions (4.1) proceeds with a forward rate coefficient k and backward rate coefficient v. We also assume in reactions (4.3) and (4.3) that A and B diffuse between cell compartments with diffusion coefficients D_A and D_B, respectively. Diffusion is assumed to take place between the present side and the two adjacent sides of the same cell. For consistency of analysis, we write $k = k_0\mathscr{K}$ and $v = v_0\mathscr{V}$, where k_0 and v_0 denote baseline values for the forward and backward rate constants (as in the 1D model). We assume

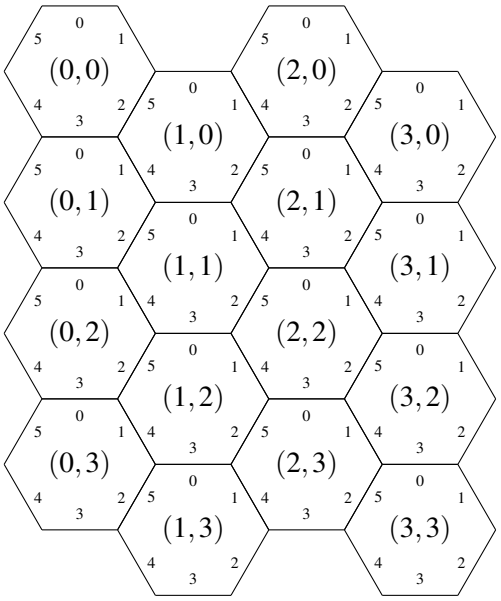

Fig. 4.1 Schematic of the cell and side numbering convention used in equations (4.1)–(4.4).

throughout that D_A and D_B are constant, while v and k may dependent on the local complex concentration (see below).

Let $A^m_{i,j}(T)$, $B^m_{i,j}(T)$ and $C^m_{i,j}(T)$ denote the concentrations of molecules A, B and C on the mth side of cell (i, j) at time T. Using the Law of Mass Action, reactions (4.1)–(4.4) may be converted into the ODE system

$$\frac{dA^m_{i,j}}{dT} = -k_0 \mathscr{K}(C^m_{i,j}) A^m_{i,j} B^{m+3}_{i_m,j_m} + v_0 \mathscr{V}(C^{m+3}_{i_m,j_m}) C^m_{i,j} + D_A (A^{m-1}_{i,j} - 2A^m_{i,j} + A^{m+1}_{i,j}), \tag{4.5}$$

$$\frac{dB^m_{i,j}}{dT} = -k_0 \mathscr{K}(C^{m+3}_{i_m,j_m}) A^{m+3}_{i_m,j_m} B^m_{i,j} + v_0 \mathscr{V}(C^m_{i,j}) C^{m+3}_{i_m,j_m} + D_B (B^{m-1}_{i,j} - 2B^m_{i,j} + B^{m+1}_{i,j}), \tag{4.6}$$

$$\frac{dC^m_{i,j}}{dT} = k_0 \mathscr{K}(C^m_{i,j}) A^m_{i,j} B^{m+3}_{i_m,j_m} - v_0 \mathscr{V}(C^{m+3}_{i_m,j_m}) C^m_{i,j}, \tag{4.7}$$

for $i \in \{0,\ldots,M-1\}$, $j \in \{0,\ldots,N-1\}$, and $m \in \{0,\ldots,5\}$. From (4.5)–(4.7), we see that the total (bound and unbound) concentrations of A and B

$$A_{\text{tot}} = \sum_{m=0}^{5} \left(A^m_{i,j} + C^m_{i,j} \right), \tag{4.8}$$

$$B_{\text{tot}} = \sum_{m=0}^{5} \left(B_{i,j}^{m} + C_{i_m, j_m}^{m+3} \right) \tag{4.9}$$

are conserved in each cell, with their values determined by the initial condition (see below).

To non-dimensionalise this model, we let $T = T_0 t$ and $A_{i,j}^{m} = A_{\text{tot}} a_{i,j}^{m}$, $B_{i,j}^{m} = B_{\text{tot}} b_{i,j}^{m}$ and $C_{i,j}^{m} = A_{\text{tot}} c_{i,j}^{m}$ for $i \in \{0, \ldots, M-1\}$, $j \in \{0, \ldots, N-1\}$, and $m \in \{0, \ldots, 5\}$, where $a_{i,j}^{m}$, $b_{i,j}^{m}$, $c_{i,j}^{m}$ and t denote dimensionless variables. Finally, we choose $T_0 = 1/k_0 A_{\text{tot}}$ and define dimensionless lumped parameters

$$\nu = \frac{v_0}{k_0 A_{\text{tot}}}, \qquad \gamma = \frac{B_{\text{tot}}}{A_{\text{tot}}}, \qquad \delta = \frac{D_A}{k_0 A_{\text{tot}}}, \qquad \sigma = \frac{D_B}{D_A}. \tag{4.10}$$

Substituting into (4.5)–(4.7), we obtain the non-dimensionalised system

$$\dot{a}_{i,j}^{m} = -\gamma \mathscr{K}(c_{i,j}^{m}) a_{i,j}^{m} b_{i_m, j_m}^{m+3} + \nu \mathscr{V}(c_{i_m, j_m}^{m+3}) c_{i,j}^{m} + \delta (a_{i,j}^{m-1} - 2a_{i,j}^{m} + a_{i,j}^{m+1}), \tag{4.11}$$

$$\dot{b}_{i,j}^{m} = -\mathscr{K}(c_{i_m, j_m}^{m+3}) a_{i_m, j_m}^{m+3} b_{i,j}^{m} + \frac{\nu}{\gamma} \mathscr{V}(c_{i,j}^{m}) c_{i_m, j_m}^{m+3} + \sigma\delta (b_{i,j}^{m-1} - 2b_{i,j}^{m} + b_{i,j}^{m+1}), \tag{4.12}$$

$$\dot{c}_{i,j}^{m} = \gamma \mathscr{K}(c_{i,j}^{m}) a_{i,j}^{m} b_{i_m, j_m}^{m+3} - \nu \mathscr{V}(c_{i_m, j_m}^{m+3}) c_{i,j}^{m}, \tag{4.13}$$

for $m \in \{0, \ldots, 5\}$, where dots denote derivatives with respect to t, with non-dimensionalised conservation laws

$$1 = \sum_{m=0}^{5} \left(a_{i,j}^{m} + c_{i,j}^{m} \right), \tag{4.14}$$

$$\gamma = \sum_{m=0}^{5} \gamma b_{i,j}^{m} + c_{i_m, j_m}^{m+3}. \tag{4.15}$$

4.3 Existence and stability of planar polarity and other patterns

Next, we aim to gain insight into the possible steady states of the system. In a two-dimensional tissue with hexagonal cells, steady states of (4.11)–(4.13) can potentially exhibit a variety of symmetries, including 'vertex' state, 'triangular' or 'side' polarity state [71], which we will discuss in more detail later in this chapter (see Fig. 4.2). In addition to planar polarity, vertex polarity is arguably most biologically relevant, since the wild-type fly wing is covered with hexagonal cells each with a distal pointing hair.

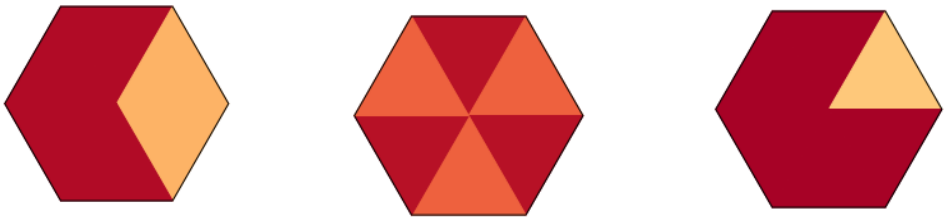

(a) Vertex polarity. (b) Triangular polarity. (c) Side polarity.

Fig. 4.2 Schematic showing the different types of steady state in two spatial dimensions.

For simplicity, in the following we consider only *homogeneous* steady states and perturbations, where

$$a^m_{i,j}(t) \equiv a^m(t), \qquad b^m_{i,j}(t) \equiv b^m(t), \qquad c^m_{i,j}(t) \equiv c^m(t), \tag{4.16}$$

for all i, j. However, we allow spatially *non-uniform* steady states, for which $a^m(t) \not\equiv a^n(t)$, $b^m(t) \not\equiv b^n(t)$ and $c^m(t) \not\equiv c^n(t)$. Equations (4.11)–(4.13) therefore simplify to

$$\dot{a}^m = -\gamma \mathscr{K}(c^m) a^m b^{m+3} + \nu \mathscr{V}(c^{m+3}) c^m + \delta(a^{m-1} - 2a^m + a^{m+1}), \tag{4.17}$$

$$\dot{b}^m = -\mathscr{K}(c^{m+3}) a^{m+3} b^m + \frac{\nu}{\gamma} \mathscr{V}(c^m) c^{m+3} + \sigma\delta(b^{m-1} - 2b^m + b^{m+1}), \tag{4.18}$$

$$\dot{c}^m = \gamma \mathscr{K}(c^m) a^m b^{m+3} - \nu \mathscr{V}(c^{m+3}) c^m, \tag{4.19}$$

for $m \in \{0,\ldots,5\}$, where dots denote derivatives with respect to t as before, and we hence have the non-dimensionalised conservation laws

$$1 = \sum_{m=0}^{5} (a^m + c^m), \tag{4.20}$$

$$\gamma = \sum_{m=0}^{5} (\gamma b^m + c^m). \tag{4.21}$$

4.3.1 Existence and uniqueness of positive SUSS

Any positive SUSS of (4.17)–(4.19), such that $a^m \equiv a$, $b^m \equiv b$ and $c^m \equiv c$, must satisfy

$$-\gamma \mathscr{K}(c) ab + \nu \mathscr{V}(c) c = 0, \tag{4.22}$$

$$6a + 6c = 1, \tag{4.23}$$

$$6\gamma b + 6c = \gamma. \tag{4.24}$$

In the absence of feedback ($\mathscr{K} = \mathscr{V} = 1$), equations (4.22)–(4.24) reduce to

$$6a^2 + (\gamma + 6\nu - 1)a - \nu = 0. \tag{4.25}$$

Regardless of the sign of $\gamma + 6\nu - 1$, we see that (4.25) always has a unique positive root, that is given by

$$a = \frac{1}{12}\left(1 - \gamma - 6\nu + \sqrt{(\gamma + 6\nu - 1)^2 + 24\nu}\right), \tag{4.26}$$

with corresponding values

$$b = \frac{1}{12\gamma}\left(\gamma - 1 - 6\nu + \sqrt{(\gamma+6\nu-1)^2+24\nu}\right), \tag{4.27}$$

$$c = \frac{1}{12}\left(1 + \gamma + 6\nu - \sqrt{(\gamma+6\nu-1)^2+24\nu}\right). \tag{4.28}$$

Thus, in the absence of feedback, there is a unique positive SUSS. In the presence of feedback, however, any SUSS satisfies

$$36\nu\mathscr{V}(c)c = \mathscr{K}(c)(1-6c)(\gamma-6c). \tag{4.29}$$

Since analysing the existence of the steady state in this case is complex, we resort to a numerical investigation in Section 4.4. We next explore the existence and uniqueness of three other possible homogeneous steady states of (4.17)–(4.19), each with a different symmetry.

4.3.2 Existence and uniqueness of 'side' steady state

We first consider any steady state of the form

$$(a^5(t),b^5(t),c^5(t)) = (a^0(t),b^0(t),c^0(t)) = (a^1(t),b^1(t),c^1(t)) = (a^U,b^U,c^U), \tag{4.30}$$

$$(a^2(t),b^2(t),c^2(t)) = (a^3(t),b^3(t),c^3(t)) = (a^4(t),b^4(t),c^4(t)) = (a^D,b^D,c^D). \tag{4.31}$$

Any such steady state must satisfy

$$0 = -\gamma\mathscr{K}(c^U)a^Ub^D + \nu\mathscr{V}(c^D)c^U + \delta(a^D-a^U), \tag{4.32}$$

$$0 = -\gamma\mathscr{K}(c^D)a^Db^U + \nu\mathscr{V}(c^U)c^D + \delta(a^U-a^D), \tag{4.33}$$

$$0 = -\mathscr{K}(c^D)a^Db^U + \frac{\nu}{\gamma}\mathscr{V}(c^U)c^D + \sigma\delta(b^D-b^U), \tag{4.34}$$

$$0 = -\mathscr{K}(c^U)a^Ub^D + \frac{\nu}{\gamma}\mathscr{V}(c^D)c^U + \sigma\delta(b^U-b^D), \tag{4.35}$$

$$0 = \gamma\mathscr{K}(c^U)a^U b^D - \nu\mathscr{V}(c^D)c^U, \tag{4.36}$$

$$0 = \gamma\mathscr{K}(c^D)a^D b^U - \nu\mathscr{V}(c^U)c^D, \tag{4.37}$$

with conservation laws

$$3a^U + 3a^D + 3c^U + 3c^D = 1, \tag{4.38}$$

$$3\gamma b^U + 3\gamma b^D + 3c^U + 3c^D = \gamma. \tag{4.39}$$

From (4.32)–(4.35) and due to diffusion, we deduce that $a^U \equiv a^D \equiv a$ and $b^U \equiv b^D \equiv b$. Therefore, the steady state must satisfy

$$0 = \gamma\mathscr{K}(c^U)ab - \nu\mathscr{V}(c^D)c^U, \tag{4.40}$$

$$0 = \gamma\mathscr{K}(c^D)ab - \nu\mathscr{V}(c^U)c^D,, \tag{4.41}$$

$$1 = 6a + 3c^D, \tag{4.42}$$

$$\gamma = 6\gamma b + 3c^U + 3c^D. \tag{4.43}$$

In the absence of feedback ($\mathscr{K} = \mathscr{V} = 1$), equations (4.41)–(4.43) have a unique solution, which corresponds to the SUSS ($c^U \equiv c^D \equiv c$). We explore numerically whether any other solution exists in the presence of feedback in Section 4.4.

4.3.3 Existence and uniqueness of 'triangular' steady state

Next, we consider any steady state of the form

$$(a^0(t), b^0(t), c^0(t)) = (a^2(t), b^2(t), c^2(t)) = (a^4(t), b^4(t), c^4(t)) = (a^T, b^T, c^T), \tag{4.44}$$

$$(a^1(t), b^1(t), c^1(t)) = (a^3(t), b^3(t), c^3(t)) = (a^5(t), b^5(t), c^5(t)) = (a^S, b^S, c^S). \tag{4.45}$$

Any such steady state must satisfy

$$0 = -\gamma\mathscr{K}(c^T)a^T b^S + \nu\mathscr{V}(c^S)c^T + 2\delta(a^S - a^T), \tag{4.46}$$

$$0 = -\gamma\mathscr{K}(c^S)a^S b^T + \nu\mathscr{V}(c^T)c^S + 2\delta(a^T - a^S), \tag{4.47}$$

$$0 = -\mathscr{K}(c^S)a^S b^T + \frac{\nu}{\gamma}\mathscr{V}(c^T)c^S + 2\sigma\delta(b^S - b^T), \tag{4.48}$$

$$0 = -\mathscr{K}(c^T)a^T b^S + \frac{\nu}{\gamma}\mathscr{V}(c^S)c^T + 2\sigma\delta(b^T - b^S), \tag{4.49}$$

$$0 = \gamma\mathscr{K}(c^T)a^T b^S - \nu\mathscr{V}(c^S)c^T, \tag{4.50}$$

$$0 = \gamma\mathscr{K}(c^S)a^S b^T - \nu\mathscr{V}(c^T)c^S, \tag{4.51}$$

with conservation laws

$$3a^T + 3a^S + 3c^T + 3c^S = 1, \tag{4.52}$$

$$3\gamma b^T + 3\gamma b^S + 3c^T + 3c^S = \gamma. \tag{4.53}$$

Following the same line of argument as the previous case, any solution of (4.46)–(4.51) should satisfy

$$\gamma\left(\frac{1}{6} - \frac{1}{2}(c^T + c^S)\right)\left(\frac{1}{6} - \frac{1}{2\gamma}(c^T + c^S)\right)\left(\mathscr{K}(c^T) + \mathscr{K}(c^S)\right) = \nu\left(\mathscr{V}(c^T)c^S + \mathscr{V}(c^T)c^S\right). \tag{4.54}$$

In the absence of feedback ($\mathscr{K} = \mathscr{V} = 1$), the only solution of the system (4.46)–(4.51) is the homogeneous unpolarised solution where $c^T \equiv c^S$. In the case of feedback, we investigate the existence of such a solution numerically in Section 4.4.

4.3.4 Existence and uniqueness of 'vertex' steady state

We next consider a vertex-like steady state where the concentrations of each species in the top and bottom compartments of each cell is equal, while the concentration in the right and left compartments is different:

$$(a^0(t), b^0(t), c^0(t)) = (a^3(t), b^3(t), c^3(t)) = (\bar{a}, \bar{b}, \bar{c}), \tag{4.55}$$

$$(a^4(t), b^4(t), c^4(t)) = (a^5(t), b^5(t), c^5(t)) = (a^L, b^L, c^L), \tag{4.56}$$

$$(a^1(t), b^1(t), c^1(t)) = (a^2(t), b^2(t), c^2(t)) = (a^R, b^R, c^R). \tag{4.57}$$

Any such steady state must satisfy

$$0 = -\gamma\mathscr{K}(\bar{c})\bar{a}\bar{b} + \nu\mathscr{V}(\bar{c})\bar{c} + \delta(a^L - 2\bar{a} + a^R), \tag{4.58}$$

$$0 = -\gamma\mathscr{K}(c^R)a^R b^L + \nu\mathscr{V}(c^L)c^R + \delta(\bar{a} - a^R), \tag{4.59}$$

$$0 = -\gamma\mathscr{K}(c^L)a^L b^R + \nu\mathscr{V}(c^R)c^L + \delta(\bar{a} - a^L), \tag{4.60}$$

$$0 = -\mathscr{K}(\bar{c})\bar{a}\bar{b} + \frac{\nu}{\gamma}\mathscr{V}(\bar{c})\bar{c} + \sigma\delta(b^L - 2\bar{b} + b^R), \tag{4.61}$$

$$0 = -\mathscr{K}(c^L)a^L b^R + \frac{\nu}{\gamma}\mathscr{V}(c^R)c^L + \sigma\delta(\bar{b} - b^R), \tag{4.62}$$

$$0 = -\mathscr{K}(c^R)a^R b^L + \frac{\nu}{\gamma}\mathscr{V}(c^L)c^R + \sigma\delta(\bar{b} - b^L), \tag{4.63}$$

$$0 = \gamma\mathscr{K}(\bar{c})\bar{a}\bar{b} - \nu\mathscr{V}(\bar{c})\bar{c}, \tag{4.64}$$

$$0 = \gamma\mathscr{K}(c^R)a^R b^L - \nu\mathscr{V}(c^L)c^R, \tag{4.65}$$

$$0 = \gamma\mathscr{K}(c^L)a^L b^R - \nu\mathscr{V}(c^R)c^L, \tag{4.66}$$

with conservation laws

$$2\bar{a} + 2a^L + 2a^R + 2\bar{c} + 2c^L + 2c^R = 1, \tag{4.67}$$

$$2\gamma\bar{b} + 2\gamma b^L + 2\gamma b^R + 2\bar{c} + 2c^L + 2c^R = \gamma. \tag{4.68}$$

From (4.58)–(4.63), we see that $\bar{a} \equiv a^L \equiv a^R \equiv a$ and $\bar{b} \equiv b^L \equiv b^R \equiv b$. Hence, any such steady state must satisfy

$$0 = \gamma \mathscr{K}(\bar{c}) ab - \nu \mathscr{V}(\bar{c}) \bar{c}, \tag{4.69}$$

$$0 = \gamma \mathscr{K}(c^R) ab - \nu \mathscr{V}(c^L) c^R, \tag{4.70}$$

$$0 = \gamma \mathscr{K}(c^L) ab - \nu \mathscr{V}(c^r) c^L. \tag{4.71}$$

Applying (4.67) and (4.68) yields

$$\begin{aligned} &\gamma \left(\frac{1}{6} - \frac{1}{3}(\bar{c} + c^R + c^L) \right) \left(\frac{1}{6} - \frac{1}{3\gamma}(\bar{c} + c^R + c^L) \right) \left(\mathscr{K}(\bar{c}) + \mathscr{K}(c^R) + \mathscr{K}(c^L) \right) \\ &\qquad = \nu \left(\mathscr{V}(\bar{c}) \bar{c} + \mathscr{V}(c^R) c^L + \mathscr{V}(c^R) c^L \right). \end{aligned} \tag{4.72}$$

In the absence of feedback ($\mathscr{K} = \mathscr{V} = 1$), the only solution to (4.72) is the homogeneous unpolarised solution where $\bar{c} \equiv c^R \equiv c^L$. Again, in the case of feedback we numerically investigate the existence of such a solution in Section 4.4.

In summary, the homogeneous unpolarised steady state, where the concentrations of each protein is equal in all compartments, always exists in the case of no feedback. In the next section we use numerical simulations to investigate the linear stability of the various steady states considered in this section in the presence or absence of feedback.

4.4 Numerical simulations

As in the model discussed in Chapter 3, we choose the following functional forms for the cases of destabilising and stabilising feedback, respectively:

$$\mathscr{V}(c) = 1 + \frac{(\eta - 1) c^n}{\kappa^n + c^n}, \tag{4.73}$$

$$\mathscr{K}(c) = 1 + \frac{(\mu - 1)c^m}{\rho^m + c^m}, \tag{4.74}$$

where η and μ denote the maximal relative levels of destabilising and stabilising feedback, κ and ρ denote the concentrations at which the corresponding feedback is half-maximal, and n and m represent the feedback sharpness. Throughout this section, we use a standard set of parameter values unless stated otherwise; these are listed in Table 4.1.

Parameter	**Destabilising feedback**	**Stabilising feedback**
Feedback strength	$\eta = 50$	$\mu = 150$
Concentration at which feedback is half-maximal	$\kappa = 0.1$	$\rho = 1$
Feedback sharpness	$n = 2$	$m = 2$
Binding affinity (v_0/k_0A_{tot})	$\nu = 0.1$	
Ratio of total concentrations ($B_{\text{tot}}/A_{\text{tot}}$)	$\gamma = 1$	
D_A/k_0A_{tot}	$\delta = 0.01$	
Ratio of diffusion coefficients (D_B/D_A)	$\sigma = 1$	
Global cue (bias)	$\varepsilon = 0.01$	

Table 4.1 Set of parameter values used for the numerical simulations presented in this section.

4.4.1 Numerical simulations for a single hexagonal cell

We first simulate the ODE system (4.17)–(4.19) numerically for a single hexagonal cell with six compartments using a variable-step, variable-order method (implemented using the function `odeint` from `scipy.integrate` in Python). We apply periodic boundary conditions in the intercellular interactions. We choose a variety of initial conditions for a, each shown in the corresponding figure, but throughout we assume that initially $b = 1/6$ and $c = 0$ in each compartment.

Fig. 4.3 presents an example of a *vertex-like* initial condition featuring a symmetric distribution of a with respect to the horizontal axis and a slight imbalance to the right. This choice of symmetry corresponds to the distal planar polarity seen in the fly wing, as described

in Chapter 1. The steady-state complex concentration obtained from this initial condition depends on whether there is destabilising (Fig. 4.3b), stabilising (Fig. 4.3c), or both types of feedback (Fig. 4.3d) present in the model. In particular, we see that destabilising feedback yields a lower-right weakly polarised state (Fig. 4.3b), whereas in the presence of both types of feedback, the system evolves to a strongly polarised state towards the lower-right side of the cell (Fig. 4.3d). It is important to note that these cases show an additional symmetry breaking, unlike the stabilising feedback case (Fig. 4.3c).

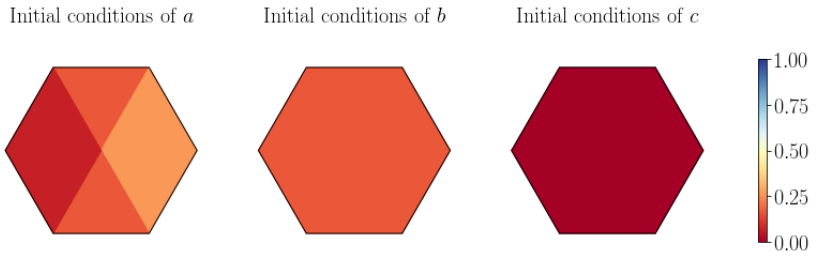

(a)

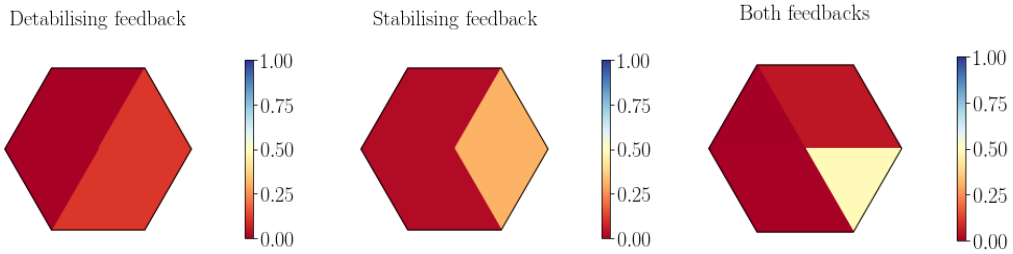

(b) $\eta = 50$. (c) $\mu = 150$. (d) $\eta = \mu = 50$.

Fig. 4.3 Vertex steady state exhibited by the one-cell model. (a) Symmetric initial condition with a small imbalance (of magnitude 0.1) in the concentration of protein a with respect to the horizontal axis; b and c are initially spatially uniform (with $c = 0$). (b-d) Steady-state concentration of c obtained from initial condition (a) and equations (4.17)–(4.19) in the case of (b) destabilising, (c) stabilising, and (d) destabilising and stabilising feedbacks of given strengths. Steady state approximated by numerical solution at $t = 10^4$. Parameter values are given in Table 4.1.

For a certain stabilising feedback strength ($\mu = 150$), an initial weakly vertex-like asymmetry in a is amplified to yield a stable vertex-like distribution of complexes, c (Fig. 4.3c).

Simulating the model for much longer (up to $t = 10^{10}$) shows that this eventually resolves into a side polarised steady state (results not shown), suggesting that the vertex polarised steady state exists but is unstable (though meta stable). This lack of stability of the vertex steady state is in agreement with modelling work by Fischer et al. [71].

In Fig. 4.4, we assume an alternative initial condition where a is asymmetric with respect to the horizontal axis of the cell. The three top compartments are assumed to have a variety of concentrations that are the same as the three bottom compartments if rotated 180° along the $x-$axis (Fig. 4.4a). This gives rise to a *triangular-like* polarity in the case of destabilising feedback (Fig. 4.4b). The triangular polarisation becomes slightly stronger if stabilising feedback is also present (Fig. 4.4d). However, stabilising feedback alone leads to a strongly symmetric polarised state towards the left-diagonal axis, with compartments 1 and 4 showing high concentrations (Fig. 4.4c).

In Fig. 4.5, we investigate another choice of initial configuration, where a is asymmetric between the top and bottom compartments of the cell. Figures 4.5b–4.5d show the resulting steady-state complex concentrations arising given the presence of destabilising, stabilising, and both types of feedback, respectively. We find that destabilising feedback leads to a weakly symmetrical polarised steady state following the same configuration as in the initial condition (Fig. 4.5a). On the other hand, strong stabilising feedback leads to a strongly double-sided polarised steady state towards the upper left and right compartments (Fig. 4.5c). A combination of both forms of feedback leads to a similar, but slightly weaker, polarity (Fig. 4.5d).

In Fig. 4.6, we consider a *triangular* asymmetric distribution of a, where the horizontal axis divides the cell into halves, each with a middle compartment having a different concentration to the others. As shown in Fig. 4.6b–4.6d, we find that this initial condition leads to an associated triangular polarised steady state distribution of c, as long as any feedback is

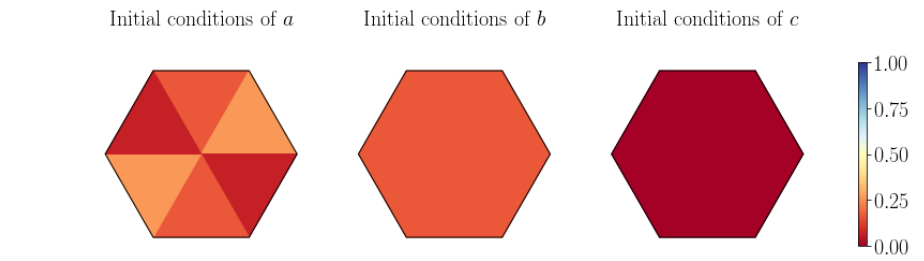

(a)

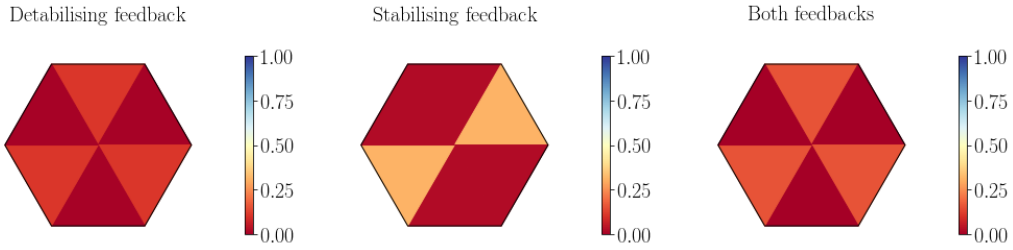

(b) $\eta = 50$. (c) $\mu = 150$. (d) $\eta = \mu = 50$.

Fig. 4.4 Triangular steady state exhibited by the one-cell model. (a) Symmetric initial condition with a small imbalance (of magnitude 0.1) in the concentration of protein a between compartments; b and c are initially spatially uniform (with $c = 0$). (b-d) Steady-state concentration of c obtained from initial condition (a) and equations (4.17)–(4.19) in the case of (b) destabilising, (c) stabilising, and (d) destabilising and stabilising feedbacks of given strengths. Steady state approximated by numerical solution at $t = 10^4$. Parameter values are given in Table 4.1.

present. This result supports previous modelling work by [71], who demonstrate that the triangular steady state is always stable.

If we instead simulate the model starting from a distinct asymmetric initial condition as in Fig. 4.7, we obtain a steady state in which polarisation generally occurs towards the upper-right half of the compartments. For a strong stabilising feedback, we obtain an upper-right strongly polarised steady state (Fig. 4.7c). With both feedbacks, we obtain a steady state where the cell is divided into two halves along its left-diagonal axis, with the right including a middle compartment surrounded by high complex concentrations (Fig. 4.7d).

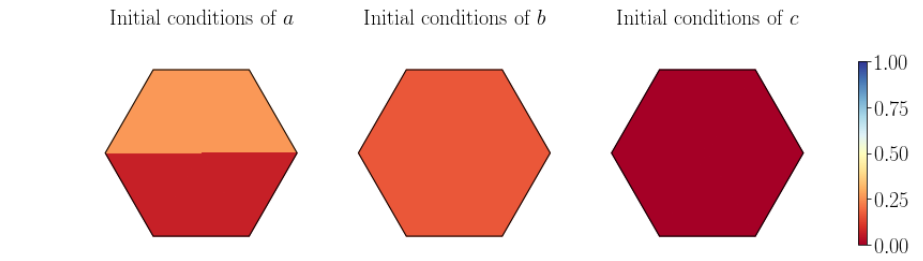

(a)

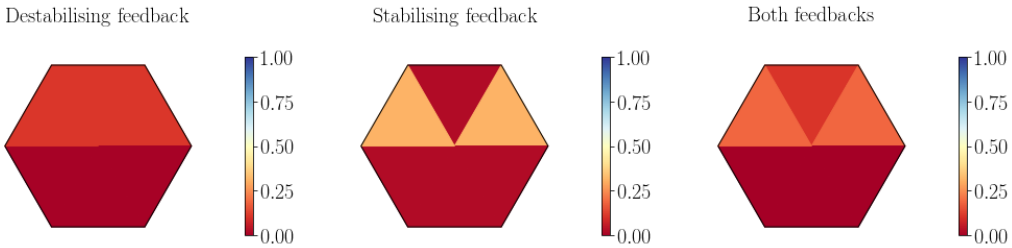

(b) $\eta = 50$. (c) $\mu = 150$. (d) $\eta = \mu = 50$.

Fig. 4.5 Top/bottom steady state exhibited by the one-cell model. (a) Symmetric initial condition with respect to the horizontal axis dividing the cell into three top and three bottom compartments with an imbalance (of magnitude 0.1) in a; b and c are initially spatially uniform (with $c = 0$). (b-d) Steady-state concentration of c obtained from initial condition (a) and equations (4.17)–(4.19) in the case of (b) destabilising, (c) stabilising, and (d) destabilising and stabilising feedbacks of given strengths. Steady state approximated by numerical solution at $t = 10^4$. Parameter values are given in Table 4.1.

Finally, we consider a distinct asymmetric-side polarised initial condition, as shown in Fig. 4.8. In this case, the cell is initialised with a direction which is opposite to that shown in Fig. 4.7. For sufficiently strong destabilising feedback strength, the system evolves to a weakly polarised triangular steady state (Fig. 4.8b). However, strong stabilising feedback instead leads to a strong sided-polarity (Fig. 4.8c). Including both stabilising and destabilising feedback leads to the same type of polarised state as the initial condition, with high concentrations towards the lower-left, but the polarity is slightly weaker than the stabilising case (Fig. 4.8d).

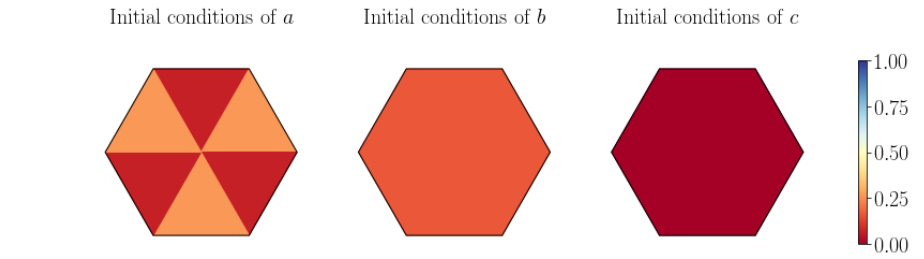

(a)

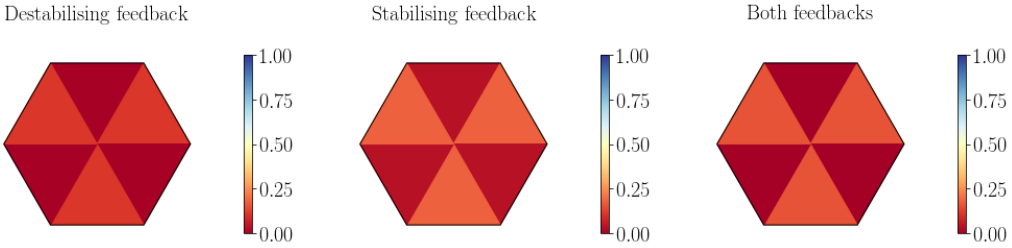

(b) $\eta = 50$. (c) $\mu = 150$. (d) $\eta = \mu = 50$.

Fig. 4.6 Triangular steady state exhibited by the one-cell model. (a) Symmetric initial condition with a small imbalance (of magnitude 0.1) in the concentration of protein a between compartments; b and c are initially spatially uniform (with $c = 0$). (b-d) Steady-state concentration of c obtained from initial condition (a) and equations (4.17)–(4.19) in the case of (b) destabilising, (c) stabilising, and (d) destabilising and stabilising feedbacks of given strengths. Steady state approximated by numerical solution at $t = 10^4$. Parameter values are given in Table 4.1.

In conclusion, in the presence of an initial bias of any of the forms discussed in Section 4.3, and in the absence of feedback, the system always evolves to a stable SUSS. The presence of sufficiently strong feedback, however, drives the system to a stable *side* or *triangular* polarised steady state. The *vertex* steady state exists for a symmetrical initial bias and strong stabilising feedback, but is always unstable.

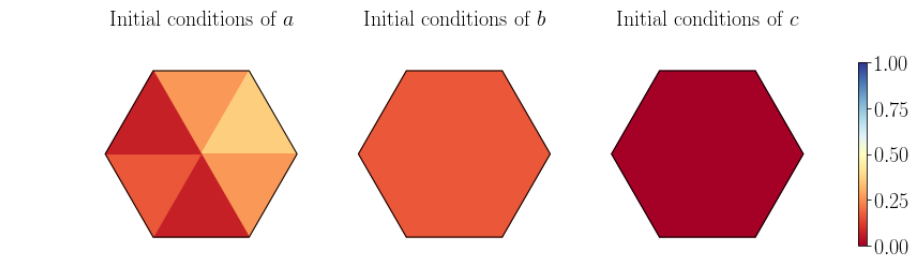

(a)

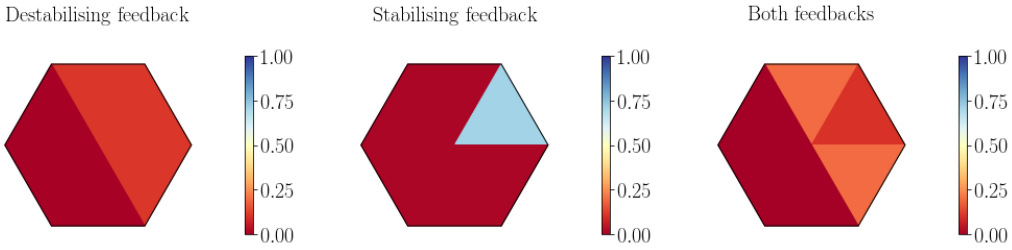

(b) $\eta = 50$. (c) $\mu = 150$. (d) $\eta = \mu = 50$.

Fig. 4.7 Asymmetric steady state exhibited by the one-cell model. (a) Asymmetric initial condition with a small imbalance (of magnitude 0.1) in the concentration of protein a between compartments; b and c are initially spatially uniform (with $c = 0$). (b-d) Steady-state concentration of c obtained from initial condition (a) and equations (4.17)–(4.19) in the case of (b) destabilising, (c) stabilising, and (d) destabilising and stabilising feedbacks of given strengths. Steady state approximated by numerical solution at $t = 10^4$. Parameter values are given in Table 4.1.

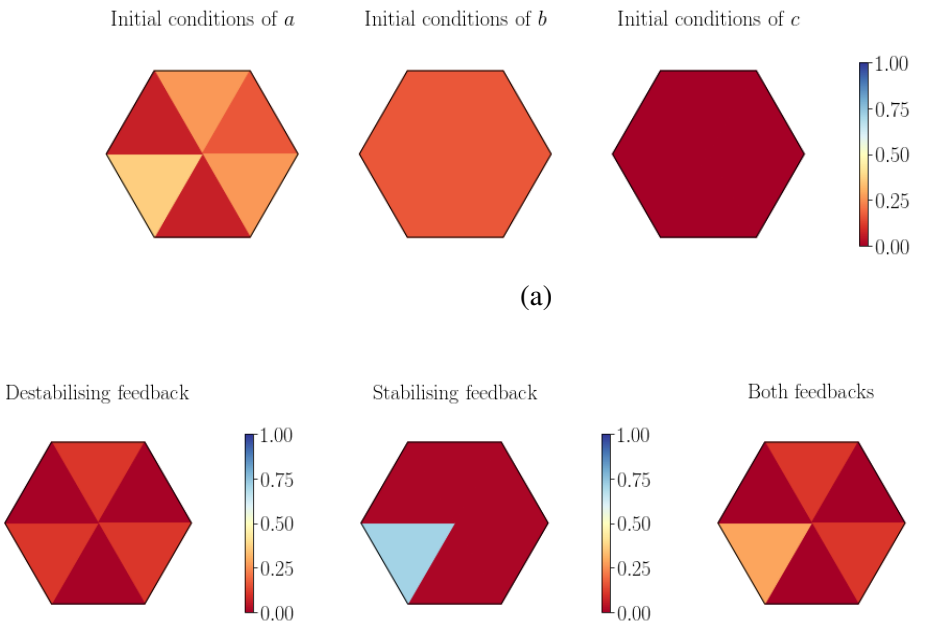

(a)

(b) $\eta = 50$. (c) $\mu = 150$. (d) $\eta = \mu = 50$.

Fig. 4.8 Asymmetric-side polarised steady state exhibited by the one-cell model. (a) Asymmetric-side triangular initial condition with a small imbalance (of magnitude 0.1) in the concentration of protein a between compartments; b and c are initially spatially uniform (with $c = 0$). (b-d) Steady-state concentration of c obtained from initial condition (a) and equations (4.17)–(4.19) in the case of (b) destabilising, (c) stabilising, and (d) destabilising and stabilising feedbacks of given strengths. Steady state approximated by numerical solution at $t = 10^4$. Parameter values are given in Table 4.1.

4.4.2 Numerical simulations for a tissue of hexagonal cells

We next extend our numerical investigations to a tissue comprised a regular array of hexagonal cells. We consider a sheet of 10×10 cells, but include an extra row/column of cells at each boundary whose governing equations are modified to reflect 'no flux' boundary conditions, thus mitigating boundary effects in our simulations. We experimented with different tissue sizes, and found no major differences in behaviours. We assume throughout that proteins a and b have the same total concentration, diffusion coefficients, and feedback parameters (if present) in every cell of the tissue, assuming the absence of any mutant cells. We also assume throughout that initially $b = 1/6$ and $c = 0$ in every compartment of every cell, while a initially has a slightly higher concentration on the right side of every cell than the left side. As before, we simulate the resulting ODE system (4.5)–(4.7) numerically using a variable-step, variable-order method (implemented using the function `odeint` from `scipy.integrate` in Python).

Fig. 4.9 shows the dynamics of a, b and c in each compartment of one cell in a tissue simulation, in the presence of destabilising (Fig. 4.9a) and stabilising (Fig. 4.9b) feedback, respectively. We find that a polarised steady state is reached quickly with destabilising feedback, in this case corresponding to the side polarised steady state illustrated in Fig. 4.3b. In contrast, the stabilising feedback model quickly evolves to a meta-steady uniform state until $t \sim 2.5 \times 10^4$, when it reaches another stable steady state. These results match our one-cell investigations showing how the vertex polarised state appears to be stable, but eventually switches to a stable side polarised steady state.

The resulting steady states are visualized in Fig. 4.10. We see that with stabilising feedback, each cell tends to a strongly polarised side steady state (Fig. 4.10b). Similarly, cells become right polarised in the presence of destabilising feedback (Fig. 4.10a), but the difference between the right and left is much smaller than the stabilising case. Hence,

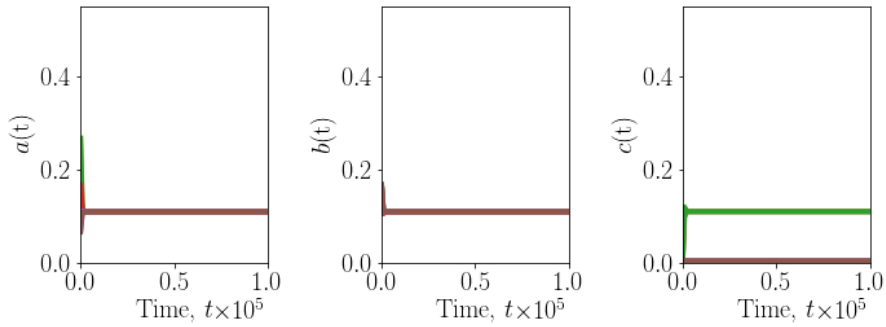

(a) Destabilising feedback.

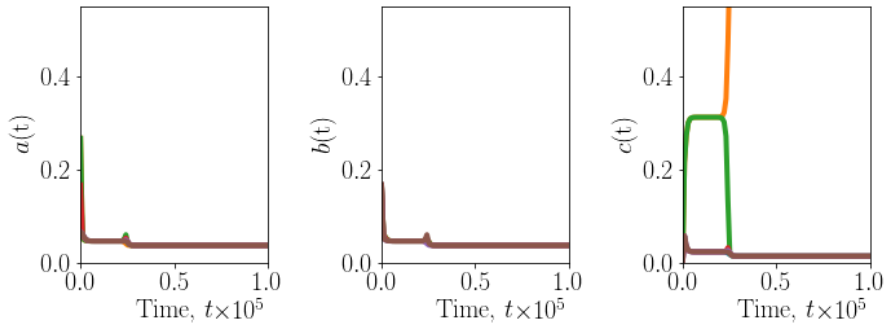

(b) Stabilising feedback.

Fig. 4.9 Numerical solution of the tissue model (4.11)–(4.13) for a tissue comprising 10×10 cells in the presence of (a) destabilising and (b) stabilising feedback. Initial conditions for each cell are the same as in Fig. 4.3a. Different colours indicate different compartments. Non-dimensional parameter values are given in Table 4.1.

introducing sufficiently strong feedback to the model drives the SUSS to a stable side polarised steady state.

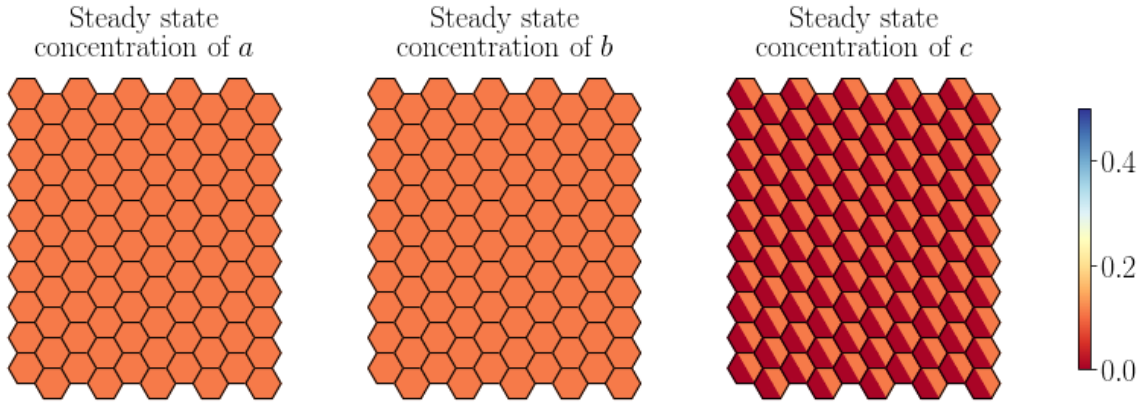

(a) Destabilising feedback.

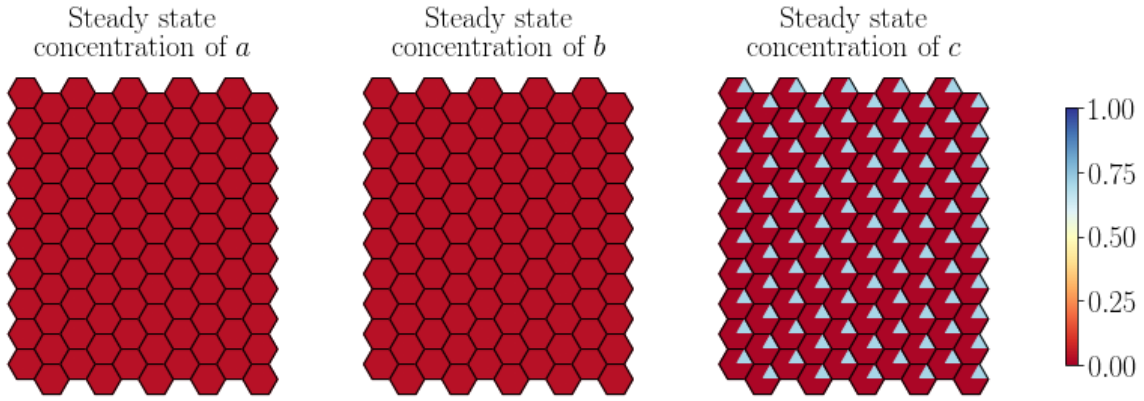

(b) Stabilising feedback.

Fig. 4.10 Numerical solution of the tissue model (4.11)–(4.13) for a tissue comprising 10×10 cells in the presence of (a) destabilising and (b) stabilising feedback. Initial conditions for each cell are the same as in Fig. 4.3a. Complex concentration c shown at $t = 10^6$. Non-dimensional parameter values are given in Table 4.1.

4.4.3 Clone phenotypes

We next investigate the behaviour of cells neighbouring a group of cells in which the abundance of each protein is perturbed. As discussed in Chapter 3, this corresponds to the presence of a mutant clone of cells in which the relevant gene is over- or underexpressed. In our 2D model, a clone is defined as a set of cell indices $i \in \mathscr{I}$ for which $6a_i + 6c_i = r$ and/or $6\gamma b_i + 6c_i = \gamma r$, where the parameter r denotes the fraction of the normal total concentration of protein a and or b in each cell. In the simulations shown below, for $\mathscr{I}$ denotes the indices of the 7 central cells in the tissue, and we take $r = 0.1$ in the case of underexpression and 4.5 in the case of overexpression.

As in Chapter 3, we discuss (at least for the degradation feedback model) results for: clones in which the total amount of a in each mutant cell is underexpressed, referred to as 'single a^- clones'; clones in which the total amount of b in each mutant cell is underexpressed, referred to as 'single b^- clones'; and clones in which both a and b in each mutant cell are underexpressed, referred to as 'double a^-b^- clones'. In addition, we show results for: clones in which a is overexpressed, referred to as 'single a^+ clones'; clones in which b is overexpressed, referred to as 'single b^+ clones'; and clones in which both a and b in each mutant cell are overexpressed, referred to as 'double a^+b^+ clones'.

Fig. 4.11 and Fig. 4.12 show example simulations demonstrating perturbed polarisation in cells surrounding clones featuring under- and overexpression, respectively, in the case of stabilising feedback. We find that cells neighbouring the clone no longer display side polarity (with the exception of a small number of cells showing disordered polarity). Instead, in the case of an a^- clone, cells above the clone are polarised towards it (Fig. 4.11a), while for a b^- clone, cells below the clone are polarised away from it (Fig. 4.11b). Perhaps counter-intuitively, for a double a^-b^- clone we observe smooth symmetry along the horizontal axis dividing the tissue into top and bottom halves. This resembles 'swirling' patterns, where

non-mutant cells' polarity rotates around the a^-b^- clone, apart from a small number of cells lying on the symmetrical horizontal axis and on the tissue boundary (Fig. 4.11c).

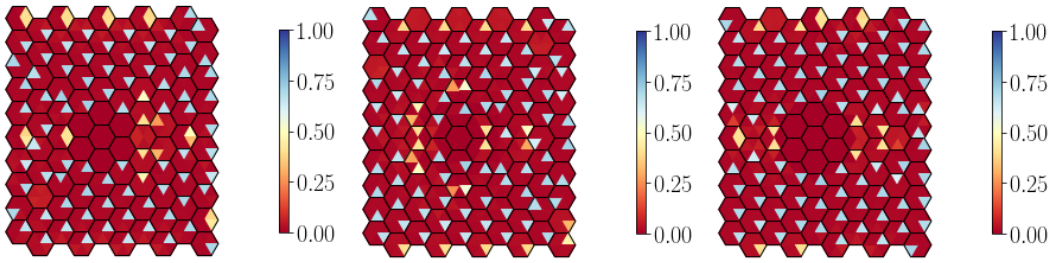

(a) a^- clone. (b) b^- clone. (c) a^-b^- clone.

Fig. 4.11 Perturbed polarisation in the tissue model (4.11)–(4.13) with stabilising feedback, for cells neighbouring (a) a single a^- clone, (b) a single b^- clone, and (c) a double a^-b^- clone, in each comprising the seven central cells. Initial conditions for each non-mutant cell are the same as in Fig. 4.3a. Complex concentration c shown at $t = 10^4$. Non-dimensional parameter values are given in Table 4.1.

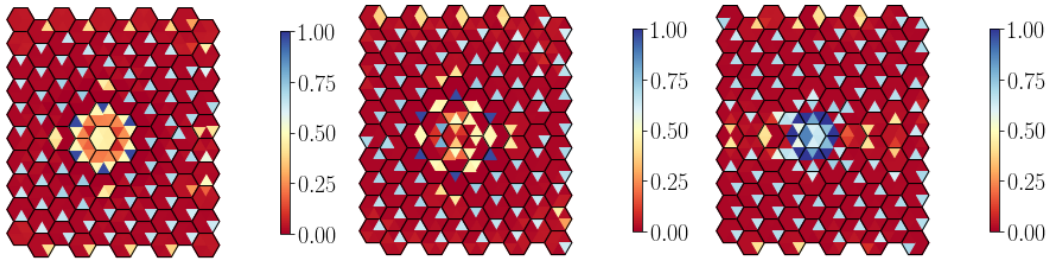

(a) a^+ clone. (b) b^+ clone. (c) a^+b^+ clone.

Fig. 4.12 Perturbed polarisation in the tissue model (4.11)–(4.13) with stabilising feedback, for cells neighbouring a clone comprising the seven central cells, in which (a) a is overexpressed, (b) b is overexpressed, and (c) both a and b are overexpressed. Initial conditions for each non-mutant cell are the same as in Fig. 4.3a. Complex concentration c shown at $t = 10^4$. The total concentration of the overexpressed protein within each clone cell is 4.5. Non-dimensional parameter values are given in Table 4.1.

For clones exhibiting overexpression and sufficiently strong stabilising feedback, we find opposing results to equivalent underexpression clones (Fig 4.12). These simulations also show a more strongly polarised phenotype. Cells neighbouring an a^+ clone show strong polarity away from the clone (Fig. 4.12a). In particular, cells below the clone show the opposite polarised state to those above the clone. In the case of a b^+ clone, however,

neighbouring cells show an even stronger polarisation towards the clone (Fig. 4.12b). Cells around the b^+ clone show weaker polarity away from the clone. Similar to Fig. 4.11c, in the case of a double a^+b^+ clone, cells neighbouring the clone show swirling patterns (Fig. 4.12c). However, this case is less symmetrical, with cells immediately neighbouring the clone polarising towards the clone.

Fig. 4.13 and Fig. 4.14 show results for the case of destabilising feedback. We find that cells above and below a single a^- or b^- clone show different polarities, depending on the specific protein: cells show an overall polarity towards an a^- clone, but away from a b^- clone. In other words, only those cells above an a^- clone (Fig. 4.14a) and below a b^- clone (Fig. 4.14b) have their polarities reoriented as a result of the clone.

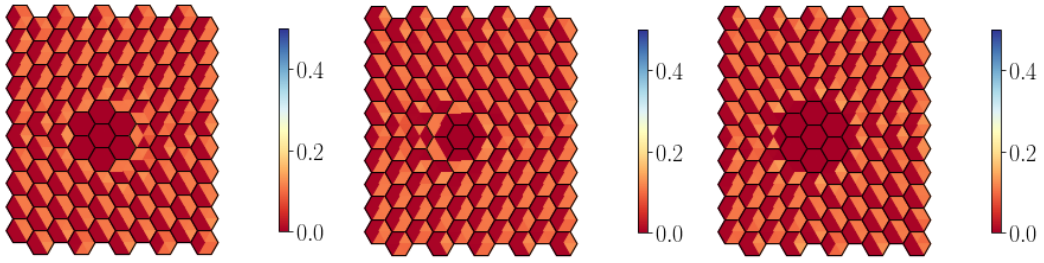

(a) a^- clone. (b) b^- clone. (c) a^-b^- clone.

Fig. 4.13 Perturbed polarisation in the tissue model (4.11)–(4.13) with destabilising feedback, for cells neighbouring (a) a single a^- clone, (b) a single b^- clone, and (c) a double a^-b^- clone, in each comprising the seven central cells. Initial conditions for each non-mutant cell are the same as in Fig. 4.3a. Complex concentration c shown at $t = 10^4$. Non-dimensional parameter values are given in Table 4.1.

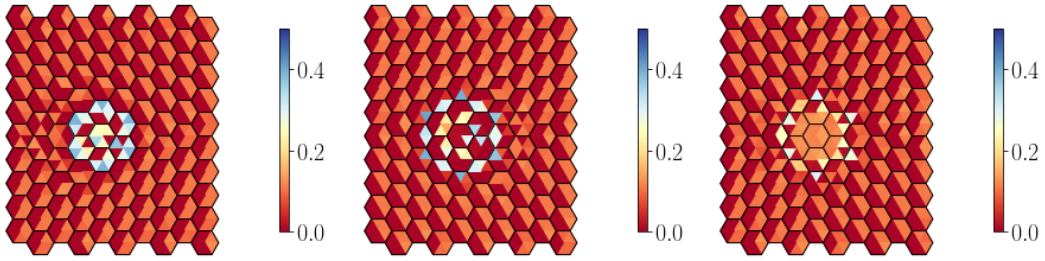

(a) a^+ clone. (b) b^+ clone. (c) a^+b^+ clone.

Fig. 4.14 Perturbed polarisation in the tissue model (4.11)–(4.13) with destabilising feedback, for cells neighbouring a clone comprising the seven central cells, in which (a) a is overexpressed, (b) b is overexpressed, and (c) both a and b are overexpressed. Initial conditions for each non-mutant cell are the same as in Fig. 4.3a. Complex concentration c shown at $t = 10^4$. The total concentration of the overexpressed protein within each clone cell is 4.5. Other non-dimensional parameter values are given in Table 4.1.

Results for single overexpression clones in the presence of sufficiently strong destabilising feedback are the opposite of those found for equivalent single underexpression clones (Fig 4.13). Cells around an a^+ clone (Fig. 4.14a) show an overall polarity away from the clone, while normal cells generally polarise towards an a^+ clone (Fig. 4.14b), with those cells immediately neighbouring the clone showing stronger polarity. In the case of a double overexpression clone (Fig. 4.14c), we observe similar behaviour to the double underexpression clone (Fig. 4.13c). However, the cells immediately neighbouring the clone show disordered polarity in this case.

Fig. 4.15 shows the result of varying the magnitude in the initial bias ε for normal cells around a single b^- clone, in the case of stabilising feedback. We find that with a stronger initial imbalance (Fig. 4.15a), there is a shorter range of effect of the clone. Results in the case of destabilising feedback are similar (not shown). These results are in agreement with previous theoretical work by Schamberg [79].

Finally, we investigate planar polarisation behaviour in the complete absence of an initial bias ($\varepsilon = 0$). Instead of initially biasing a towards a vertex state, we use spatially uniform initial conditions ($a = b = 1/6$, $c = 0$) in each normal cell compartment, with appropriate

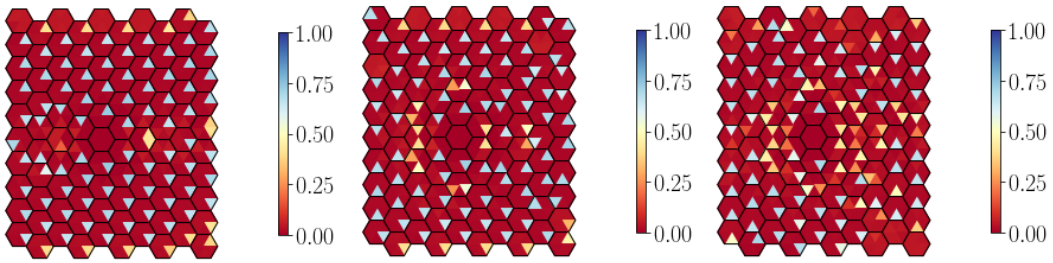

(a) $\varepsilon = 0.1$. (b) $\varepsilon = 0.01$. (c) $\varepsilon = 0.001$.

Fig. 4.15 Perturbed polarisation in the tissue model (4.11)–(4.13) with stabilising feedback, for cells neighbouring a single b^- clone comprising the seven central cells, for a range of values of the initial bias ε between the left and right sides of each normal cell. Initial conditions for each non-mutant cell are otherwise the same as in Fig. 4.3a. Complex concentration c shown at $t = 10^4$. Other non-dimensional parameter values are given in Table 4.1.

scaling for mutant cells). We then simulate the model in the presence of destabilising and stabilising feedback with a variety of different clones. The results obtained are shown in Fig. 4.16 and 4.17, respectively. We find that with sufficiently strong destabilising feedback, single and double clones result in neighbouring cells evolving to a triangular polarised state (Fig. 4.16). Single a^- clones are found drive neighbouring cells to disordered polarity in the case of destabilising (Fig. 4.16a) and stabilising feedback (Fig. 4.17a). In contrast, in the case of sufficiently strong stabilising feedback, double clones (Fig. 4.17b and 4.17c) drive neighbouring cells into a complex pattern that more reminiscent of the period two patterns observed in some clone simulations in Chapter 3. Single a^+, b^+ and b^- clones have a similar effect on the polarisation of neighbouring cells (results not shown).

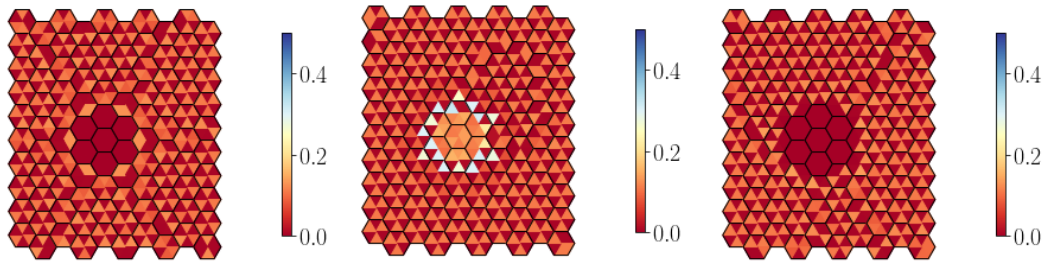

(a) a^- clone. (b) a^+b^+ clone. (c) ab^- clone.

Fig. 4.16 Perturbed polarisation in the tissue model (4.11)–(4.13) with destabilising feedback, for cells neighbouring (a) a single a^- clone, (b) a clone in which both a and b are overexpressed, and (c) a double a^-b^- clone, in each comprising the seven central cells, in the absence of an initial bias ($\varepsilon = 0$). Initial conditions for each non-mutant cell are otherwise the same as in Fig. 4.3a. In (b) the total concentration of each overexpressed protein within each clone cell is 4.5. Complex concentration c shown at $t = 10^4$. Other non-dimensional parameter values are given in Table 4.1.

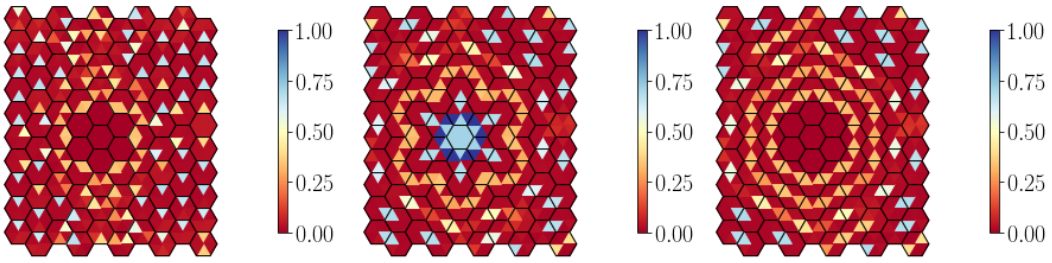

(a) a^- clone. (b) a^+b^+ clone. (c) a^-b^- clone.

Fig. 4.17 Perturbed polarisation in the tissue model (4.11)–(4.13) with stabilising feedback, for cells neighbouring (a) a single a^- clone, (b) a single b^- clone, and (c) a double a^-b^- clone, in each comprising the seven central cells, in the absence of an initial bias ($\varepsilon = 0$). Initial conditions for each non-mutant cell are otherwise the same as in Fig. 4.3a. Complex concentration c shown at $t = 10^4$. Other non-dimensional parameter values are given in Table 4.1.

4.5 Discussion

In this chapter, we have presented a detailed numerical investigation of a simplified planar polarisation model in two spatial dimensions. As an extension to the binding feedback model presented in Chapter 3, we started by considering a single hexagonal cell with six compartments, and analysed the dynamics of this model with different types of possible steady states in response to different initial symmetries. We then moved on to consider a tissue comprising a sheet of cells, some of which may be mutant.

Throughout this chapter, we used the standard of the default baseline set of parameter values given in Table 4.1. To obtain a similar tissue-scale polarisation to that observed in the fly wing, our model shows that the initial conditions must be symmetric with respect to the horizontal axis (Fig. 4.3). Although this *vertex* polarised state exists, it is not stable. Nevertheless, asymmetric initial conditions for the same parameter values give rise to stable configurations, but this is usually biologically undesirable. For instance, a *triangular* initial state is always stable in the presence of sufficiently strong feedback (Fig. 4.6). One suggested mechanism to ensure stable proximal polarity is the addition of a weak global bias to direct tissue polarity [81].

Our numerical simulations show that the steady state reached in the presence of strong feedback has the same orientation as the initial bias, in agreement with previous theoretical modelling [38, 63, 71]. Simulation results using different initial states show that the triangular and side steady states are stable, while the desired vertex polarised steady state in the fly wing is not stable. This finding is in agreement with previous modelling by Fischer et al. [71].

Clone analysis of our model with stabilising or destabilising feedback shows that the loss of activity in a group of cells within a tissue can cause the wild-type neighbouring cells to point towards the a^- clone and away from the b^- clone. However, overexpression clones drive surrounding cells to polarise away from the clone. These results (with either

stabilising or destabilising feedback) capture the experimentally observed event of *domineering non-autonomy* [38], discussed in Chapter 1. Our findings may be related to the experimental observation that wild-type cells neighbouring a Fz^- clone polarise towards the clone (Fig. 4.11a), while cells around $Vang^-$ clone are induced to polarise away from the clone (Fig. 4.11b).

According to our simulations, overexpression of genes also provides results that are similar to those discovered in fly wing mutant tissues. Experimentally, Fz^+ clones have been found to reorient surrounding wild-type cells to polarise away from the clone (Fig. 4.12a), while the wild-type cells surrounding the $Vang^+$ clones polarise towards the clone (Fig. 4.12b) [38]. Notably, tissues with double mutant clones show strong symmetry along the horizontal axis dividing the tissue into top and bottom halves. Given the same form of feedback, we occasionally observe equivalents to the period two patterns in a 1D line of cells observed in our simulations in Chapter 3.

In the case where no bias is applied, our simulations show that clones drive more complicated patterns. Swirling hair patterns are an example of complicated patterns in the fly wing, which have been observed in several experimental studies and have been deemed to be a result of a variety of genetic mutations. In the core planar polarity pathway, for example, swirling patterns are seen in *dsh* mutant clones [82, 83]. More recently, Fisher et al. [63] found that double clones are able to generate non-autonomous phenotypes that in some circumstances result in swirling hairs.

Overall, the results of our simulations are in agreement with those of the 1D model in Chapter 3, which indicate that sufficiently strong feedback is needed for correct polarisation if there is an initial imbalance between the proximal and distal ends of each cell. In addition, under- or overexpression of proteins in a group of mutant cells can lead to an opposing effect on their neighbouring wild-type cells. While an initial bias is essential for obtaining tissue polarity [71], clones (or more generally, groups of cells with stochastically higher or lower

protein concentrations within the developing tissue) might be considered as an additional bias or cue, providing more complicated patterning such as triangular patterns in 2D and period two patterns observed in our 1D model. In the next chapter, we extend this work to consider the combined roles of feedback interactions and global cues in planar polarisation, using a more biochemically detailed model tailored to the Ft-Ds pathway.

Chapter 5

Feedbacks and global cues in the Ft-Ds pathway

5.1 Introduction

In Chapter 4 we developed a framework for modelling the intracellular diffusion and transmembrane binding of two abstract planar polarity proteins in a static 2D tissue comprising hexagonal cells. In this chapter, we extend this framework to consider a much more biochemically detailed model of a planar polarity pathway.

As discussed in Chapter 1, the establishment and maintenance of planar polarisation is known to involve global cues such as tissue-level signalling gradients as well as local cell-cell interactions. The Fat-Dachsous (Ft-Ds) pathway in the fly wing offers an excellent system in which to study the relative contributions of these two mechanisms. The activity of the Four-jointed (Fj) enzyme forms a gradient along a developing wing, and this tissue-level gradient acts as a 'global' polarising cue [84], which is then converted into subcellular asymmetries in the cadherin molecules Ft and Ds [19]. Ft and Ds bind heterophilically between neighbouring cells using their cadherin repeats [85]. Fj acts as a kinase in the Golgi apparatus, an organelle found within each cell, to phosphorylate Ft and Ds and modify their

binding affinities [42]. As with the core pathway, local amplifying feedback interactions have also been proposed to play a role in the asymmetric localisation of Ft and Ds [81].

An understanding of cell-to-tissue polarisation requirements depends upon integrating the contributions of two important factors: first, the global cue that transfers polarisation signals across the tissue; and second, the local feedback interactions that result in the asymmetric localisation and stability of heterodimers within each cell. In the core pathway, the source of global cue is still uncertain [86]. In contrast, it is well established that a gradient in Fj activity is the source of global cue in the Ft-Ds system [76]. With regard to local feedback interactions, it is worth noting that the core pathway consists of six proteins that can form a variety of complexes of different stoichiometries [63], whereas in the Ft-Ds system there are only two transmembrane proteins that form complexes. Nevertheless, the precise nature of feedback interactions and the mode of action of Fj remain unclear. The Ft-Ds pathway thus offers a tractable planar polarity system with which to employ more biochemically detailed modelling than the approach we have taken elsewhere in this thesis.

Various mathematical models have been developed to explain how the Ft-Ds pathway operates. One example is the model by Jolly et al. [87], who construct an ODE-based system corresponding to a one-dimensional line of cells. Their model captures key molecular interactions in the Ft-Ds pathway, including Ft-Ds complex formation, Fj phosphorylation, and opposing tissue-level gradients of Fj and Ds. Analysis of this model suggests that levels of Ft-Ds heterodimers at cell-cell junctions, and levels of phosphorylated Ft and Ds in the cytoplasm, evolve over time to a unique globally stable steady state over time regardless of initial conditions. The theoretical findings also suggest that phosphorylation of Ft and the elevated distal gradient of Fj along the fly wing are essential for attaining subcellular asymmetry localisation of Ft-Ds heterodimers, and consequently tissue-scale polarity. However, boosting phosphorylation of Ds allows robustness to polarity across the tissue. When Fj phosphorylation of Ft is lost, asymmetry of Ft-Ds complex is distributed,

whereas loss of Fj activity on Ds does not influence asymmetrical localisation of Ft-Ds heterodimers. However, it remains unclear how these authors' findings, particularly with respect to simulated clone phenotypes, extend to two spatial dimensions.

In other work, Singh et al. [88] consider a minimal mechanistic model in one and two spatial dimensions of the Ft-Ds pathway to investigate the rule of global tissue-level gradients and complex local asymmetric distribution. This model suggests that polarisation is tightly related to a threshold membrane-bound protein concentration, above which Ft and Ds form heterodimer complexes. Based on their theoretical analysis, the authors hypothesise a sorting mechanism in which the stability of either Ft or Ds on junctions depend on the total concentrations of one another on the opposite orientation. Although this work considers Ft-Ds dynamics in two spatial dimensions, it is somewhat lacking in biological detail, and provides limited insight into the factors that may affect heterodimer stability in this system.

A more biochemically detailed modelling approach is taken by Hale et al. [44], who develop a computational model of Ft-Ds polarisation in a one-dimensional line of cells, each comprising a left and a right compartment. In this model, in the absence of any feedback amplification a linear gradient of Fj activity is sufficient to generate Ft-Ds polarisation of similar degree to that observed experimentally in the fly wing. Testing their model in *vivo*, Hale et al. [44] conclude that the removal of Fj gradient activity results in a reduction in the Ft-Ds dimer stability using fluorescence recovery after photobleaching. Experimentally, Fj is expressed as a gradient of approximately 3% between neighbouring cells along the proximal-distal axis [44]. Consistent with their modelling predictions, the authors find that the removal of Fj activity on Ds enhance Ft-Ds heterodimer stability, while the loss of its effect on Ft reduces heterodimer stability.

A key feature of the computational model by Hale et al. [44] is the consideration of different possible complexes between phosphorylated and non-phosphorylated forms of Ft and Ds. Based on *in vitro* experiments [42, 43], the strongest binding affinity is formed

by phosphorylated Ft and unphosphorylated Ds, and the weakest is the binding between unphosphorylated Ft and phosphorylated Ds. However, it remains unclear to what extent the results of Hale et al. [44] carry over to two spatial dimensions. In addition, recent experimental observations [81] as well as previous work by [89, 42] suggest the possibility of an amplifying feedback mechanism that enhances the gradient expression of Fj, which is not considered in the model by Hale et al. [44].

5.1.1 Aim of work

Although the above models shed some light on the the factors that are essential for the Ft-Ds system to achieve tissue-scale polarisation, the relative contributions of tissue-level gradient and feedback interactions is still unknown. Our aim in this chapter is to determine the mechanism by which a uniform tissue polarisation is obtained via sensing different levels of gradient transcriptions between neighbouring cells. Here, we use the Ft-Ds pathway in the fly wing to address this biological problem. The readout polarity of the Ft-Ds pathway is visible via the asymmetrical distribution of Ft and Ds dimers along the tissue axis (Fig. 5.1). In the fly wing, Fj is expressed as a tissue-level gradient, high distally at the wing tip and low proximally towards the fly body. Both Ft and Ds are mobile and able to be redistributed to their most favourable cellular edge.

Mathematical modelling suggests that the graded expression of Fj and Ds could be sufficient to generate the observed cellular asymmetry in the absence of feedback amplification [44, 87, 90]. Nevertheless, it is not yet clear whether the shallow gradient expressions in *vivo* may result in the recognised cellular asymmetry. Thus, it has been suggested that some feedback interaction may contribute [42, 44, 89]. Our aim in this chapter is to extend the computational model by Hale et al. [44] to two spatial dimensions with the aim of investigating whether enough polarity is obtained, given the input of a shallow gradient of Fj activity.

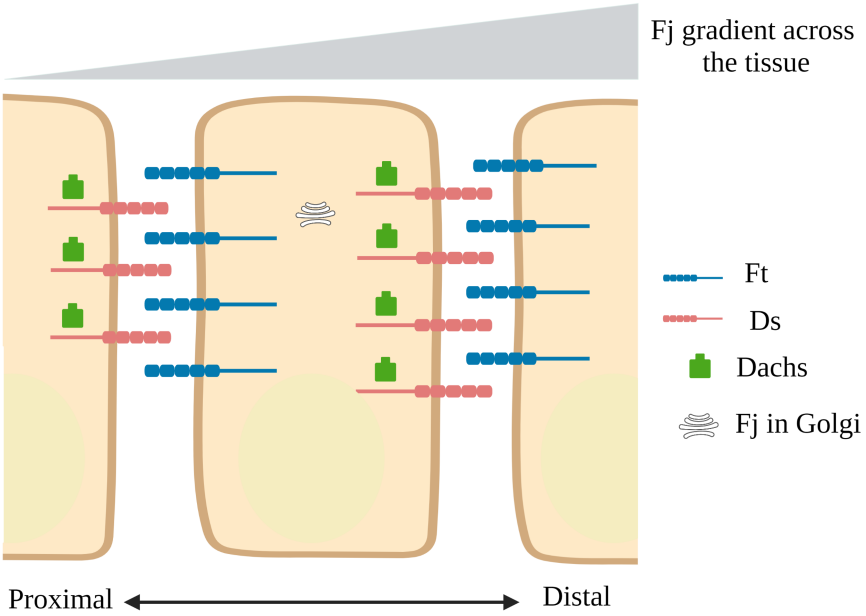

Fig. 5.1 Schematic of the localisation of Ft and Ds on the proximal and distal sides of each cell in the developing fly wing. Ft is expressed uniformly along the tissue axis, while Ds is expressed as a gradient from the proximal to the distal edge of the wing. Dachs, an effector protein of the Ft-Ds system, is asymmetrically localised to the distal edge of each cell, while Fj localises to the Golgi apparatus. This schematic is created with BioRender.

The remainder of this chapter is structured as follows. We first revisit the 1D model by Hale et al. [44] in Section 5.2, and summarise their main findings. We then extend the model to 2D in Section 5.3 and explore numerically whether a shallow Fj tissue-gradient is sufficient to obtain experimentally observed levels of Ft-Ds heterodimer asymmetry. In addition, we explore the effect of possible feedback amplification on the existing mechanism and the overall polarity. We conclude in Section 5.4 with a discussion of our results and how their implications for understanding Ft-Ds polarisation.

5.2 Modelling Ft-Ds activity in one spatial dimension

5.2.1 Governing equations

Let F_i^m, S_i^m, $\tilde{F}_i^m$ and $\tilde{S}_i^m$ denote the concentrations of Ft and Ds proteins and their phosphorylated copies in cell i, compartment $m \in \{L,R\}$ (the left and right edges of the cell, respectively) at time t. Following Hale et al. [44], we assume that these proteins can bind and unbind to form the complexes A_i^j, B_i^j, C_i^j and D_i^j according to the chemical reactions

$$\tilde{F}_i^R + S_{i+1}^L \rightleftharpoons A_i^R, \tag{5.1}$$

$$\tilde{F}_i^R + \tilde{S}_{i+1}^L \rightleftharpoons B_i^R, \tag{5.2}$$

$$F_i^R + S_{i+1}^L \rightleftharpoons C_i^R, \tag{5.3}$$

$$F_i^R + \tilde{S}_{i+1}^L \rightleftharpoons D_i^R, \tag{5.4}$$

and be trafficked between left and right compartments of each cell according to the reactions

$$F_i^L \rightleftharpoons F_i^R, \tag{5.5}$$

$$\tilde{F}_i^L \rightleftharpoons \tilde{F}_i^R, \tag{5.6}$$

$$S_i^L \rightleftharpoons S_i^R, \tag{5.7}$$

$$\tilde{S}_i^L \rightleftharpoons \tilde{S}_i^R, \tag{5.8}$$

for $i \in \{0,1,\ldots,N-1\}$. We assume that reactions (5.1)–(5.4) proceed with forward rate constant k_i and backward rate constant v_i, where $i \in \{a,b,c,d\}$, depending on the corresponding complex type. In addition, we assume that Ft and Ds and their phosphorylated copies are trafficked between cell compartments with effective diffusion rates δ_F, $\delta_{\tilde{F}}$, δ_S and $\delta_{\tilde{S}}$,

respectively. Applying the Law of Mass Action yields the following system ODEs for cell i:

$$\frac{dF_i^L}{dt} = -k_c F_i^L S_{i-1}^R - k_d F_i^L \tilde{S}_{i-1}^R + v_c C_i^L + v_d D_i^L + \delta_F (F_i^R - F_i^L), \tag{5.9}$$

$$\frac{dF_i^R}{dt} = -k_c F_i^R S_{i+1}^L - k_d F_i^R \tilde{S}_{i+1}^L + v_c C_i^R + v_d D_i^R + \delta_F (F_i^L - F_i^R), \tag{5.10}$$

$$\frac{d\tilde{F}_i^L}{dt} = -k_a \tilde{F}_i^L S_{i-1}^R - k_b \tilde{F}_i^L \tilde{S}_{i-1}^R + v_a A_i^L + v_b B_i^L + \delta_{\tilde{F}} (\tilde{F}_i^R - \tilde{F}_i^L), \tag{5.11}$$

$$\frac{d\tilde{F}_i^R}{dt} = -k_a \tilde{F}_i^R S_{i+1}^L - k_b \tilde{F}_i^R \tilde{S}_{i+1}^L + v_a A_i^R + v_b B_i^R + \delta_{\tilde{F}} (\tilde{F}_i^L - \tilde{F}_i^R), \tag{5.12}$$

$$\frac{dS_i^L}{dt} = -k_a \tilde{F}_{i-1}^R S_i^L - k_c F_{i-1}^R S_i^L + v_a A_{i-1}^R + v_c C_{i-1}^R + \delta_S (S_i^R - S_i^L), \tag{5.13}$$

$$\frac{dS_i^R}{dt} = -k_a \tilde{F}_{i+1}^L S_i^R - k_c F_{i+1}^L S_i^R + v_a A_{i+1}^L + v_c C_{i+1}^L + \delta_S (S_i^L - S_i^R), \tag{5.14}$$

$$\frac{d\tilde{S}_i^L}{dt} = -k_b \tilde{F}_{i-1}^R \tilde{S}_i^L - k_d F_{i-1}^R \tilde{S}_i^L + v_b B_{i-1}^R + v_d D_{i-1}^R + \delta_{\tilde{S}} (\tilde{S}_i^R - \tilde{S}_i^L), \tag{5.15}$$

$$\frac{d\tilde{S}_i^R}{dt} = -k_b \tilde{F}_{i+1}^L \tilde{S}_i^R - k_d F_{i+1}^L \tilde{S}_i^R + v_b B_{i+1}^L + v_d D_{i+1}^L + \delta_{\tilde{S}} (\tilde{S}_i^L - \tilde{S}_i^R), \tag{5.16}$$

$$\frac{dA_i^L}{dt} = k_a \tilde{F}_i^L S_{i-1}^R - v_a A_i^L, \tag{5.17}$$

$$\frac{dA_i^R}{dt} = k_a \tilde{F}_i^R S_{i+1}^L - v_a A_i^R, \tag{5.18}$$

$$\frac{dB_i^L}{dt} = k_b \tilde{F}_i^L \tilde{S}_{i-1}^R - v_b B_i^L, \tag{5.19}$$

$$\frac{dB_i^R}{dt} = k_b \tilde{F}_i^R \tilde{S}_{i+1}^L - v_b B_i^R, \tag{5.20}$$

$$\frac{dC_i^L}{dt} = k_c F_i^L S_{i-1}^R - v_c C_i^L, \tag{5.21}$$

$$\frac{dC_i^R}{dt} = k_c F_i^R S_{i+1}^L - v_c C_i^R, \tag{5.22}$$

$$\frac{dD_i^L}{dt} = k_d F_i^L \tilde{S}_{i-1}^R - v_d D_i^L, \tag{5.23}$$

$$\frac{dD_i^R}{dt} = k_d F_i^R \tilde{S}_{i+1}^L - v_d D_i^R. \tag{5.24}$$

The total (bound and unbound) concentrations of both phosphorylated and unphosphorylated Ft and Ds are conserved in each cell:

$$F_T = F_i^L + C_i^L + D_i^L + F_i^R + C_i^R + D_i^R, \tag{5.25}$$

$$\tilde{F}_T = \tilde{F}_i^L + A_i^L + Bi^L + \tilde{F}_i^R + A_i^R + B_i^R, \tag{5.26}$$

$$S_T = S_i^L + A_{i-1}^R + S_i^R + D_{i-1}^R + A_{i+1}^L + D_{i+1}^L, \tag{5.27}$$

$$\tilde{S}_T = \tilde{S}_i^L + B_{i-1}^R + D_{i-1}^R + \tilde{S}_i^R + B_{i+1}^L + D_{i+1}^L, \tag{5.28}$$

for positive constants F_T, $\tilde{F}_T$, S_T and $\tilde{S}_T$. Following Hale et al. [44], we assume that the rate at which Fj phosphorylates either or both Ft and Ds is proportional to its concentration at a particular cell edge, and that phosphorylation is sufficiently rapid to be in quasi-steady state, since Fj is based in the Golgi. Hence we do not explicitly include flux terms between the phosphorylation and unphosphorylated forms of Ft and Ds, respectively. This explains why we have a total of four conserved quantities (F_T, $\tilde{F}_T$, S_T, and $\tilde{S}_T$) in each cell.

As discussed in Section 5.1, the Ft-Ds polarisation is 'read out' via differences in the levels of total bound Ft and Ds on each cell edge. Mathematically, the total bound Ft and Ds on the left and the right edges of cell (i, j), respectively are represented by

$$F_T^L = A_i^L + B_i^L + C_i^L + D_i^L, \tag{5.29}$$

$$F_T^R = A_i^R + B_i^R + C_i^R + D_i^R, \tag{5.30}$$

$$S_T^L = A_{i-1}^R + B_{i-1}^R + C_{i-1}^R + D_{i-1}^R, \tag{5.31}$$

$$S_T^R = A_{i+1}^L + B_{i+1}^L + C_{i+1}^L + D_{i+1}^L. \tag{5.32}$$

5.2.2 Numerical simulations

Having presented the governing equations for the 1D Ft-Ds model, we next conduct a numerical investigation to verify the key results of Hale et al. [44]. For simplicity, we do not carry out a formal non-dimensionalisation of this model as in Chapters 3–4, to facilitate direct comparison with the results of Hale et al. [44]. Instead, we consider (5.9)–(5.24) to already be in a non-dimensional form. Due to the size of the system, we also omit the usual steady state and linear stablity analysis. This is in part because the spatially non-uniform

influence of Fj means that, even in the absence of any feedback interactions, we do not expect the system to evolve to a stable SUSS, but instead to a stable spatially non-uniform steady state. Throughout the rest of this chapter, unless stated otherwise, we use the same parameter values and assumptions regarding Fj activity as proposed by Hale et al. [44].

The Fj gradient acts as a morphogen that alters Ft and Ds cadherin affinities along the tissue. The resulting polarity hence arises due to the local activity between adjacent cells and the preferred binding affinities between phosphorylated Ft-Ds heterodimers. In this model, binding rates of Ft and Ds are parameterised using the association constant (k/v). Relative binding strengths for different species used in our simulations are such that phosphorylated Ds inhibits its binding, while phosphorylated Ft promotes its binding. These relative binding strengths are presented in Table 5.1. The difference between the left and right of each cell represent the differences between proximal and distal cell edges in the developing fly wing.

Complex type / Figure	A ($\tilde{F} : S$)	B ($\tilde{F} : \tilde{S}$)	C ($F : S$)	D ($F : \tilde{S}$)
Fig. 5.2	1	$1/4$	$1/4$	$1/16$
Fig. 5.3	1	$1/2$	$1/4$	$1/4$

Table 5.1 Set of the association constants (k/v) for different complex combinations of the Ft-Ds model adapted from Hale et al. [44].

To simulate Ft-Ds binding between neighbouring cells relative to a Fj gradient, we numerically solve the system (5.9)–(5.24) for a one-dimensional line of $N = 20$ cells of equal size, each with two compartments, numerically using a variable-step, variable-order method (implemented using the function `odeint` from `scipy.integrate` in Python).

Following Hale et al. [44], we implement no-flux boundary conditions at the left and right tissue boundaries, through the inclusion of 'half cells' at these boundaries that mirror the activity of the boundary cells.

We assume that initially, there are no complexes present, and unbound Ft and Ds (in both phosphorylated and unphosphorylated forms) are distributed evenly within each cell. We

further assume that the fraction of Ft and/or Ds that is initially phosphorylated varies with the level of Fj activity in each cell, depending on the modelling assumption made in each simulation. Thus, the initial condition for each simulation is given by

$$F_i^L(0) = F_i^R(0) = F_0(1 - p_F(i)), \tag{5.33}$$

$$\tilde{F}_i^L(0) = \tilde{F}_i^R(0) = F_0 p_F(i), \tag{5.34}$$

$$S_i^L(0) = S_i^R(0) = S_0(1 - p_S(i)), \tag{5.35}$$

$$\tilde{S}_i^L(0) = \tilde{S}_i^R(0) = S_0 p_S(i), \tag{5.36}$$

$$A_i^L(0) = A_i^R(0) = 0, \tag{5.37}$$

$$B_i^L(0) = B_i^R(0) = 0, \tag{5.38}$$

$$C_i^L(0) = C_i^R(0) = 0, \tag{5.39}$$

$$D_i^L(0) = D_i^R(0) = 0, \tag{5.40}$$

for $i \in \{0, \ldots N-1\}$, where we assume the following linear forms for the Fj activity gradient [44]:

$$p_F(i) = \begin{cases} \dfrac{p_0 + i\Delta}{p_0 + N\Delta} & \text{if Fj acts on Ft} \\ 1 & \text{if Fj does not act on Ft,} \end{cases} \tag{5.41}$$

$$p_S(i) = \begin{cases} \dfrac{p_0 + i\Delta}{p_0 + N\Delta} & \text{if Fj acts on Ds} \\ 1 & \text{if Fj does not act on Ds,} \end{cases} \tag{5.42}$$

Unless stated otherwise, we use parameter values $p_0 = 80$, $\Delta = 3$, $F_0 = S_0 = 50$ in our numerical simulations. These and other model parameters are motivated by the experimentally determined Fj gradient of around 3% between neighbouring cells along the proximal-distal axis of the developing fly wing [44]. We choose values of k/v for different complex combinations such that $A > B = C > D$, with the complex of phosphorylated Ft and Ds having

the fastest, and Ft with phosphorylated Ds having the lowest 'on' rate among other complex combinations to reflect different stable concentrations measured experimentally [42–44].

Fig. 5.2 shows the total bound proteins with different assumptions regarding Fj activity on either or both Ft and Ds, with the association constant values shown in Table 5.1. As expected, in the absence of Fj activity, the system does not polarise but instead shows an even distribution of Ft and Ds between the left and right edges (Fig. 5.2a–5.2b). If instead Fj is only allowed to act on either Ft or Ds, weak asymmetry of both bound Ft and Ds is observed across the line of cells (Fig. 5.2c–5.2f). If Fj acts only on Ds (Fig. 5.2c, Fig. 5.2d), moving towards high levels of Fj activity, a tissue gradient of high to low binding of Ft-Ds complexes is observed with an average polarity of 0.7% in total bound Ft and Ds. Conversely, an overall tissue gradient of low to high Ft-Ds binding is observed if Fj acts only on Ft (Fig. 5.2e and Fig. 5.2f), with an average of 1.3% in the total Ft and Ds. However, an overall improvement on cellular asymmetry (2.5% in total Ft and Ds) is obtained when Fj is permitted to act on both Ft and Ds (Fig. 5.2g, Fig. 5.2h), with a further reduction of the relative tissue gradient.

The simulations in Fig. 5.2 suggest that Fj has an opposing activity on Ft and Ds localisation, with a stronger effect on Ft. The association constants are hence adapted to allow for phosphorylated Ds having less significant effect on binding to Ft [44]. In addition, the rate for which phosphorylated Ds is allowed to inhibit its binding with phosphorylated Ft is reduced, i.e. $A > B > C = D$. Fig. 5.3 shows the resulting total bound Ft and Ds at steady state when the Ft-Ds binding affinities are modified to reflect that Ds binding to Ft is most preferable if Ft is phosphorylated by Fj. Binding affinity is intermediate when Ft and Ds are both phosphorylated, with an overall cellular asymmetry of 1.7% in the total Ft and Ds. The overall tissue gradient of Ft-Ds binding follows the Fj gradient. The weakest binding is confirmed in the case when Ft and Ds are both non-phosphorylated, or when only Ds is phosphorylated. Thus, the model predicts that moving from a low-Fj region to a high-Fj region, the stable Ft-Ds dimers accumulate at cell junctions.

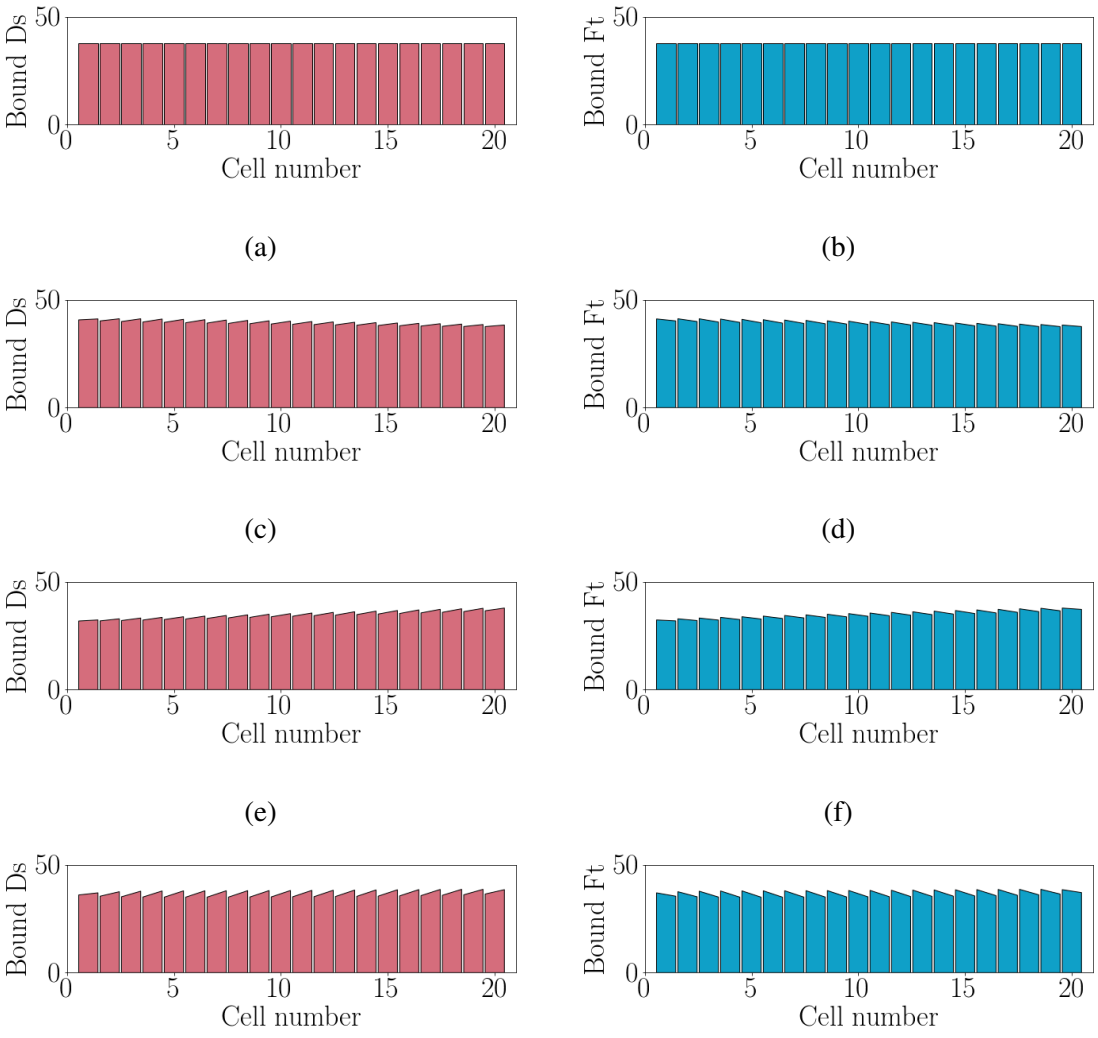

Fig. 5.2 Numerical solution of the 1D Ft-Ds model (5.9)–(5.24) with initial condition (5.33)–(5.40) and no-flux boundary conditions, under different assumptions on the action of Fj on Ft and/or Ds: (a, b) Fj does not act on Ft nor Ds; (c, d) Fj acts only on Ds; (e, f) Fj acts only on Ft; (g, h) Fj acts on both Ft and Ds. Association constants are given in Table 5.1. Other non-dimensional parameter values are $\delta_F = \delta_{\tilde{F}} = \delta_S = \delta_{\tilde{S}} = 10$. Teal: total bound Ft on each cell edge (5.29)–(5.30); pink: total bound Ds on each cell edge (5.31)–(5.32). Numerical solution shown at $t = 20$.

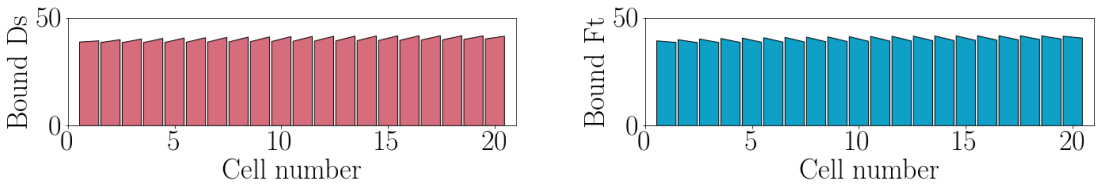

(a) Fj acts on both Ft and Ds

(b) Fj acts on both Ft and Ds

Fig. 5.3 Numerical solution of the 1D Ft-Ds model (5.9)–(5.24) with initial condition (5.33)–(5.40) and no-flux boundary conditions, assuming that Fj acts more strongly on Ft than on Ds. A Fj expression gradient of 3% is allowed to act on both Ft and Ds. Association constants are given in Table 5.1. Other non-dimensional parameter values are $\delta_F = \delta_{\tilde{F}} = \delta_S = \delta_{\tilde{S}} = 10$. Teal: total bound Ft on each cell edge (5.29)–(5.30); pink: total bound Ds on each cell edge (5.31)–(5.32). Numerical solution shown at $t = 20$.

Overall our 1D simulations confirm the findings of Hale et al. [44] that, given a shallow gradient of Fj activity along the tissue axis, there must exist extra two constraints on binding strengths in order to recapitulate the observed even distribution of bound Ft-Ds complexes at cell junctions. First, there must be a hierarchy of binding strengths across the tissue. Second, Ds phosphorylation must act in an opposing gradient in order to counter the effect of Ft phosphorylation. Hence, the effect of Fj on Ft/Ds phosphorylation results in an opposing effect on their binding activity. However, our simulation results show relatively moderate cellular asymmetries of bound Ft and Ds, yet Ds asymmetry can be up to twofold *in vivo* [89, 91]. As suggested by Brittle et al. [91] and Ambegaonkar et al. [89], a local positive feedback mechanism could amplify the shallow expression gradient to produce observed asymmetrical distribution of Ft and Ds.

In the next section, we extend the Ft-Ds model to two spatial dimensions. We first verify whether enough polarity is obtained given a shallow Fj gradient. We then explore the effect of adding a positive feedback, representing in-*cis* or in-*trans* cooperative clustering [92, 93] to investigate whether the system becomes capable of generating sufficient polarisation.

5.3 Modelling Ft-Ds activity in two spatial dimensions

5.3.1 Governing equations

Extending the Hale et al. [44] model into two spatial dimensions, we now consider a two-dimensional sheet of $M \times N$ hexagonal cells, as described in Chapter 4 (see Fig. 4.1). Let $F^m_{i,j}$, $S^m_{i,j}$, $\tilde{F}^m_{i,j}$ and $\tilde{S}^m_{i,j}$ denote the concentrations of Ft and Ds proteins and their phosphorylated copies in cell (i,j), compartment $m \in \{0,1,\ldots,5\}$ at time t. The monomers F and S and their phosphorylated copies $\tilde{F}$ and $\tilde{S}$ bind and unbind across neighbouring cells to form an intercellular complexes A, B, C and D according to the set of reversible reactions

$$\tilde{F}^m_{i,j} + S^{m+3}_{i_m,j_m} \rightleftharpoons A^m_{i,j}, \tag{5.43}$$

$$\tilde{F}^m_{i,j} + \tilde{S}^{m+3}_{i_m,j_m} \rightleftharpoons B^m_{i,j}, \tag{5.44}$$

$$F^m_{i,j} + S^{m+3}_{i_m,j_m} \rightleftharpoons C^m_{i,j}, \tag{5.45}$$

$$F^m_{i,j} + \tilde{S}^{m+3}_{i_m,j_m} \rightleftharpoons D^m_{i,j}, \tag{5.46}$$

where (as in Chapter 4) superscript indices are understood to be taken mod 6, and the subscript indices (i_m, j_m) transform (i,j) to neighbouring indices in a way that depends on the value of m, as follows:

$$(i_m, j_m) = \begin{cases} (i, j+1) & \text{if } m = 0 \\ (i+1, j+(i+1) \bmod 2) & \text{if } m = 1 \\ (i+1, j-i \bmod 2) & \text{if } m = 2 \\ (i, j-1) & \text{if } m = 3 \\ (i-1, j-i \bmod 2) & \text{if } m = 4 \\ (i-1, j+(i+1) \bmod 2) & \text{if } m = 5 \end{cases} \tag{5.47}$$

Monomers are also allowed to diffuse between neighbouring sides of each cell according to the 'reactions'

$$F^m_{i,j} \rightleftharpoons F^{m\pm1}_{i,j}, \tag{5.48}$$

$$\tilde{F}^m_{i,j} \rightleftharpoons \tilde{F}^{m\pm1}_{i,j}, \tag{5.49}$$

$$S^m_{i,j} \rightleftharpoons S^{m\pm1}_{i,j}, \tag{5.50}$$

$$\tilde{S}^m_{i,j} \rightleftharpoons \tilde{S}^{m\pm1}_{i,j}, \tag{5.51}$$

for $i \in \{0,\dots,M-1\}$, $j \in \{0,\dots,N-1\}$, and $m \in \{0,\dots,5\}$. As in the 1D model, we assume that the reactions (5.43)–(5.51) proceed with a forward rate constant k_i, and a backward rate constant v_i, where $i \in \{a,b,c,d\}$, depending on the corresponding complex type. In addition, we assume that Ft and Ds and their phosphorylated copies diffuse between cell compartments with diffusion rates δ_F, $\delta_{\tilde{F}}$, δ_S and $\delta_{\tilde{S}}$, respectively. We also assume that the forward rates are modified to be monotonically increasing functions, denoted by $\mathscr{K}$ and depend on the concentration of the complex on the opposite orientation.

Using the Law of Mass Action, reactions (5.43)–(5.51) are converted into an ordinary differential equation (ODE) system for cell (i,j). The full system of equations is thus given by

$$\begin{aligned}\frac{dF^m_{i,j}}{dt} &= -k_c\mathscr{K}(C^m_{i,j})F^m_{i,j}S^{m+3}_{i_m,j_m} + v_cC^m_{i,j} - k_d\mathscr{K}(D^m_{i,j})F^m_{i,j}\tilde{S}^{m+3}_{i_m,j_m} \\ &\quad + v_dD^m_{i,j} + \delta_F(F^{m-1}_{i,j} - 2F^m_{i,j} + F^{m+1}_{i,j}),\end{aligned} \tag{5.52}$$

$$\begin{aligned}\frac{d\tilde{F}^m_{i,j}}{dt} &= -k_a\mathscr{K}(A^m_{i,j})\tilde{F}^m_{i,j}S^{m+3}_{i_m,j_m} + v_aA^m_{i,j} - k_b\mathscr{K}(B^m_{i,j})\tilde{F}^m_{i,j}\tilde{S}^{m+3}_{i_m,j_m} \\ &\quad + v_bB^m_{i,j} + \delta_{\tilde{F}}(\tilde{F}^{m-1}_{i,j} - 2\tilde{F}^m_{i,j} + \tilde{F}^{m+1}_{i,j}),\end{aligned} \tag{5.53}$$

$$\begin{aligned}\frac{dS^m_{i,j}}{dt} &= -k_c\mathscr{K}(C^{m+3}_{i_m,j_m})F^{m+3}_{i_m,j_m}S^m_{i,j} + v_cC^{m+3}_{i_m,j_m} - k_a\mathscr{K}(A^{m+3}_{i_m,j_m})\tilde{F}^{m+3}_{i_m,j_m}S^m_{i,j} \\ &\quad + v_aA^{m+3}_{i_m,j_m} + \delta_S(S^{m-1}_{i,j} - 2S^m_{i,j} + S^{m+1}_{i,j}),\end{aligned} \tag{5.54}$$

$$\begin{aligned}\frac{d\tilde{S}^m_{i,j}}{dt} &= -k_d\mathscr{K}(D^{m+3}_{i_m,j_m})F^{m+3}_{i_m,j_m}\tilde{S}^m_{i,j} + v_d D^{m+3}_{i_m,j_m} - k_b\mathscr{K}(B^{m+3}_{i_m,j_m})\tilde{F}^{m+3}_{i_m,j_m}\tilde{S}^m_{i,j} \\ &\quad + v_b B^{m+3}_{i_m,j_m} + \delta_{\tilde{S}}(\tilde{S}^{m-1}_{i,j} - 2\tilde{S}^m_{i,j} + \tilde{S}^{m+1}_{i,j}),\end{aligned} \tag{5.55}$$

$$\frac{dA^m_{i,j}}{dt} = k_a\mathscr{K}(A^m_{i,j})\tilde{F}^m_{i,j}S^{m+3}_{i_m,j_m} - v_a A^m_{i,j}, \tag{5.56}$$

$$\frac{dB^m_{i,j}}{dt} = k_b\mathscr{K}(B^m_{i,j})\tilde{F}^m_{i,j}\tilde{S}^{m+3}_{i_m,j_m} - v_b B^m_{i,j}, \tag{5.57}$$

$$\frac{dC^m_{i,j}}{dt} = k_c\mathscr{K}(C^m_{i,j})F^m_{i,j}S^{m+3}_{i_m,j_m} - v_c C^m_{i,j}, \tag{5.58}$$

$$\frac{dD^m_{i,j}}{dt} = k_d\mathscr{K}(D^m_{i,j})F^m_{i,j}\tilde{S}^{m+3}_{i_m,j_m} - v_d D^m_{i,j}. \tag{5.59}$$

Similar to Section 5.2, the total (bound and unbound) concentrations of both phosphorylated and unphosphorylated Ft and Ds are conserved in each cell:

$$F_T = \sum_{m=0}^{5}\left(F^m_{i,j} + C^m_{i,j} + D^m_{i,j}\right), \tag{5.60}$$

$$\tilde{F}_T = \sum_{m=0}^{5}\left(\tilde{F}^m_{i,j} + A^m_{i,j} + B^m_{i,j}\right), \tag{5.61}$$

$$S_T = \sum_{m=0}^{5}\left(S^m_{i,j} + A^m_{i,j} + D^m_{i,j}\right), \tag{5.62}$$

$$\tilde{S}_T = \sum_{m=0}^{5}\left(\tilde{S}^m_{i,j} + B^m_{i,j} + D^m_{i,j}\right), \tag{5.63}$$

for positive constants F_T, $\tilde{F}_T$, S_T and $\tilde{S}_T$. As discussed in Section 5.1, the Ft-Ds polarisation is then readout via differences in the levels of total bound Ft and Ds on each cell edge. Mathematically, the total bound Ft and Ds on edge j of cell i, respectively are represented by

$$F_T = A^m_{i,j} + B^m_{i,j} + C^m_{i,j} + D^m_{i,j}, \tag{5.64}$$

$$S_T = A^{m+3}_{i_m,j_m} + B^{m+3}_{i_m,j_m} + C^{m+3}_{i_m,j_m} + D^{m+3}_{i_m,j_m}. \tag{5.65}$$

5.3.2 Numerical simulations

We numerically solve the system (5.52)–(5.59) for a two-dimensional sheet of 10×10 heaxgonal cells of equal size, each with six compartments, numerically using a variable-step, variable-order method (implemented using the function `odeint` from `scipy.integrate` in Python). Unless otherwise stated, we use the same parameter values and modelling assumptions described in Section 5.2, and assume that the Fj gradient is aligned with the x axis. We use a similar strategy to specifying no flux conditions on the left and right tissue boundaries, and for simplicity we impose periodicity on the top and bottom tissue boundaries.

Similar to the 1D model, we assume that initially, there are no complexes present, and unbound Ft and Ds (in both phosphorylated and unphosphorylated forms) are distributed evenly within each cell. We further assume that the fraction of Ft and/or Ds that is initially phosphorylated varies with the level of Fj activity in each cell, depending on the modelling assumption made in each simulation. Thus, the initial condition for each simulation is given by

$$F^m_{i,j}(0) = F_0(1 - p_F(i)), \tag{5.66}$$

$$\tilde{F}^m_{i,j}(0) = F_0 p_F(i), \tag{5.67}$$

$$S^m_{i,j}(0) = S_0(1 - p_S(i)), \tag{5.68}$$

$$\tilde{S}^m_{i,j}(0) = S_0 p_S(i), \tag{5.69}$$

$$A^m_{i,j}(0) = 0, \tag{5.70}$$

$$B^m_{i,j}(0) = 0, \tag{5.71}$$

$$C^m_{i,j}(0) = 0, \tag{5.72}$$

$$D^m_{i,j}(0) = 0, \tag{5.73}$$

for $i \in \{0,\dots M-1\}$, $j \in \{0,\dots,N-1\}$, and $m \in \{0\dots,5\}$, and we assume the following linear forms for the Fj activity gradient [44]:

$$p_F(i) = \begin{cases} \dfrac{p_0 + i\Delta}{p_0 + N\Delta} & \text{if Fj acts on Ft} \\ 1 & \text{if Fj does not act on Ft,} \end{cases} \tag{5.74}$$

$$p_S(i) = \begin{cases} \dfrac{p_0 + i\Delta}{p_0 + N\Delta} & \text{if Fj acts on Ds} \\ 1 & \text{if Fj does not act on Ds,} \end{cases} \tag{5.75}$$

As in Section 5.2.2, we use parameter values $p_0 = 80$, $\Delta = 10$, $F_0 = S_0 = 50$ in our numerical simulations unless stated otherwise. For simulations where stabilising feedback is present, we use the same functional form as in Chapters 3 and 4, namely

$$\mathscr{K}(c) = 1 + \frac{(\mu - 1)c^m}{\rho^m + c^m}, \tag{5.76}$$

where $m = 2$, $\rho = 1$ and μ is specified in each simulation below.

We begin by checking whether the system evolves to a SUSS in the absence of feedback and Fj gradient. Fig. 5.4 shows that the bound Ft and Ds do indeed reach stable unpolarised steady states in the absence of a Fj gradient activity. Note that the extreme concentrations on the cells further to the right and left of the tissue are due to boundary effects.

We next explore the case where there is no feedback ($\mathscr{K} = 1$) and Fj acts to phosphorylate either Ft or Ds. Fig. 5.5a and Fig. 5.5b show the total bound Ds and Ft, respectively, in the case where Fj phosphorylates only Ft, while Fig. 5.5c and Fig. 5.5d show the case where Fj acts to phosphorylate only Ds. In all of the cases of Fig. 5.5, we suppose that Fj activity starts low at the proximal edge and increases by 10% towards the distal edge of the tissue. The average total polarity between the proximal and distal cell edges in the bound Ft and Ds for the first row of Fig. 5.5 is approximately 0.3%, and 0.4% for the second row. A shallow

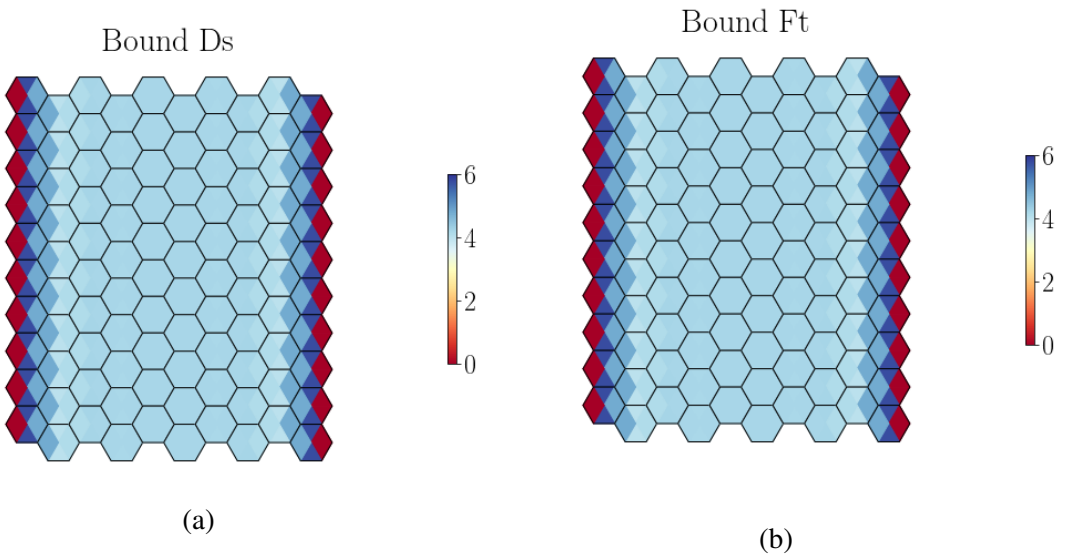

Fig. 5.4 Numerical solution of the 2D Ft-Ds model (5.52)–(5.59) with initial condition (5.66)–(5.73) and no-flux conditions on the left and right boundary and periodicity on the upper and lower boundary, in the absence of a Fj gradient. (a) total bound Ds on each cell edge (5.65); (b) total bound Ft on each cell edge (5.64). Association constants are given in Table 5.1. Other non-dimensional parameter values are $\delta_F = \delta_{\tilde{F}} = \delta_S = \delta_{\tilde{S}} = 10$. Numerical solution shown at $t = 20$.

gradient of Fj on either Ft or Ds shows very weak proximal polarity on Ft and distal polarity on Ds in the interior cells with an average of 0.3% between the proximal and distal cell edges. Increasing the steepness of Fj activity (from 10% to 30%) slightly improves polarity by 0.1% (results are not shown). However, Fj phosphorylation of both Ds and Ft results in a stronger polarity across the tissue with an average of 1.2% (Fig. 5.6). The average polarity within each cell is 0.8% (Fig. 5.6a–5.6b) and 1.2% (Fig. 5.6c–5.6d), which is still weak compared to the expected polarisation strength observed experimentally (two-fold asymmetry in Ds distribution) [91].

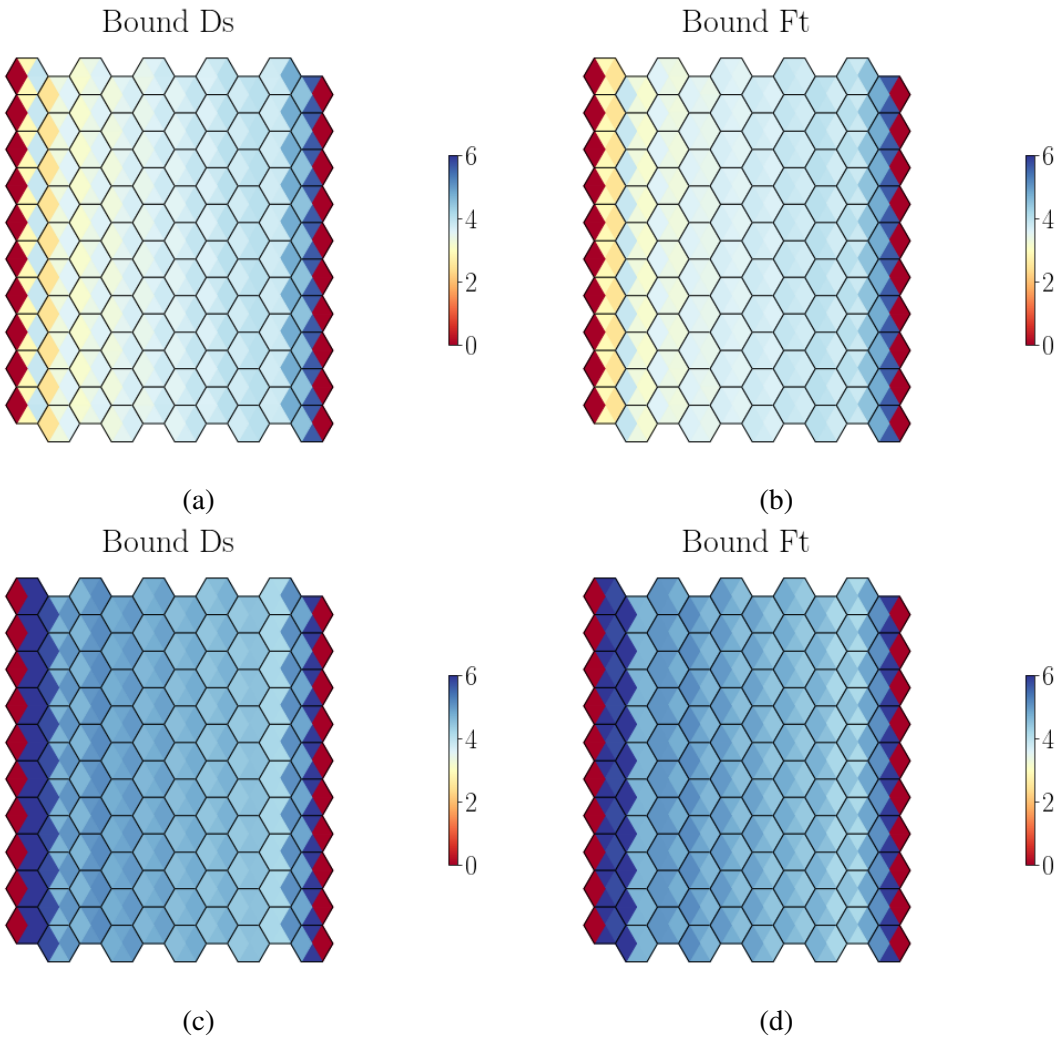

Fig. 5.5 Numerical solution of the 2D Ft-Ds model (5.52)–(5.59) with initial condition (5.66)–(5.73) and no-flux conditions on the left and right boundary and periodicity on the upper and lower boundary, in the presence of a 10% tissue gradient in Fj activity, with Fj acting (a, b) only on Ft or (c, d) only on Ds. (a, c) total bound Ds on each cell edge (5.65); (b, d) total bound Ft on each cell edge (5.64). Association constants are given in Table 5.1. Other non-dimensional parameter values are $\delta_F = \delta_{\tilde{F}} = \delta_S = \delta_{\tilde{S}} = 10$. Numerical solution shown at $t = 20$.

We next examine the behaviour of the model using association rates that are modified to reflect Fj having a dominant effect on Ft [44]. We observe a weak asymmetry in the Ft/Ds localisation if Fj is allowed to phosphorylate either Ft or Ds with an average polarity of 0.3% (results not shown). If Fj is allowed to phosphorylate both Ft and Ds, the polarisation slightly improves, with an average of 0.6% (results are not shown), but is still weak. Increasing the Fj gradient further to 50% results in an average polarity of 1.3%.

We next explore how stabilising feedback interactions may improve tissue-scale polarisation. We suppose that the higher concentration of a certain complex on one orientation between two neighbouring cells is, the slower the reverse reaction proceeds in the opposite orientation. Results for the case of a Fj gradient acting on both Ft and Ds, with different feedback assumptions, are shown in Fig. 5.7. In Fig. 5.7a and Fig. 5.7b, we assume that the stabilising feedback depends on how much complex of the same type there is in a particular cell edge. We observe an improvement in the average tissue polarity of 1.7%. In Fig. 5.7c and Fig. 5.7d, we suppose that the feedback depends on the total complex present on the same orientation of Ft and the opposite orientation for Ds. In this case, we obtain an average polarity of 1.5%. If Fj is allowed to phosphorylate either Ft or Ds, weak feedback ($\mu = 3$) suffices to generate stronger polarisation (than seen on Fig. 5.5 without feedback) with an average of 0.7% (results not shown). Simulations using modified association rates with Fj having a dominant effect on Ft show an average polarity of 0.9% in the total bound Ft and Ds, if allowing a Fj gradient of 30% steep and weak feedback ($\mu = 2$; results not shown). Consequently, neither a steeper gradient nor a stronger feedback predicts stronger polarisation in this case.

Overall, our results suggest that the existence of a weak local positive feedback slightly improves the overall polarisation of the system. The highest average polarity that we observe in the total bound Ft and Ds is about 5.2% in the case of a Fj steepness of 50% and a feedback

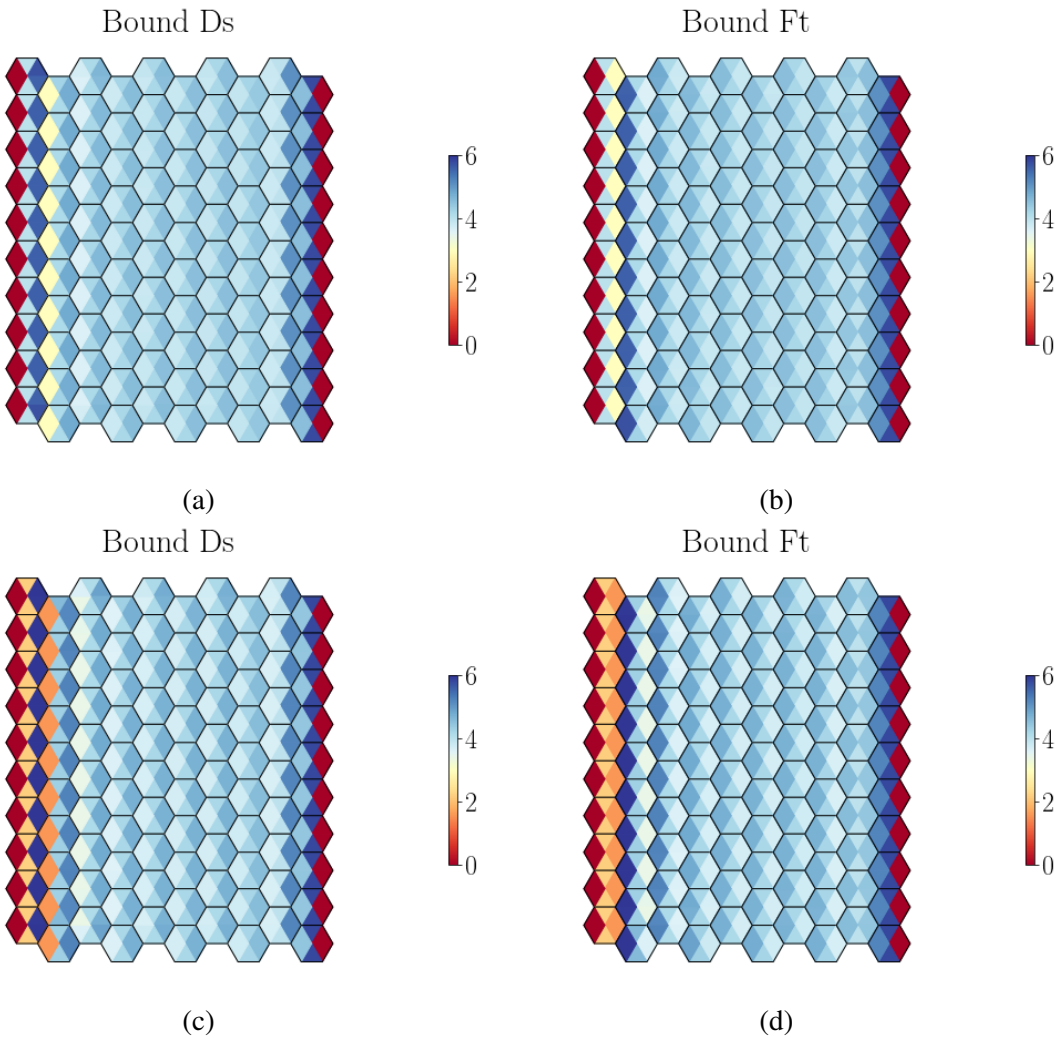

Fig. 5.6 Numerical solution of the 2D Ft-Ds model (5.52)–(5.59) with initial condition (5.66)–(5.73) and no-flux conditions on the left and right boundary and periodicity on the upper and lower boundary, in the presence of a (a-b) 10% or (c-d) 30% tissue gradient in Fj activity, with Fj acting on both Ft and Ds. (a, c) total bound Ds on each cell edge (5.65); (b, d) total bound Ft on each cell edge (5.64). Association constants are given in Table 5.1. Other non-dimensional parameter values are $\delta_F = \delta_{\tilde{F}} = \delta_S = \delta_{\tilde{S}} = 10$. Numerical solution shown at $t = 20$.

strength $\mu = 10$ (result is not shown). In this case, the obtained tissue gradient rises up to 14% in the total bound Ds and 6.4% in the total bound Ft.

5.4 Discussion

Several mechanisms are thought to affect planar polarisation during development. In particular, the coordination of cellular polarisation along a tissue axis is tightly regulated by an upstream 'global cue' [18]. Through such regulation, hundreds of cells in epithelial sheets become planar polarised. However, the source of such a global cue and how it is interpreted at a molecular level, is still not well understood. One particular challenge is to determine potential mechanisms by which a gradient is sensed across the tissue by individual cells, ultimately resulting in uniform planar polarity across the tissue. In this chapter, we have extended an existing one-dimensional model of the Ft-Ds planar polarity pathway in the developing fly wing [44] to two spatial dimensions, and have examined the hypothesised mechanism of a local positive interaction, in addition to a shallow Fj gradient, in driving planar polarisation.

Our simulation results show that the system evolves to a stable unpolarised steady state in the absence of feedback amplification or a tissue-scale of Fj activity (and hence of Ft or Ds phosphorylation). In the absence of any feedback amplification, a linear gradient of Fj activity is sufficient to recapitulate experimentally observed Ft-Ds patterns. This result elevates the importance of the distal gradient of Fj along the tissue plane to attain asymmetric localisation of the Ft-Ds heterodimer [44, 87], which consequently drives polarisation across the tissue. Nevertheless, the relative tissue gradients obtained in our simulations under these assumptions did not predict the experimentally observed distribution of Ds across the cell axis, which is found to be about twofold [91]. We therefore modified the model to include a nonlinear feedback that amplifies Ft and Ds binding.

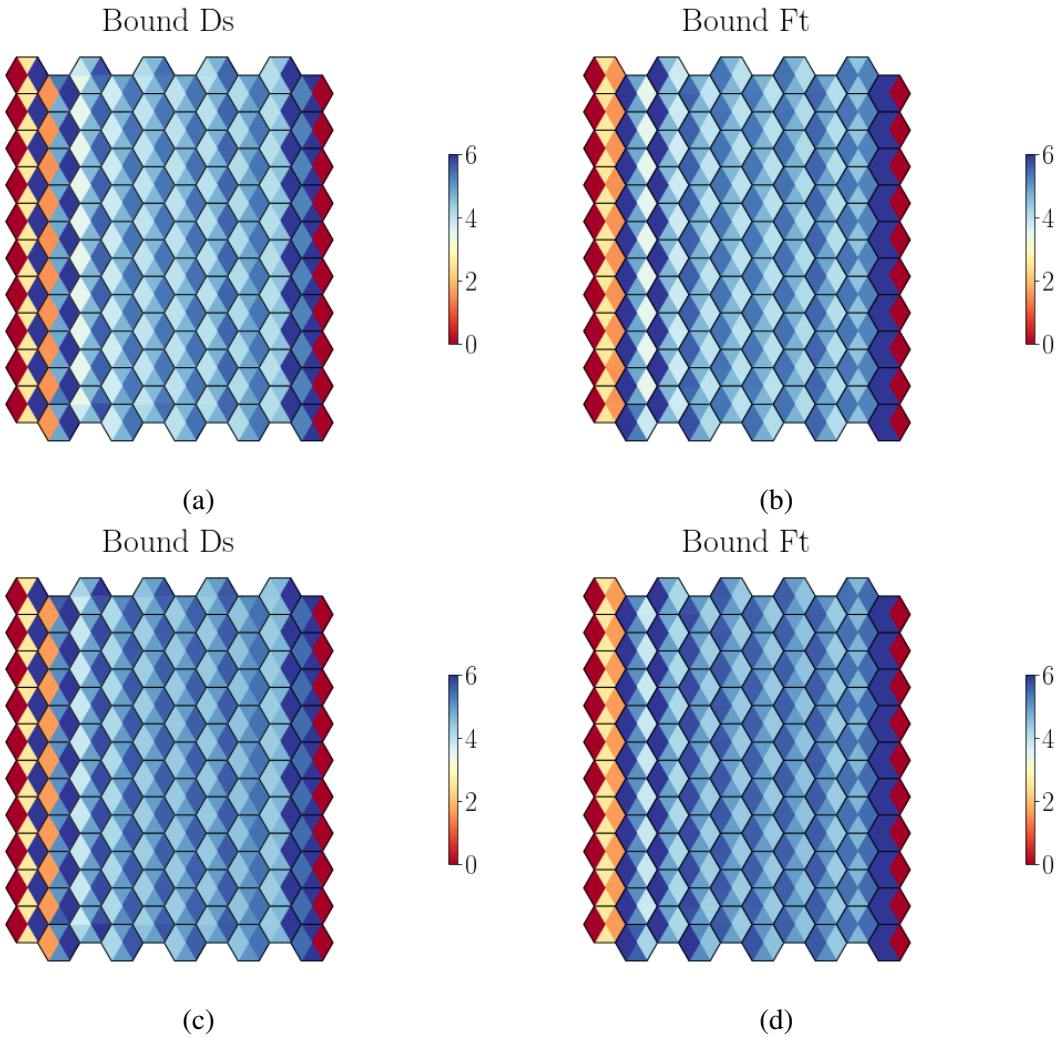

Fig. 5.7 Numerical solution of the 2D Ft-Ds model (5.52)–(5.59) with initial condition (5.66)–(5.73) and no-flux conditions on the left and right boundary and periodicity on the upper and lower boundary, in the presence of a 30% tissue gradient in Fj activity, with Fj acting on both Ft and Ds, with an additional stabilising feedback interaction of strength $\mu = 2$ that depends (a-b) how much of the complex there is of the same type or (c-d) how much of the complex involving Ft or Ds there is on the corresponding edge. (a, c) total bound Ds on each cell edge (5.65); (b, d) total bound Ft on each cell edge (5.64). Association constants are given in Table 5.1. Other non-dimensional parameter values are $\delta_F = \delta_{\tilde{F}} = \delta_S = \delta_{\tilde{S}} = 10$. Numerical solution shown at $t = 20$.

Recent theoretical models of the Ft-Ds system suggest that the stability of Ft-Ds heterodimers depend on the local concentrations of Ft and Ds on opposing cell junctions [88]. Such local interactions may then occur within each cell or between neighbouring cells [81]. Here, we considered two possible mechanisms of stabilising feedback. In the first case, we assumed that feedback strength depends on the concentration of the corresponding complex in the opposite orientation. In the second case, we assumed that feedback strength instead depends on the total amount of the corresponding complex in the opposite orientation. The resulting simulations suggest that Ft-Ds polarity establishment may require a potential asymmetrical distribution of Ft and Ds via a graded tissue-level activity of Fj, which is then amplified by weakly positive feedback. These results appear to support recent experimental findings reached by Brittle et al. [81].

A natural avenue for future work in this area is to investigate *in silio* the effect of different mutant clones on Ft-Ds polarity in surrounding wild-type cells within the fly wing. For instance, ft mutant clones have been shown experimentally to exhibit marked swirls [94], with similar phenotypes observed in the absence of Fj gradient expression [88, 95] given a weak global polarity input and a local protein distribution. There is also significant scope for exploring the mechanisms underlying the upstream generation of a Fj gradient and the possible role of a moving boundary of Ds expression at the tissue boundary [91] as an additional global cue, as well as the downstream regulation by planar polarised Ft and Ds of cell growth and mechanics [17]. We discuss this further, and summarise the overall contributions made in this thesis, in the next chapter.

Chapter 6

Discussion

The patterning of multicellular tissues is essential for the formation of the organs that make up our bodies. It relies on self-organisation, which emerges from dynamic, iterative interactions between components from molecular to cellular to tissue levels. Alongside experimental approaches, mathematical modelling can help us to unravel such complexity, by testing sufficiency of proposed patterning mechanisms under normal conditions and/or generating experimentally testable predictions of behaviour under perturbed conditions.

In this thesis we have used mathematical modelling to investigate aspects of patterning from the molecular to the tissue scale, motivated by recent experimental observations related to three biological exemplars: (i) the clustering of E-cadherin protein complexes underlying cell-cell adhesion; (ii) the presence of amplifying feedback interactions underlying 'core' planar polarity; (iii) the relative contributions of such feedback interactions and graded global cues underlying Fat-Dachsous planar polarity. In this chapter we summarise our scientific contributions, highlight the strengths and limitations of our research, and discuss avenues for future work.

6.1 Turing and wave-pinning mechanisms of protein complex clustering

Tissue-scale polarity emerges, in part, from the self-organised spatial patterning of intercellular protein complexes [5, 47]. In Chapter 2 we used reaction-diffusion modelling to investigate how transmembrane homodimers, an abstraction of cell-cell adhesion complexes, may become locally clustered within cell-cell junctions. Our analysis of the mass conserved model revealed that pattern formation can occur, given a sufficiently strong stabilising feedback on local complex formation, and/or sufficiently high total protein concentration in the system. While the conservative model exhibits multiple (meta)stable punctate regions within a range of parameter values, we found that breaking the mass conservation via protein trafficking fails to recapitulate stable complex clustering.

Existing mathematical models of mass-conserved reaction-diffusion systems vary in the way that positive feedback mechanisms are formulated. However, they agree on the requirement of such a feedback to obtain patterning. One set of models exhibit 'peak' formation via a Turing instability [25, 48, 59]. Depending on how large the domain size is relative to a characteristic wavelength, these models can generate one or more peaks from an initial condition that is close to homogeneous [15, 50]. However, even when multiple peaks emerge, most of the smaller peaks eventually disappear through 'competition', ending with a single large peak. This behaviour is thought to be due to the mass conservation property [59]. In another set of models, patterns arise comprising spatial subdomains with spatially uniform solutions connected by a 'wave-front', producing 'wave-pinning' behaviour [25].

Our numerical results when mass conservation is broken may be related to other theoretical analysis by Verschueren and Champneys [96], who explore the patterns arising in a variant of a Schnackenberg reaction-diffusion model in the limit of mass conservation. Through bifurcation and multiple-scale asymptotic analysis, these authors find that in the

singular limit corresponding to mass conservation, localised regions become filled with spike solutions that tend to wave-pinned fronts.

A biological motivation for our work in this chapter has been E-cadherin cluster formation [4]. In our abstracted model, initial concentration fluctuations always generate a single spike or mesa, depending on the type of feedback. For a sufficiently high total protein concentration, however, our conserved system exhibits multiple (meta)stable peaks within the domain. In the case of saturating feedback, the size of our simulated 'clusters' may be related to the total protein concentration and other model parameters. It is interesting to compare this behaviour with the results of Quang et al. [4], whose E-cadherin data suggests a truncated power-law cluster size distribution. The emergence of such a distribution is likely to emerge in part from the activity of key cortical regulators, coupling E-cadherin/actin with endocytosis (corresponding to 'degradation' in our non-conservative model). In addition, for simplicity our model considers only protein dimerisation and neglects higher order complexes, which observations suggest E-cadherin can form [4].

An obvious avenue for future work is to extend our model to account for higher-order protein complexes. Another natural extension is to generalise to more than one molecular species, as we have considered in Chapters 3–5, and apply our modelling approach to investigate possible mechanisms underlying the spatial clustering of core pathway protein complexes [47]. Finally, we acknowledge a 'missing length scale' between our modelling in Chapter 2 and Chapter 3, which is the emergence of cell-scale patterning due to the coordination of molecular interactions across an individual cell. We have not focused on bridging that length scale in this thesis, as it is arguably the most technically challenging, for example in terms of requiring 1D reaction-diffusion systems defined at each cell-cell junction to a 2D reaction-diffusion system defined in the cell bulk. Nevertheless, such coupling is likely to provide fertile ground for future modelling efforts.

6.2 Feedback requirements for cell-to-tissue scale planar polarity

Moving up to the cell-to-tissue scale, in Chapter 3 we developed and analysed three minimal models of transmembrane heterodimer formation and intracellular trafficking in a one-dimensional ring of cells. This work was inspired in part by a recent detailed computational model of the core pathway in the fly wing by Fisher et al. [63], and extends upon that work by considering different hypothesised mechanisms of nonlinear feedback interactions that could act to amplify small initial biases in this system and generate planar polarisation.

In the absence of feedback, we found a unique positive spatially uniform steady state (SUSS) in each of our models, which is stable to spatially homogeneous perturbations. Hence, patterning cannot occur in the absence of feedback. However, in the presence of feedback, bifurcation and linear stability analysis proved the existence of a critical feedback strength above which the SUSS loses stability, and the system becomes planar polarised. For fixed parameter values within this bistable regime, simulation results revealed that the polarised steady state depends on the choice of initial condition. Numerical simulations of mutant clones revealed that the range of domineering non-autonomy in neighbouring cells depends on both feedback strength and the mutation: single clones showed non-autonomy phenotype, while double clones showed either weak or no non-autonomy, in line with recent experimental observations of planar polarity in the fly wing [63].

In the case where feedback acts upon protein binding and trafficking, our simulations exhibited some period two patterns in the concentration of unbound proteins. This was also found in a more abstract planar polarity model by Schamberg et al. [69], who show that sufficiently weak diffusion and strong feedback strength are enough to generate period two patterns given inhomogeneous initial conditions. We also observed period two patterns around double clones with stabilising feedback in our other two models. Period two patterns

were previously observed by Fisher et al. [63] in Fmi^{-} mutant tissues where stabilising feedback acts on both Fz and Vang. This is an interesting behaviour that requires further investigation.

In the present work, we have abstracted much of the known biochemical details of the core planar polarity pathway and its key molecular players. This was deliberate: our intention was to allow some mathematical analysis, and focus on the essential 'rules' governing different forms of feedback in generalising planar polarity patterning. In comparison to the published work of Fisher and Strutt [97], which focuses on the initial interpretation of the graded cue to guide asymmetry in complex formation, our simplified approach allows us to take a simple system, apply different types of feedback interactions and compare how they are interpreted at the molecular level to drive wild-type and mutant polarity.

An obvious avenue for future modelling work is to revisit the more complex model of Fisher et al. [63] in the light of our results, and explore alternate feedback mechanisms. Of course, another next step is to consider whether certain experimental perturbations of core pathway activity could help to test our model predictions, such as the requirement for an 'intermediate' feedback sharpness for polarisation to occur; relating experiments to model predictions will become more straightforward as additional biochemical detail is added to our models.

6.3 Moving from one to two spatial dimensions

In Chapter 4 we extended the feedback models proposed in Chapter 3 to two spatial dimensions. We showed analytically that in the absence of feedback, the SUSS remains stable, and we also explored the occurrence of other forms of pattern. These results were supplemented by a detailed numerical exploration of the model behaviour, included planar polarisation in normal and perturbed tissue, in a static hexagonal cell packing.

Our results on the stability of different types of pattern in this model are consistent with previous models [38, 79]. Simulations with strong feedback do not show distal-vertex polarisation along the tissue, instead they evolving to a stable 'side' polarised steady state. This suggests that sufficiently strong feedback is needed for polarisation provided there is an initial imbalance between the proximal and distal ends of the cell. Hence, while the global cue is important to establish and direct polarity, feedback controls the polarisation's strength [71, 81]. In the fly wing, each cell has an initial distribution of Fz, with a slight proximal-distal bias. Intracellular interactions then drive both Fz and Vang complexes to accumulate towards distally, which result in the observed 'vertex' polarisation. Our modelling suggests that an analogous vertex steady state arises only from a *symmetric* initial condition along the x-axis; however, the vertex steady state is unstable. One possible mechanism to obtain stable vertex polarisation in the core system is to introduce an additional global bias. Experimental evidence of the core pathway in the fly wing suggests that such a global bias may be required to orient the direction of polarity [81].

Simulations of mutant clones in our 2D model recapitulated the aforementioned behaviour of domineering non-autonomy [38, 98]. Relating this to the core pathway, wild-type cells surrounding clones lacking Fz polarise towards the clone, while clones overexpressing Fz induce cells to polarise away from the clone. The situation is reversed in the case of Vang clones. This is also observed in previous planar polarity models [38, 63, 99].

A key difference between our 2D simulation results and those obtained in Chapter 3 is the occurrence of 'swirling' patterns in cells surrounding mutant clones. This form of behaviour has been observed experimentally in fly wings with single mutant clones in which either Fz [100] or Pk [101] function is lost. Swirling patterns have been also observed in fly wings around clones lacking the activity of both Fz and Vang [63]. The Ft-Ds pathway system also shows this type of behaviour [102, 103] (see Chapter 5 and Section 6.4). In this work, we observed swirling patterns in double clones for sufficiently strong stabilising feedback and in

the absence of an initial cue. Note that using the same form of feedback, we observed period two patterns in our 1D model.

Many of the proposed extensions discussed in Section 6.2 also apply to our 2D modelling work. An additional natural avenue for future work is to consider different static cell packings, reflecting more or less well ordered epithelial tissues. In our two-dimensional models, we have assumed that all cells within the tissue have a hexagonal shape, for simplicity and also motivated by the experimental observation that the fly wing comprises a hexagonal array of epithelial cells. However, other planar polarised tissues exhibit different cell packings, and indeed experimental observations suggest that cell packing may affect the propagation of polarity in the fly wing [104]. Beyond static cell packings, one could also consider a dynamic tissue that undergoes planar polarisation in the presence of cell flows [10], which could be amenable to simulation using cell-based models such as the vertex model [105].

6.4 Feedbacks and global cues in the Ft-Ds pathway

In Chapter 5 we considered a more detailed model of a planar polarity pathway: the Fat-Dachsous (Ft-Ds) pathway. This model was inspired by a one-dimensional computational model of the Ft-Ds system in the fly wing by Hale et al. [44], which included an 'upstream' gradient of Fj activity across the tissue. The main findings of that model are in agreement with more recent work, including a continuum model of two generic proteins that suggests that tissue-scale expression gradients play an important rule in stable polarisation [106]. However, local feedback interactions are neglected in these works.

We first confirmed the one-dimensional results of the model by Hale et al. [44], then extended it into two spatial dimensions using our framework developed in Chapter 4, with the aim of exploring the possible relative contributions of feedback interactions along with the Fj activity gradient in driving tissue-scale polarisation in the Ft-Ds pathway.

Our numerical simulations suggest that in the absence of a Fj activity gradient and feedback interactions, the system fails to polarise, instead evolving to a SUSS. When Fj is allowed to phosphorylate Ft and/or Ds in our simulations, thus altering their binding affinities [42, 43], we observed weak proximal polarity on Ft and a distal polarity on Ds. Nevertheless, the presence of a weak positive feedback improved the overall planar polarisation.

These theoretical findings raise the question as to the nature of possible local feedback interactions in the Ft-Ds pathway. Recent experimental findings by the Strutt lab (School of Biosciences, University of Sheffield) suggest that such interactions serve to locally stabilise Ft-Ds complexes of the same orientations, at least within puncta [81]. This supports the hypothesis that there exists a comparable combination of in-*cis* and in-*trans* clustering in the local concentrations of Ft and Ds. Here, we have investigated two potential mechanisms of local stabilising feedback: the first based on heterodimer stability depending how much complex there is in the apposing edge of the neighbouring cell; and the second based on the concentration of complexes involving both Ft and Ds on the corresponding edge. Our simulation results suggest that both forms of hypothesised feedback can improve the overall tissue-scale polarity.

There is also significant scope for extending our present analysis to include the predicted phenotypes associated with various clones and other genetic perturbations, and then testing these model predictions experimentally. Other natural avenues for future work in this area include more detailed modelling of the processes downstream of Ft-Ds polarisation, in particular the possible interplay of growth and mechanics [17].

6.5 Conclusions

In this thesis we have constructed and analysed a suite of mathematical models to study mechanisms underlying molecular to tissue scale pattern formation. Our theoretical findings

have implications for biological processes ranging from the clustering of cell-cell adhesion proteins to core and Ft-Ds pathway planar polarisation in the developing fly wing.

A longer term aim is to further bridge the spatial and temporal scales between our models, arriving at a truly multiscale description of emergent tissue-scale polarisation. With advances in biophysical techniques such as single molecule imaging, there will be greater availability of data at each scale with which to constrain and test such a model in a quantitative manner. Nevertheless, we anticipate that simple, abstracted models of the form favoured in this thesis will continue to offer an attractive, useful and complementary approach in aiding our mechanistic understanding of biological pattern formation in health and disease.

References

[1] D.W. Thompson. *On growth and form*. Cambridge University Press, 1917.

[2] A.M. Turing. The chemical basis of morphogenesis. *Bull. Math. Biol.*, 52(1):153–197, 1990. doi: 10.1007/BF02459572.

[3] St. Werner, H.T. Vu, and J.C. Rink. Self-organization in development, regeneration and organoids. *Curr. Opin. Cell Biol.*, 44:102–109, 2017. doi: 10.1016/j.ceb.2016.09.002.

[4] B. Quang, M. Mani, O. Markova, T. Lecuit, and P. Lenne. Principles of E-cadherin supramolecular organization in vivo. *Curr. Biol.*, 23(22):2197–2207, 2013. doi: 10.1016/j.cub.2013.09.015.

[5] H. Strutt, J. Gamage, and D. Strutt. Robust asymmetric localization of planar polarity proteins is associated with organization into signalosome-like domains of variable stoichiometry. *Cell Rep.*, 17(10):2660–2671, 2016. doi: 10.1016/j.celrep.2016.11.021.

[6] J.L. Maître and C.P. Heisenberg. Three functions of cadherins in cell adhesion. *Curr. Biol.*, 23(14):R626–R633, 2013. doi: 10.1016/j.cub.2013.06.019.

[7] Y. Wu, P. Kanchanawong, and R. Zaidel-Bar. Actin-delimited adhesion-independent clustering of E-cadherin forms the nanoscale building blocks of adherens junctions. *Dev. Cell*, 32(2):139–154, 2015. doi: 10.1016/j.devcel.2014.12.003.

[8] S. Hong, R.B. Troyanovsky, and S.M. Troyanovsky. Binding to F-actin guides cadherin cluster assembly, stability, and movement. *J. Cell Biol.*, 201(1):131–143, 2013. doi: 10.1083/jcb.201211054.

[9] H. Strutt, S. Warrington, and D. Strutt. Dynamics of core planar polarity protein turnover and stable assembly into discrete membrane subdomains. *Dev. Cell*, 20(4): 511–525, 2011. doi: 10.1016/j.devcel.2011.03.018.

[10] B. Aigouy, R. Farhadifar, D.B. Staple, A. Sagner, J.C. Röper, F. Jülicher, and S. Eaton. Cell flow reorients the axis of planar polarity in the wing epithelium of Drosophila. *Cell*, 142(5):773–786, 2010. doi: 10.1016/j.cell.2010.07.042.

[11] B. Cho, Pierre L., A. Sagner, S. Eaton, and J. Axelrod. Clustering and negative feedback by endocytosis in planar cell polarity signaling is modulated by ubiquitinylation of prickle. *PLoS Genet.*, 11(5):e1005259, 2015. doi: 10.1371/journal.pgen.1005259.

[12] R. Li and B. Bowerman. Symmetry breaking in biology. *Cold Spring Harb. Perspect. Biol.*, 2(3):a003475, 2010. doi: 10.1101/cshperspect.a003475.

[13] H. Strutt and D. Strutt. Asymmetric localisation of planar polarity proteins: Mechanisms and consequences. *Semin. Cell Dev. Biol.*, 20(8):957–963, 2009. doi: 10.1016/j.semcdb.2009.03.006.

[14] I. Lestas, G. Vinnicombe, and J. Paulsson. Fundamental limits on the suppression of molecular fluctuations. *Nature*, 467(7312):174–178, 2010. doi: 10.1038/nature09333.

[15] A. Gierer and H. Meinhardt. A theory of biological pattern formation. *Kybernetik*, 12 (1):30–39, 1972. doi: 10.1007/BF00289234.

[16] S. Shadkhoo and M. Mani. The role of intracellular interactions in the collective polarization of tissues and its interplay with cellular geometry. *PLoS Comput. Biol.*, 15(11):e1007454, 2019. doi: 10.1371/journal.pcbi.1007454.

[17] K.H. Fisher, D. Strutt, and A.G. Fletcher. Integrating planar polarity and tissue mechanics in computational models of epithelial morphogenesis. *Curr. Opin. Sys. Biol.*, 5:41–49, 2017. doi: 10.1016/j.coisb.2017.07.009.

[18] W.Y. Aw, B.W. Heck, B. Joyce, and D. Devenport. Transient tissue-scale deformation coordinates alignment of planar cell polarity junctions in the mammalian skin. *Curr. Biol.*, 26(16):2090–2100, 2016. doi: 10.1016/j.cub.2016.06.030.

[19] W. Aw and D. Devenport. Planar cell polarity: global inputs establishing cellular asymmetry. *Curr. Opin. Cell Biol.*, 44:110–116, 2017. doi: 10.1016/j.ceb.2016.08.002.

[20] A.R.A. Anderson and V. Quaranta. Integrative mathematical oncology. *Nat. Rev. Cancer*, 8(3):227–234, 2008. doi: 10.1038/nrc2329.

[21] H. Meinhardt and A. Gierer. Pattern formation by local self-activation and lateral inhibition. *Bioessays*, 22(8):753–760, 2000. doi: 10.1002/1521-1878(200008)22:8<753::AID-BIES9>3.0.CO;2-Z.

[22] S. Kondo and T. Miura. Reaction-diffusion model as a framework for understanding biological pattern formation. *Science*, 329(5999):1616–1620, 2010. doi: 10.1126/science.1179047.

[23] L. Marcon and J. Sharpe. Turing patterns in development: what about the horse part? *Curr. Opin. Genet. Dev.*, 22(6):578–584, 2012. doi: 10.1016/j.gde.2012.11.013.

[24] S. Kondo. An updated kernel-based Turing model for studying the mechanisms of biological pattern formation. *J. Theor. Biol.*, 414:120–127, 2017. doi: 10.1016/j.jtbi.2016.11.003.

[25] Y. Mori, A. Jilkine, and L. Edelstein-Keshet. Wave-pinning and cell polarity from a bistable reaction-diffusion system. *Biophys. J.*, 94(9):3684–3697, 2008. doi: 10.1529/biophysj.107.120824.

[26] K.H. Palmquist, S.F. Tiemann, F.L. Ezzeddine, S. Yang, C.R. Pfeifer, A. Erzberger, A.R. Rodrigues, and A.E. Shyer. Reciprocal cell-ECM dynamics generate supracellular fluidity underlying spontaneous follicle patterning. *Cell*, 185(11):1960–1973.e11, 2022. doi: 10.1016/j.cell.2022.04.023.

[27] R.S. Gray, I. Roszko, and L. Solnica-Krezel. Planar cell polarity: coordinating morphogenetic cell behaviors with embryonic polarity. *Dev. Cell*, 21(1):120–133, 2011. doi: 10.1016/j.devcel.2011.06.011.

[28] L.V. Goodrich and D. Strutt. Principles of planar polarity in animal development. *Development*, 138(10):1877–1892, 2011. doi: 10.1242/dev.054080.

[29] C. Guillot and T. Lecuit. Mechanics of epithelial tissue homeostasis and morphogenesis. *Science*, 340(6137):1185–1189, 2013. doi: 10.1126/science.1235249.

[30] M. Wang, P. de Marco, V. Capra, and Z. Kibar. Update on the role of the non-canonical Wnt/planar cell polarity pathway in neural tube defects. *Cells*, 8(10):1198, 2019. doi: 10.3390/cells8101198.

[31] H. Chen and C.Y. Cheng. Planar cell polarity (PCP) proteins and spermatogenesis. *Semin. Cell Dev. Biol.*, 59:99–109, 2016. doi: 10.1016/j.semcdb.2016.04.010.

[32] D.J. Henderson and B. Chaudhry. Getting to the heart of planar cell polarity signaling. *Birth Defects Res. A Clin. Mol. Teratol.*, 91(6):460–467, 2011. doi: 10.1002/bdra.20792.

[33] C. Tower-Gilchrist, S.A. Zlatic, D. Yu, Q. Chang, H. Wu, X. Lin, V. Faundez, and P. Chen. Adaptor protein-3 complex is required for Vangl2 trafficking and planar cell polarity of the inner ear. *Mol. Biol. Cell*, 30(18):2422–2434, 2019. doi: 10.1091/mbc.E16-08-0592.

[34] J.D. Axelrod and C.J. Tomlin. Modeling the control of planar cell polarity. *Wiley Interdiscip. Rev. Sys. Biol. Med.*, 3(5):588–605, 2011. doi: 10.1002/wsbm.138.

[35] L.L. Wong and P.N. Adler. Tissue polarity genes of Drosophila regulate the subcellular location for prehair initiation in pupal wing cells. *J. Cell Biol.*, 123(1):209–221, 1993. doi: 10.1083/jcb.123.1.209.

[36] C.R. Vinson and P.N. Adler. Directional non-cell autonomy and the transmission of polarity information by the frizzled gene of Drosophila. *Nature*, 329(6139):549–551, 1987. doi: 10.1038/329549a0.

[37] J. Taylor, N. Abramova, J. Charlton, and P.N. Adler. Van Gogh: a new Drosophila tissue polarity gene. *Genetics*, 150(1):199–210, 1998. doi: 10.1093/genetics/150.1.199.

[38] K. Amonlirdviman, N. Khare, D. Tree, W. Chen, J. Axelrod, and C. Tomlin. Mathematical modeling of planar cell polarity to understand domineering nonautonomy. *Science*, 307(5708):423–426, 2005. doi: 10.1126/science.1105471.

[39] P.A. Mahoney, U. Weber, P. Onofrechuk, H. Biessmann, P.J. Bryant, and C.S. Goodman. The fat tumor suppressor gene in Drosophila encodes a novel member of the cadherin gene superfamily. *Cell*, 67(5):853–868, 1991. doi: 10.1016/0092-8674(91)90359-7.

[40] H.F. Clark, D. Brentrup, K. Schneitz, A. Bieber, C. Goodman, and M. Noll. Dachsous encodes a member of the cadherin superfamily that controls imaginal disc morphogenesis in Drosophila. *Genes Dev.*, 9(12):1530–1542, 1995. doi: 10.1101/gad.9.12.1530.

[41] J.L. Villano and F.N. Katz. four-jointed is required for intermediate growth in the proximal-distal axis in Drosophila. *Development*, 121(9):2767–2777, 1995. doi: 10.1242/dev.121.9.2767.

[42] A.L. Brittle, A. Repiso, J. Casal, P.A. Lawrence, and D. Strutt. Four-jointed modulates growth and planar polarity by reducing the affinity of dachsous for fat. *Curr. Biol.*, 20 (9):803–810, 2010. doi: 10.1016/j.cub.2010.03.056.

[43] M.A. Simon, A. Xu, H.O. Ishikawa, and K.D. Irvine. Modulation of fat:dachsous binding by the cadherin domain kinase four-jointed. *Curr. Biol.*, 20(9):811–817, 2010. doi: 10.1016/j.cub.2010.04.016.

[44] R. Hale, A.L. Brittle, K.H. Fisher, N.A.M. Monk, and D. Strutt. Cellular interpretation of the long-range gradient of Four-jointed activity in the Drosophila wing. *eLife*, 4: e05789, 2015. doi: 10.7554/eLife.05789.

[45] Y. Mao, C. Rauskolb, E. Cho, W.-L. Hu, H. Hayter, G. Minihan, F.N. Katz, and K.D. Irvine. Dachs: an unconventional myosin that functions downstream of Fat to regulate growth, affinity and gene expression in Drosophila. *Development*, 133:2539–2551, 2006. doi: 10.1242/dev.02427.

[46] M.T. Butler and J.B. Wallingford. Planar cell polarity in development and disease. *Nat. Rev. Mol. Cell Biol.*, 18(6):375–388, 2017. doi: 10.1038/nrm.2017.11.

[47] H. Strutt, J. Gamage, and D. Strutt. Reciprocal action of Casein Kinase Iε on core planar polarity proteins regulates clustering and asymmetric localisation. *eLife*, 8: e45107, 2019. doi: 10.7554/eLife.45107.

[48] A.B. Goryachev and A.V. Pokhilko. Dynamics of Cdc42 network embodies a Turing-type mechanism of yeast cell polarity. *FEBS Lett.*, 582(10):1437–1443, 2008. doi: 10.1016/j.febslet.2008.03.029.

[49] Y. Mori, A. Jilkine, and L. Edelstein-Keshet. Asymptotic and bifurcation analysis of wave-pinning in a reaction-diffusion model for cell polarization. *SIAM J. Appl. Math.*, 71(4):1401–1427, 2011. doi: 10.1137/10079118X.

[50] J. Chiou, S. Ramirez, T. Elston, T. Witelski, D. Schaeffer, and D. Lew. Principles that govern competition or co-existence in Rho-GTPase driven polarization. *PLoS Comput. Biol.*, 14(4):e1006095, 2018. doi: 10.1371/journal.pcbi.1006095.

[51] J.C. Looney. Non-saturating amplifier theory. Master's thesis, Oregon State University, 1960.

[52] Ph. Saucez, W.E. Schiesser, and A. Vande Wouwer, editors. *Adaptive Method of Lines*. CRC Press, 2001.

[53] A. Jilkine. *A wave-pinning mechanism for eukaryotic cell polarization based on Rho GTPase dynamics*. PhD thesis, University of British Columbia, 2009.

[54] F. Brauns, J. Halatek, and E. Frey. Phase-space geometry of mass-conserving reaction-diffusion dynamics. *Phys. Rev. X*, 10(4):041036, 2020. doi: 10.1103/PhysRevX.10.041036.

[55] C. Kuehn. *PDE dynamics: an introduction*. Philadelphia: Society for Industrial and Applied Mathematics, 2019.

[56] Y. Nishiura. Global structure of bifurcating solutions of some reaction-diffusion systems. *SIAM J. Math. Anal.*, 13(4):555–593, 1982. doi: 10.1137/0513037.

[57] S.A. Rautu, G. Rowlands, and M.S. Turner. Size-dependent recycling of membrane clusters. *EPL*, 121(5):58004, 2018. doi: 10.1209/0295-5075/121/58004.

[58] A. Jilkine and L. Edelstein-Keshet. A comparison of mathematical models for polarization of single eukaryotic cells in response to guided cues. *PLOS comput. Biol.*, 7 (4):e1001121, 2011. doi: 10.1371/journal.pcbi.1001121.

[59] M. Otsuji, S. Ishihara, C. Co, K. Kaibuchi, A. Mochizuki, and S. Kuroda. A mass conserved reaction-diffusion system captures properties of cell polarity. *PLoS Comput. Biol.*, 3(6):e108, 2007. doi: 10.1371/journal.pcbi.0030108.eor.

[60] M. Cavey, M. Rauzi, P.F. Lenne, and T. Lecuit. A two-tiered mechanism for stabilization and immobilization of E-cadherin. *Nature*, 453(7196):751–756, 2008. doi: 10.1038/nature06953.

[61] T.J.C. Harris and M. Peifer. Adherens junction-dependent and-independent steps in the establishment of epithelial cell polarity in Drosophila. *J. Cell Biol.*, 167(1): 135–147, 2004. doi: 10.1083/jcb.200406024.

[62] M.C. Wigbers, F. Brauns, T. Hermann, and E. Frey. Pattern localization to a domain edge. *Phys. Rev. E*, 101(2):022414, 2020. doi: 10.1103/PhysRevE.101.022414.

[63] K.H. Fisher, D. Strutt, and A.G. Fletcher. Experimental and theoretical evidence for bidirectional signalling via core planar polarity protein complexes in Drosophila. *iScience*, 17:49–66, 2019. doi: 10.1016/j.isci.2019.06.021.

[64] J. Sharpe. Computer modeling in developmental biology: growing today, essential tomorrow. *Development*, 144(23):4214–4225, 2017. doi: 10.1242/dev.151274.

[65] J.F. Le Garrec, P. Lopez, and M. Kerszberg. Establishment and maintenance of planar epithelial cell polarity by asymmetric cadherin bridges: a computer model. *Dev. Dyn.*, 235(1):235–246, 2006. doi: 10.1002/dvdy.20617.

[66] D. Strutt and H. Strutt. Differential activities of the core planar polarity proteins during Drosophila wing patterning. *Dev. Biol.*, 302(1):181–194, 2007. doi: 10.1016/j.ydbio.2006.09.026.

[67] J. Wu and M. Mlodzik. The frizzled extracellular domain is a ligand for Van Gogh/Stbm during nonautonomous planar cell polarity signaling. *Dev. Cell*, 15 (3):462–469, 2008. doi: 10.1016/j.devcel.2008.08.004.

[68] G. Struhl, J. Casal, and P.A. Lawrence. Dissecting the molecular bridges that mediate the function of Frizzled in planar cell polarity. *Development*, 139(19):3665–3674, 2012. doi: 10.1242/dev.083550.

[69] S. Schamberg, P. Houston, N.A.M. Monk, and M.R. Owen. Modelling and analysis of planar cell polarity. *Bull. Math. Biol.*, 72(3):645–680, 2010. doi: 10.1007/s11538-009-9464-0.

[70] B. Anderson, J. Jackson, and M. Sitharam. Descartes' rule of signs revisited. *Am. Math. Mon.*, 105(5):447–451, 1998. doi: 10.2307/3109807.

[71] S. Fischer, P. Houston, N.A.M. Monk, and M.R. Owen. Is a persistent global bias necessary for the establishment of planar cell polarity? *PLOS ONE*, 8(4):e60064, 2013. doi: 10.1371/journal.pone.0060064.

[72] J. Estrada, F. Wong, A. DePace, and J. Gunawardena. Information integration and energy expenditure in gene regulation. *Cell*, 166(1):234–244, 2016. doi: 10.1016/j.cell.2016.06.012.

[73] R.C. Piper and J.P. Luzio. Ubiquitin-dependent sorting of integral membrane proteins for degradation in lysosomes. *Curr. Opin. Cell Biol.*, 19(4):459–465, 2007. doi: 10.1016/j.ceb.2007.07.002.

[74] J. Lavalou and T. Lecuit. In search of conserved principles of planar cell polarization. *Curr. Opin. Genet. Dev.*, 72:69–81, 2022. doi: 10.1016/j.gde.2021.11.001.

[75] J. Wu, A.C. Roman, J.M. Carvajal-Gonzalez, and M. Mlodzik. Wg and Wnt4 provide long-range directional input to planar cell polarity orientation in Drosophila. *Nat. Cell Biol.*, 15(9):1045–1055, 2013. doi: 10.1038/ncb2806.

[76] C. Harrison, H. Shao, H. Strutt, and D. Strutt. Molecular mechanisms mediating asymmetric subcellular localisation of the core planar polarity pathway proteins. *Biochem. Soc. Trans*, 48(4):1297–1308, 2020. doi: 10.1042/BST20190404.

[77] D.R.P. Tree, D. Ma, and J.D. Axelrod. A three-tiered mechanism for regulation of planar cell polarity. *Sem. Cell Dev. Biol.*, 13(3):217–224, 2002. doi: 10.1016/s1084-9521(02)00042-3.

[78] M. Matis, D.A. Russler-Germain, Q. Hu, C.J. Tomlin, and J.D. Axelrod. Microtubules provide directional information for core PCP function. *eLife*, 3:e02893, 2014. doi: 10.7554/eLife.02893.

[79] S. Schamberg. *Modelling planar cell polarity in Drosophila melanogaster*. PhD thesis, University of Nottingham, 2009.

[80] A.K. Classen, K.I. Anderson, E. Marois, and S. Eaton. Hexagonal packing of Drosophila wing epithelial cells by the planar cell polarity pathway. *Dev. Cell*, 9(6):805–817, 2005. doi: 10.1016/j.devcel.2005.10.016.

[81] A. Brittle, S.J. Warrington, H. Strutt, E. Manning, S.E. Tan, and D. Strutt. Distinct mechanisms of planar polarisation by the core and Fat-Dachsous planar polarity pathways in the Drosophila wing. *In revision*, 2022.

[82] P.N. Adler, J. Charlton, and J. Liu. Mutations in the cadherin superfamily member gene dachsous cause a tissue polarity phenotype by altering frizzled signaling. *Development*, 125(5):959–968, 1998. doi: 10.1242/dev.125.5.959.

[83] M. Matis and J.D. Axelrod. Regulation of PCP by the Fat signaling pathway. *Genes Dev.*, 27(20):2207–2220, 2013. doi: 10.1101/gad.228098.113.

[84] P.A. Lawrence and J. Casal. Planar cell polarity: two genetic systems use one mechanism to read gradients. *Development*, 145(23):dev168229, 2018. doi: 10.1242/dev.168229.

[85] C. Thomas and D. Strutt. The roles of the cadherins Fat and Dachsous in planar polarity specification in Drosophila. *Dev. Dyn.*, 241(1):27–39, 2012. doi: 10.1002/dvdy.22736.

[86] H. Strutt and D. Strutt. How do the Fat-Dachsous and core planar polarity pathways act together and independently to coordinate polarized cell behaviours? *Open Biol.*, 11(2):200356, 2021. doi: 10.1098/rsob.200356.

[87] M.K. Jolly, M.S. Rizvi, A. Kumar, and P. Sinha. Mathematical modeling of subcellular asymmetry of fat-dachsous heterodimer for generation of planar cell polarity. *PLoS One*, 9(5):e97641, 2014. doi: 10.1371/journal.pone.0097641.

[88] D. Singh, M.K. Jolly, and M.S. Rizvi. Emergence of planar cell polarity from the interplay of asymmetric interaction and tissue-level gradients. *bioRxiv*, 2021. doi: 10.1101/2021.11.30.468750.

[89] A.A. Ambegaonkar, G. Pan, M. Mani, Y. Feng, and K.D. Irvine. Propagation of Dachsous-Fat planar cell polarity. *Curr. Biol.*, 22(14):1302–1308, 2012. doi: 10.1016/j.cub.2012.05.049.

[90] J.C. Wortman, P.C. Nahmad, M.and Zhang, A.D. Lander, and C.C. Yu. Expanding signaling-molecule wavefront model of cell polarization in the Drosophila wing primordium. *PLoS Comput. Biol.*, 13(7):e1005610, 2017. doi: 10.1371/journal.pcbi.1005610.

[91] A. Brittle, C. Thomas, and D. Strutt. Planar polarity specification through asymmetric subcellular localization of Fat and Dachsous. *Curr. Biol.*, 22(10):907–914, 2012. doi: 10.1016/j.cub.2012.03.053.

[92] H. Matakatsu and S.S. Blair. Separating the adhesive and signaling functions of the fat and dachsous protocadherins. *Development*, 133(12):2315–2324, 2006. doi: 10.1242/dev.02401.

[93] R. Sopko, E. Silva, L. Clayton, L. Gardano, M. Barrios-Rodiles, J. Wrana, X. Varelas, N.I. Arbouzova, S. Shaw, S. Saburi, H. Matakatsu, S. Blair, and H. McNeill. Phosphorylation of the tumor suppressor fat is regulated by its ligand Dachsous and the kinase discs overgrown. *Curr. Biol.*, 19(13):1112–1117, 2009. doi: 10.1016/j.cub.2009.05.049.

[94] D. Ma, C. Yang, H. McNeill, M.A. Simon, and J.D. Axelrod. Fidelity in planar cell polarity signalling. *Nature*, 421(6922):543–547, 2003. doi: 10.1038/nature01366.

[95] J.D. Axelrod. Planar cell polarity signaling in the development of left-right asymmetry. *Curr. Opin. Cell Biol.*, 62:61–69, 2020. doi: 10.1016/j.ceb.2019.09.002.

[96] N. Verschueren and A. Champneys. A model for cell polarization without mass conservation. *SIAM J. Appl. Dyn. Syst.*, 16(4):1797–1830, 2017. doi: 10.1137/16M1093847.

[97] K.H. Fisher and D. Strutt. A theoretical framework for planar polarity establishment through interpretation of graded cues by molecular bridges. *Development*, 146(3): dev168955, 2019. doi: 10.1242/dev.168955.

[98] P.N. Adler, J. Taylor, and J. Charlton. The domineering non-autonomy of frizzled and van Gogh clones in the Drosophila wing is a consequence of a disruption in local signaling. *Mech. Dev.*, 96(2):197–207, 2000. doi: 10.1016/s0925-4773(00)00392-0.

[99] H. Zhu and M.R. Owen. Damped propagation of cell polarization explains distinct PCP phenotypes of epithelial patterning. *Sci. Rep.*, 3(1):1–10, 2013. doi: 10.1038/srep02528.

[100] H. Strutt and D. Strutt. Nonautonomous planar polarity patterning in Drosophila: dishevelled-independent functions of frizzled. *Dev. Cell*, 3(6):851–863, 2002. doi: 10.1016/s1534-5807(02)00363-5.

[101] Y.Y. Lin and D. Gubb. Molecular dissection of Drosophila Prickle isoforms distinguishes their essential and overlapping roles in planar cell polarity. *Dev. Biol.*, 325(2): 386–399, 2009. doi: 10.1016/j.ydbio.2008.10.042.

[102] D. Devenport. The cell biology of planar cell polarity. *J. Cell Biol.*, 207(2):171–179, 2014. doi: 10.1083/jcb.201408039.

[103] J. Hogan, M. Valentine, C. Cox, K. Doyle, and S. Collier. Two frizzled planar cell polarity signals in the Drosophila wing are differentially organized by the Fat/Dachsous pathway. *PLoS Genet.*, 7(2):e1001305, 2011. doi: 10.1371/journal.pgen.1001305.

[104] D. Ma, K. Amonlirdviman, R.L. Raffard, A. Abate, C.J. Tomlin, and J.D. Axelrod. Cell packing influences planar cell polarity signaling. *Proc. Natl Acad. Sci. USA*, 105 (48):18800–18805, 2008. doi: 10.1073/pnas.0808868105.

[105] A.G. Fletcher, M. Osterfield, R.E. Baker, and S.Y. Shvartsman. Vertex models of epithelial morphogenesis. *Biophys. J.*, 106(11):2291–2304, 2014. doi: 10.1016/j.bpj.2013.11.4498.

[106] M.S. Rizvi, D. Singh, and M.K. Jolly. Continuum theory for planar cell polarity. *bioRxiv*, 2021. doi: 10.1101/2021.11.30.468758.